Confined Fluid Phase Behavior and Its Influence on Unconventional Hydrocarbon Recovery

By

Gang Yang

Submitted to the graduate degree program in Chemical and Petroleum Engineering and the Graduate Faculty of the University of Kansas in partial fulfillment of the requirements for the degree of Doctor of Philosophy.

Chair: Dr. Xiaoli Li

Dr. Reza Barati

Dr. Russ Ostermann

Dr. Aaron Scurto

Dr. Xinmai Yang

Date Defended: 07 May 2021

The dissertation committee for Gang Yang certifies that this is the approved version of the following dissertation:

Confined Fluid Phase Behavior and Its Influence on Unconventional Hydrocarbon Recovery

Chair: Dr. Xiaoli Li

Date Approved: 07 May 2021

Abstract

Unconventional reservoirs are predominantly consisted of meso to nanoscale pores, which impose strong confinement effect to the encapsulated reservoir fluids and result in drastic deviations of confined fluid properties. Due to the lack of overall understanding of the nanoscale confinement, the phase behavior of confined fluids has not been well characterized. Furthermore, the influence of nanoscale confinement on the production and the ultimate recovery of unconventional reservoirs is not well predicted.

The focus of this dissertation is twofold: firstly, to propose solid theoretical models to characterize the confined fluid phase behavior within nanopores; secondly, to investigate the influence of nanoscale confinement on the primary and enhanced oil recovery (EOR) production of unconventional reservoirs. Regarding the first objective, a modified Peng-Robinson equation of state (PR EOS) is proposed with incorporation of both molecule-wall interaction and geometric constraints to determine the critical property shift and the deviated phase transition boundaries of confined fluids. The capillary condensation pressure of both single- and multicomponent fluids confined within nanopores are computed by a modified Kelvin equation. For the second objective, an improved algorithm with application of the modified PR EOS is established to compute the minimum miscibility pressure (MMP) of unconventional reservoir fluids with different injected gases. The deviated properties of confined fluids are incorporated into the compositional simulation model to predict their effect on the unconventional hydrocarbon recovery. Both the theoretical models and improved algorithm are validated with either experimental or molecular simulation results.

The modified PR EOS model is validated to be able to predict the confined fluid phase behavior at various pore sizes. Confinement effect imposes an overall shrinkage to both the *P-T* diagram and the two-phase region in a ternary diagram of CO_2/hydrocarbon systems, benefiting the miscible gas EOR in unconventional reservoirs by increasing the possibility of achieving the first contact miscibility. The modified Kelvin equation is applicable to compute the suppressed capillary condensation pressure of single- and multicomponent fluids with overall relative deviations of 7.65% and 6.52%, respectively. The molecule-wall interaction potential has the most significant contribution to the improved accuracy. Moreover, comparison to the experimental results demonstrate that the improved multiple mixing cell (MMC) algorithm is a reliable method to determine the MMP of unconventional reservoir fluids with different injected gases. Nanoscale confinement results in the drastic suppression of MMP and the suppression rate increases with decreasing pore size. For 100% CO_2 injection, the MMP suppression rate of Bakken oil and Eagle Ford oil at 10 nm are 6.22% and 13.01%, respectively. Compositional simulations demonstrate that the nanoscale confinement has obvious influence on the primary production and the ultimate recovery of gas huff-n-puff in unconventional reservoirs. The oil recovery factor of Eagle Ford well is increased by 12.20% at the end of the 13 years production with CH_4 huff-n-puff. The performance of gas huff-n-puff EOR in unconventional reservoir is highly dependent on the composition of reservoir fluids and properties of reservoir formations.

The results of this dissertation will deepen our understanding of the confined fluid phase behavior and provide reliable instructions for the unconventional hydrocarbon recovery. In addition, it will shed light on the characterization of confined fluid systems which would potentially be applied in some other nanoscale disciplines.

Acknowledgments

I would like to express my deepest gratitude to my advisor, Dr. Xiaoli Li for her inspiring mentorship, significant support, and great patience through my PhD study at The University of Kansas. Dr. Li, as a great role model, not only guided me how to be a qualified and independent researcher, but also inspired me to further my career goals in academia.

I would also like to sincerely thank my research committee, Dr. Reza Barati, Dr. Russ Ostermann, Dr. Aaron Scurto, and Dr. Xinmai Yang for their valuable suggestions and comments regarding both my research and this dissertation. Moreover, I want to say thank you to all the professors who I have been honored to work with as a Graduate Teaching Assistant, Dr. Paul Willhite, Dr. Shapour Vossoughi, and Dr. Karen Nordheden. I highly appreciate the knowledge and wisdom you taught me regarding how to be a good instructor and professor. In addition, I'm truly grateful for all my peer colleagues both inside and outside the School of Engineering for their kind support and companionship during my study at The University of Kansas. Special thanks to Martha Kehr, Dr. Di Chai, Dr. Ruyi Zheng, Dr. Xuejia Du, Mr. Yuhao Yang, and Ms. Julia Espinoza.

Lastly, I want to thank my family, particularly my parents, for their endless support, understanding, and love in both my good and bad times. Without your great efforts and sacrifices, none of my success would be possible.

Dedication

To my beloved parents,

Yang Shijie and Sun Xianping,

my dear brothers and friends,

who have taught me how to live and love the world.

Table of Contents

List of Figures

List of Tables

Chapter 1: Introduction

1.1 Background and Significance

Confined fluid phase behavior in nanopores has attracted great attention in recent years because of its application in unconventional hydrocarbon recovery, which sustains high potential in fulfilling the worldwide energy need. Shifted phase transitions of confined hydrocarbons play a significant role in reserve estimation, primary production, and the enhanced oil recovery (EOR) of unconventional reservoirs (Ambrose et al., 2012; Chen et al., 2013; Alharthy et al., 2013). Moreover, confined fluid phase behavior has also found its wide application in many other nanoscale disciplines including drug delivery, membrane separation, carbon storage, and micro-engineering (Laitinen et al., 2013; Uchytil et al., 2003; Bernardo et al., 2009; Fréchette et al., 2005). The extensive applications of confined fluid phase behavior have inspired much research interest in both academic and industrial institutions, which in turn yields more advanced techniques for applicable disciplines.

The fundamental questions of confined fluid phase behavior are how the dynamics of fluid molecules are altered in confined systems and how it impacts the macroscopic properties. As is well known, the molecules of ideal gas are regarded as moving point particles without any volume or intermolecular interactions. For real gas, the actual volume of gas molecules and intermolecular interactions are considered. As in confined space, since the molecule size is comparable to the pore size, the molecule-wall interaction becomes strong enough to compete against the intermolecular interaction (Gelb et al., 1999). Therefore, the dynamics of confined molecules is controlled by a counterbalance between geometric constraints and molecule-wall interaction (Kremer et al., 2003; Richert, 2011). Their relative influence is determined by the size of the pores and the strength of the interaction between guest molecules and the pore surface. Bras et al. (2014) concluded that the

overall behavior inside the nanopores is consisted of two distinct dynamical domains, originated by molecules in the core of the pore cavity and adjacent to the pore wall. Derycke et al. (1991) illustrated a reduction of the effective Van der Waals molecular volume of the adsorbate in pores of atomic size and Gavette et al. (2014) observed the folding phenomenon of long-chain alkanes in nanosized capsules, reflecting the contortions imposed by confinement. Consequently, the variations of molecular dynamics result in the shift of thermodynamic properties and phase behavior of confined fluids.

Due to the strong confinement effect, confined fluid phase behavior deviates significantly from that of bulk fluids, including the critical properties shift, the phase diagram shift, and the surface driven phase transitions not existing in bulk space, such as capillary condensation. With respect to that fact, numerous theoretical and experimental works have been conducted to characterize those deviations. Theoretical works, including the modified/extended equations of state (EOS), molecular simulations, and density functional theory (DFT) are dominant because of their high flexibility and low cost in both time and expenses. Experimental approaches, however, are less prevalent because of the significant challenges and high cost of simulating real confined systems. Some highly promising experimental methods include nanoscale isotherm adsorption, differential scanning calorimetry (DSC), nanofluidic chip, and other microscopy methods. Despite the numerous works, the physics behind confined phase behavior is still in its early exploratory stage. It is far from well-understanding not only because of the complex interplay of the surface-interfaces but also the difficulties in experimentally quantifying the phase boundaries in confined space. In addition, publications of partly contradicting results have also stirred up controversial discussions due to the lack of solid experimental validations. Essentially, confined fluid phase behavior is still an intriguing yet unanswered question.

1.2 Research Objective and Tasks

The overall objective of this dissertation is to develop reliable theoretical methods to characterize the confined fluid phase behavior within nanopores and to further investigate its impact on the unconventional hydrocarbon recovery. The following specific tasks have been addressed regarding this objective:

(1) A modified PR EOS model is proposed by incorporating both the molecule-wall interaction and geometric constraints. It is validated to be relatively accurate to determine both the critical property shift and the phase transition boundaries of confined fluid systems, including unconventional hydrocarbons.

(2) A modified Kelvin equation is developed to compute the capillary condensation pressure of both single- and multicomponent fluids within nanopores down to 2 nm with the overall relative deviations of 7.65% and 6.52%, respectively.

(3) An improved algorithm with application of the modified PR EOS is proposed to determine the minimum miscibility pressure (MMP) of different unconventional reservoir fluids with various injected gases at multiple nanopore sizes.

(4) Compositional simulation models with well-incorporated nanoscale confinement are established to investigate the influence of shifted confined fluid properties on both the primary and the gas huff-n-puff production in unconventional reservoirs.

1.3 Organization of the Dissertation

The organization of this dissertation is demonstrated in Figure 1.1. Chapter 1 illustrates the significance and research objective of this dissertation. Chapter 2 highlights the state-of-the-art research regarding both the experimental and theoretical approaches to investigate the confined

fluid phase behavior and its impact on the unconventional hydrocarbon recovery. Chapters 3 and 4 demonstrate the establishment of the theoretical models to characterize the confined fluid phase behavior within nanopores. Specifically, Chapter 3 is the modified PR EOS model with consideration of both molecule-wall interaction and geometric constraints. Chapter 4 is the modified Kelvin equation to calculate the capillary condensation pressure of both single- and multicomponent fluids. Chapters 5 and 6 elaborate the effect of nanoscale confinement on the unconventional hydrocarbon recovery, where Chapter 5 proposes a reliable algorithm to compute the MMP of unconventional reservoir fluids with different injected gases. Chapter 6 manifest the compositional simulation of unconventional reservoirs with well-incorporated nanoscale confinement. Chapter 7 lists the summary and conclusions.

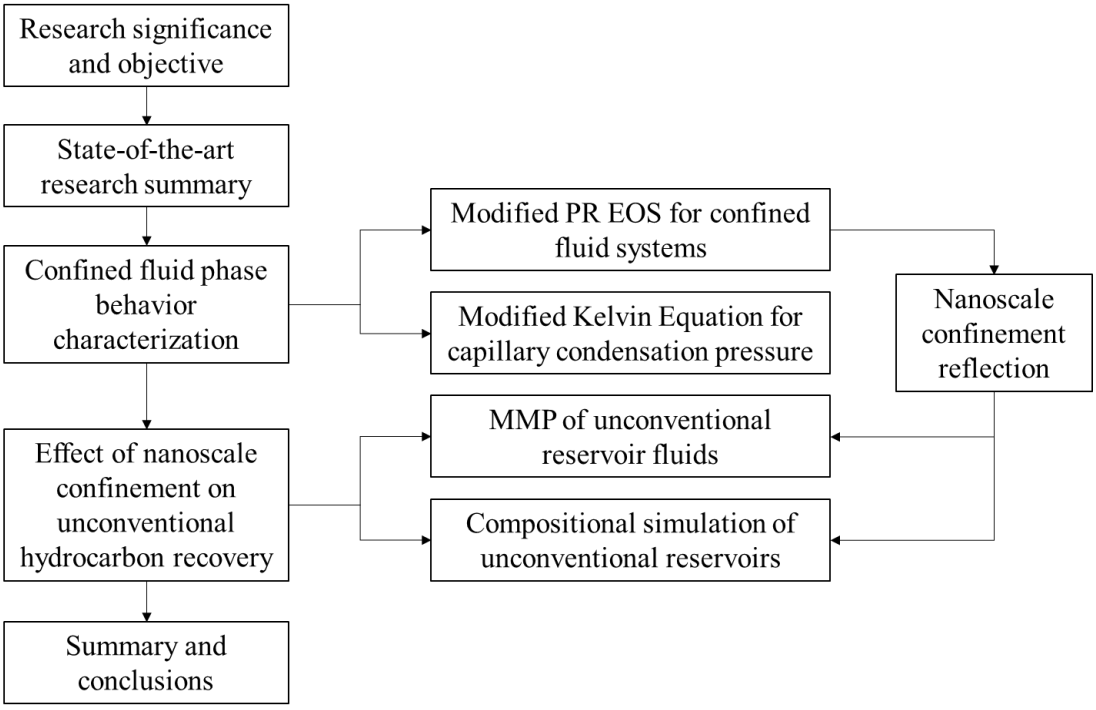

Figure 1.1: Organization of the dissertation

Chapter 2: Literature Review

This chapter highlights the state-of-the-art research of confined fluid properties and phase behavior deviations, experimental and theoretical approaches to investigate the confined fluid phase behavior, and the impact of nanoscale confinement on both the primary production and the enhanced oil recovery (EOR) in unconventional reservoirs.

2.1 Confined Fluid Phase Behavior Deviation

Confined fluid phase behavior deviates significantly from that of bulk fluids because of the nanoscale confinement resulting from strong molecule-wall interaction and geometric constraints (Yang and Li, 2020). These deviations are widely manifested in thermodynamic properties (density and viscosity), phase transition boundaries (bubble point, dew point, critical point), and unique phase transitions induced by surface-driven forces (capillary condensation).

2.1.1 Density and viscosity

The existence of confining boundaries not only disturbs the spatial distribution of the constituent molecules but also affects the dynamic rearrangement of those molecules, resulting in an oscillatory density distribution in confined space (Giovambattista et al., 2006; Israelachvili, 2011; Ingebrigtsen and Dyre, 2014), as illustrated in Figure 2.1 (a). Despite the oscillation, the overall density of confined fluids is greater than that of the bulk fluids. Figure 2.1 (b) demonstrated the CH_4 density as a function of graphite nanopore size and the total CH_4 density can be drastically higher than the bulk density within pores smaller than 20 nm (Cao et al., 2016). Moreover, Eberle et al., (2016) measured the methane density in shale samples and concluded that the density in organic mesopores is two times greater than the bulk value. It is also proved that the excess density

persists to elevated temperatures, which provides new insight into the hydrocarbon storage mechanisms within unconventional reservoirs.

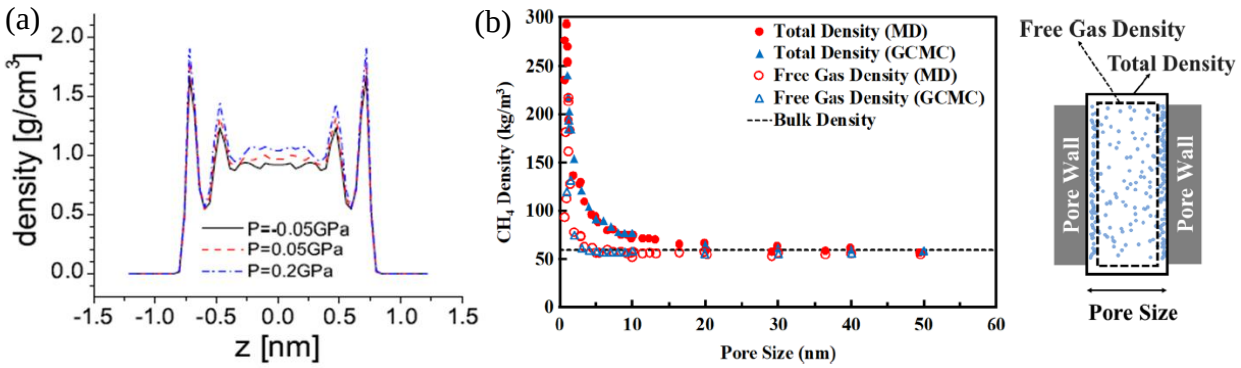

Figure 2.1: Nanoconfined fluid density. (a) Water in nanoscale plate under different pressure (Giovambattista et al. 2006); (b) CH_4 within graphite of different sizes (Cao et al. 2016).

The strongly inhomogeneous distribution of molecules also induces variations in the transport properties of confined fluids (Chai et al., 2019). The shear viscosity of liquid usually increases and becomes non-Newtonian when confined to a thin film (Israelachvili 2011). Figure 2.2 (a) shows the local shear viscosity of Lennard-Jones fluids confined in narrow slit pores. As can be seen, the local shear viscosity, depending on the density inhomogeneities, varies strongly with the distance to the walls (Hoang and Galliero, 2012). Experiments and theory also prove that the viscosity of water confined between hydrophilic surfaces increases with confinement, reaching values orders of magnitude higher within a subnanometer gap (Goertz et al., 2007). Young et al. (2013) demonstrated the increased viscous shear forces (apparent viscosity) of nanoconfined water between solid hydrophilic surfaces of different wettability. A drastic decrease is reflected in Figure 2.2 (b) when the surface becomes increasingly hydrophobic. Their results offered a new understanding of interfacial fluids, which can be used to control nanoscale flow.

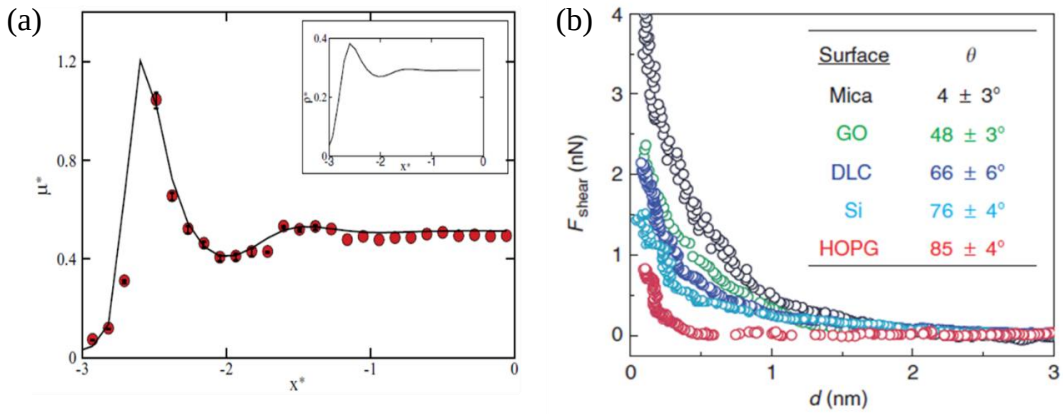

Figure 2.2: Viscosity of confined fluids. (a) Viscosity profile of simple Lennard-Jones fluid confined in narrow slit pores (Hoang and Galliero, 2012); (b) Shear viscous force of water confined within 0.1 to 3 nm (Young et al., 2013).

2.1.2 Phase transition boundaries

The geometric constraints and molecule-wall interaction in confined systems impose drastic shift to the phase transition boundaries of confined fluids, which has been extensively studied for decades (Fisher and Nakanishi, 1981; Morishige et al., 1997; Gelb et al., 1999; Yang and Li, 2020). It is generally concluded that the freezing temperature, the melting temperature, the saturation pressure, and the critical point of pure fluids are all suppressed in confined space. Findenegg et al. (2008) studied the freezing/melting of nanoconfined water and plotted the pore size dependence of the melting temperature, as shown in Figure 2.3 (a). A linear correlation between the melting point suppression and the reciprocal diameter was found by Jackson and Mckenna (1990) for the nonpolar organics confined in controlled pore glasses. Qiu et al. (2019) demonstrated in Figure 2.3 (b) the suppressed saturation pressure curve of CO_2 confined in SBA-15. Figure 2.3 (c) and (d) illustrated the suppressed critical temperature of different confined fluids (Yang et al., 2019) and shifted two-phase diagrams of binary mixtures (Sandoval et al., 2015).

Despite the widely accepted insights, conflicting results also exist for confined fluid mixtures due to the complexity of the systems. Liu et al (2016) observed higher bubble-point pressure for partially confined binary mixture N_2/*n*-C_4H_{10}, which is against the results of numerous experimental and theoretical works. Meanwhile, Salahshoor and Fahes (2020) measured the dew-point pressure of gas condensate in a nano-porous medium by isochoric method and concluded that the confinement effect shifts the dew-point pressure towards higher values, which is contrary to many published models. Table 2.1 listed some typical works demonstrating the shift of phase transition boundaries of confined fluids.

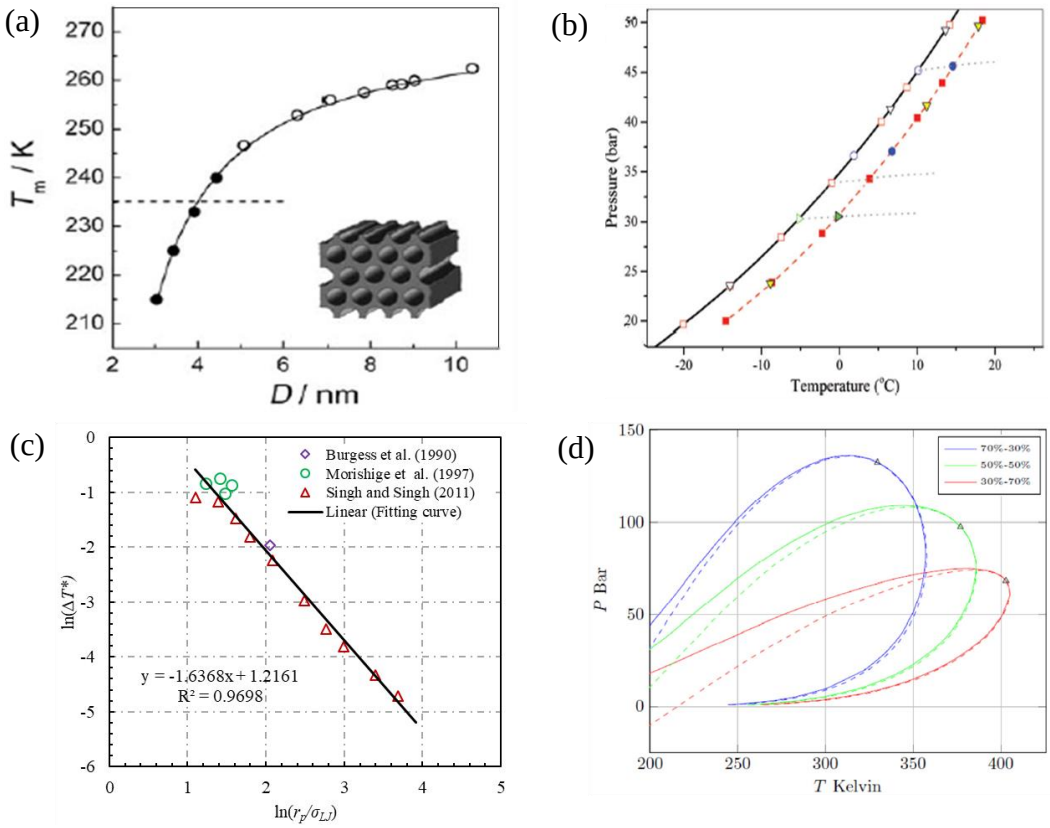

Figure 2.3: Phase transition shift of confined fluids. (a) Melting temperature of nanoconfined water (Findenegg et al., 2008); (b) Saturation pressure shift of confined CO_2 (Qiu et al., 2019); (c) Critical temperature shift of different fluids (Yang et al., 2019); (d) Phase diagram of C_1+C_4 with consideration of capillary pressure within 10 nm (Sandoval et al., 2015).

Table 2.1: Phase transition shift of confined fluids

References	Fluid	Material	Pore size, nm	Properties	Shift
Findenegg et al. (1994)	Cyclopentane, iso-pentane etc.	CPG	7.0/7.7/24.2	Capillary condensation pressure	Suppression
Morishige et al. (1997)	Ar, N_2, O_2, C_2H_4, CO_2	MCM-41	1.2/1.4/1.8/2.1	Critical temperature	Suppression
Maniwa et al. (2002)	Water	Carbon Nanotube	1.35-1.38	Freezing temperature	Suppression
Takaiwa et al. (2008)	Water	Carbon nanotube	0.9-1.7	Melting point temperature	Suppression
Parsa et al. (2015)	Propane	Nanofluidic chip	50/30	Bubble-point pressure	Suppression
Alfi et al. (2016)	Hexane, heptane, and octane	Nanofluidic chip	50	Bubble-point temperature	Almost equal to bulk values
Luo et al. (2016)	Octane and decane	GPG	4.3/38.1	Bubble-point temperature	Elevation by 15 K
Cho et al. (2017)	Decane/methane Octane/methane	SBA-15 SBA-16	4	Bubble-point pressure	Suppression
Jatukaran et al. (2018)	Propane	Nanoporous media	9	Evaporation pressure	Suppression
Barsotti et al. (2018)	n-Pentane, isopentane, and CO_2	MCM-41	2.78/3.70/ 6.32	Capillary condensation pressure	Suppression
Barsotti et al. (2018)	Propane, n-butane, and n-Pentane	MCM-41	2.90/4.19/8.08	Critical temperature	Suppression
Tan et al. (2019)	CO_2, C_2H_6	SBA-15	4.570/6.079/8.145	Critical temperature/pressure	Suppression
Salahshoor and Fahes (2020)	Ethane/pentane	$BaTiO_3$ nanoparticles	1-70	Dew point pressure	Elevation

2.1.3 Unique phase transitions

Confinement induces unusual behavior in matter (Mashl et al., 2003). The effect of wall forces and the competition between molecule–wall and intermolecular interactions in confined systems lead to surface-driven phase changes, such as capillary condensation (Gelb et al. 1999). This unique phenomenon represents a confinement induced gas-liquid phase transition occurring in nanoscale adsorption at a pressure lower than the bulk saturation pressure. Barsotti et al. (2016) provided a general review of the theoretical and experimental works on capillary condensation

with emphasis on the production and interpretation of adsorption isotherms in hydrocarbon systems. Yang et al. (2019) collected the capillary condensation pressure of various confined fluids within different nanopore sizes, as demonstrated in Figure 2.4 (a). It has also been proved that even simple fluids confined within nanoscale pores can exhibit unusually rich behavior (Ingebrigtsen and Dyre, 2014). Maniwa et al. (2002) found that the liquid-like water transformed into a new solid form at 235 K while studying water adsorption in carbon nanotube bundles. Han et al. (2010) presented the simulation results for water in a quasi-two-dimensional hydrophobic nanopore slit and claimed that water might freeze by means of both first order and continuous phase transitions. The phase diagram of nanoconfined water was schematically demonstrated in Figure 2.4 (b) by hypothesizing the existence of a connection point at which first-order and continuous transition lines meet. The existence of a variety of new ice phases not seen in bulk were reported by Koga et al. (2001) during simulations of water encapsulated in carbon nanotubes (Figure 2.5).

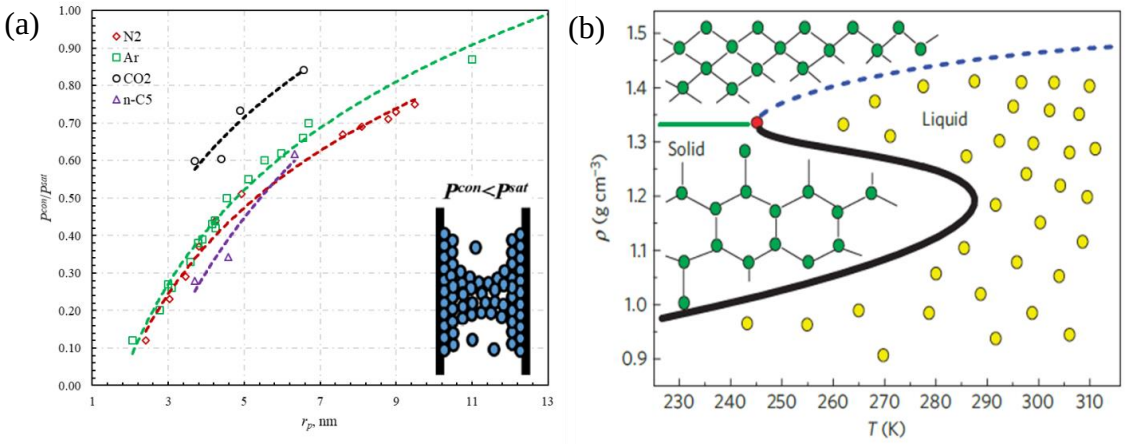

Figure 2.4: Unique phase transitions in confined space (a) Capillary condensation pressure ratio of various fluids at different pore sizes (Yang et al, 2019); (b) Schematic phase diagram of nanoconfined water in the density–temperature plane (Han et al., 2010).

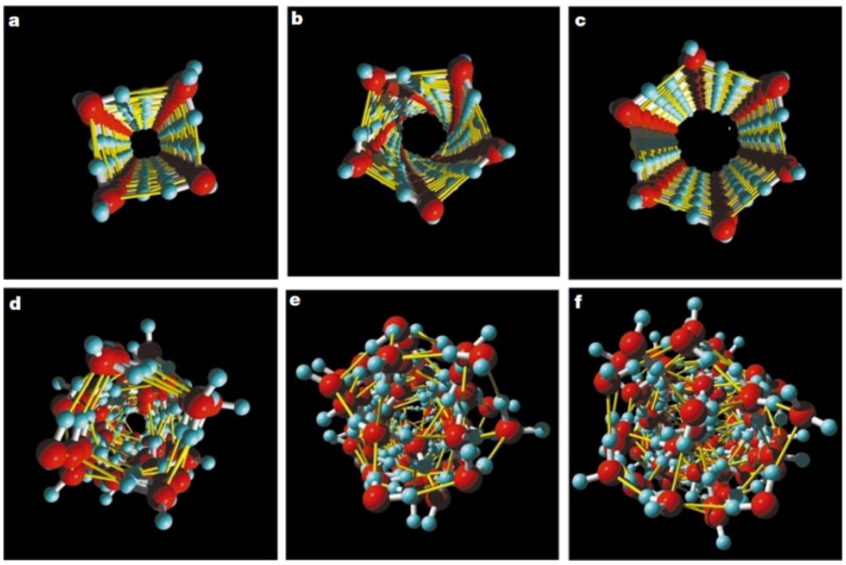

Figure 2.5: Snapshots of quenched molecular coordinates (Koga et al. 2001). (a) Square; (b) pentagonal; (c) hexagonal ice-nanotubes in 11.1 nm, 11.9 nm, and 12.6 nm inner diameter SWCNTs, respectively. Figures (d), (e) and (f) are the corresponding liquid phases.

2.1.4 Heat of evaporation/condensation

Heat of evaporation is the amount of energy requires to be added to transform a quantity of substance from liquid to vapor phase. While the heat of condensation is the energy to be released by the substance during vapor to liquid phase transition. Since evaporation and condensation of a given substance are the exact opposite processes at bulk conditions, the heat of evaporation is numerically equal to the heat of condensation. Within confined space, however, these two values are not equal because of the existence of hysteresis. Tan et al. (2017) pointed out that the Clapeyron equation was valid to calculate the heat of evaporation and condensation of confined fluids within nanopores. This statement can be verified by the highly linear correlations between $\ln(P)$ and $1/T$ in Figure 2.6 (a). While Figure 2.6 (b) illustrated the heat of evaporation and condensation of N_2 at bulk and confined space. As can be seen, both heat of evaporation and condensation are

increased in nanopores. The smaller the pore size, the larger the heat of evaporation and condensation values. The gap between the heat of evaporation and condensation represents the effect of hysteresis in confined space.

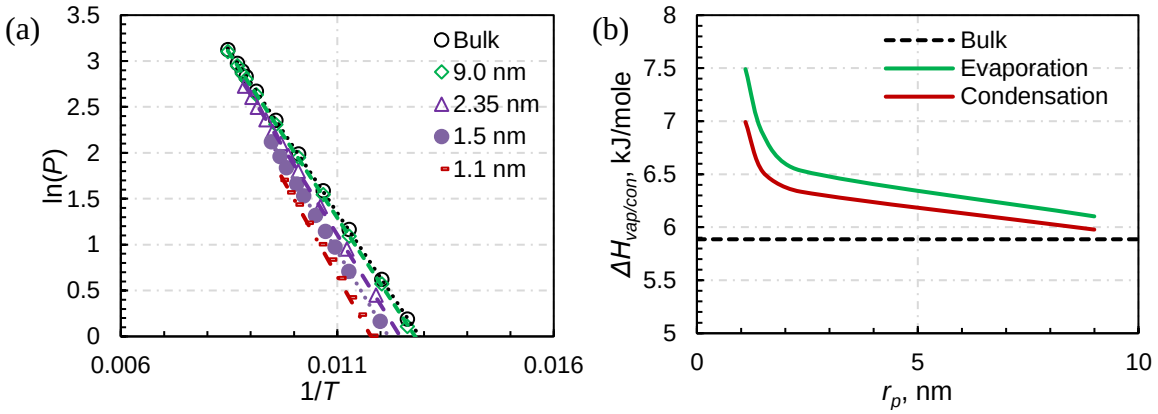

Figure 2.6: Heat of evaporation and condensation in bulk and confined space (a) Validation of Clapeyron equation at different pore sizes (data from Morishige and Nakamura, 2004); (b) Heat of evaporation and condensation of N_2.

2.2 Experimental Works on Confined Phase Behavior

The experimental approaches applicable to investigate confined fluid phase behavior, although not as widely seen as theoretical works, tend to expand at an accelerated pace, resulting from the popularity of confined systems and the validity of the theoretical and simulation works. Some highly promising experimental approaches include nanoscale isotherm adsorption, differential scanning calorimetry (DSC), nanofluidic chip, and other microscopy methods. All these visual or non-visual approaches can generate direct/indirect observation data on confined phase behavior characterization and interpretation.

2.2.1 Nanoscale isotherm adsorption

Nanoscale isotherm adsorption was initially used to investigate the monolayer phase behavior of simple gases (argon, krypton, xenon, and methane) adsorbed on graphite surface. It was demonstrated that monolayer films may exhibit various phases, resembling the ordinary bulk gases, liquids and solids (Thomy and Duval, 1970). Triggered by this pioneering work, extensive experimental studies have been carried out for adsorption of simple molecules on graphite (Thomy et al., 1981), boron nitride (Regnier et al., 1979), alkali halides (Schmicker et al., 1991), and metals (Glachant et al., 1982). These studies enabled to construct phase diagrams for a variety of systems and provided further information concerning the inner structure of different phases. In principle, nanoscale adsorption allows the complete thermodynamic characterization of a physisorbed system (Marx, 1985). However, two fundamental phenomena commonly investigated in recent years are the capillary condensation and critical point, as schematically demonstrated in Figure 2.7.

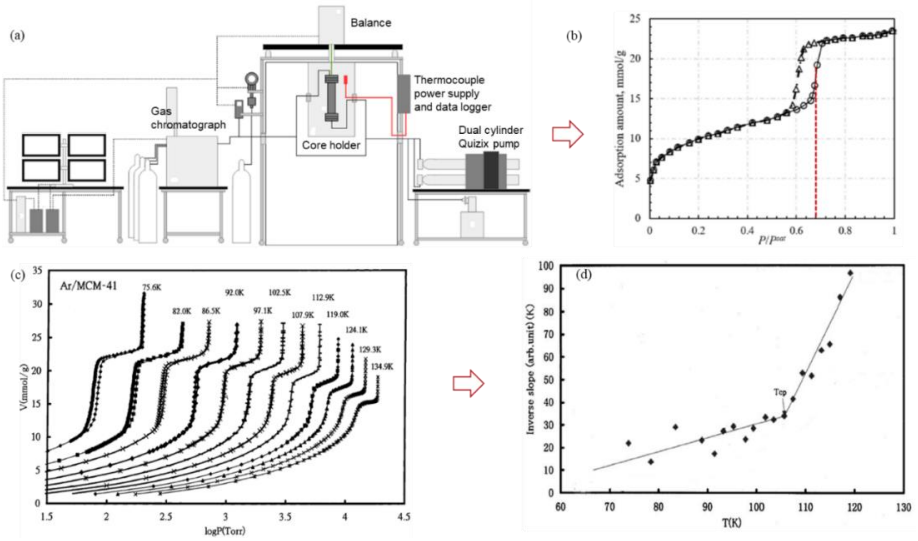

Figure 2.7: Determination of capillary condensation pressure and critical point via nanoscale adsorption isotherms. (a) Schematic diagram of experimental setup (Barsotti et al., 2018); (b) Determination of capillary condensation pressure (Ravikovitch and Neimark, 2001); (c) Adsorption isotherms at different temperatures (Morishige and Nakamura, 2004); (d) Determination of confined critical temperature T_{cp} (Morishige and Ito, 2002).

Capillary condensation

Adsorption isotherm relates the amount of adsorbed fluid on mesoscale pores (MCM-41, SBA-15, and controlled pore glass) to the operating bulk pressure at a given temperature. The "vertical steps" in the adsorption isotherms is widely accepted to indicate the first-order phase transition, namely capillary condensation, occurring in the film before reaching the bulk saturation pressure (Regnier et al. 1979; Horikawa et al., 2011). In real experiments, however, this verticality is usually lost to some extent because of the size distribution and nonuniformity of the adsorption surface (Barsotti et al, 2016). Hence, the capillary condensation pressure is generally identified as the midpoint of the step change in the adsorption isotherm branch, as demonstrated in Figure 2.7 (b). Barsotti et al. (2018) applied a novel gravimetric apparatus to generate the adsorption isotherms of both binary mixture of carbon dioxide and n-pentane and ternary mixture of carbon dioxide, n-pentane, and isopentane to determine their capillary condensation pressure within MCM-41. Later, they also investigated the capillary condensation hysteresis of n-butane and n-pentane in kerogen-rich shale core and concluded that new core analysis and reservoir modeling procedures must be developed to account for the irreproducible hysteresis at reservoir temperature.

Critical point

The first noteworthy attempt to determine the critical temperature by adsorption isotherms was carried out for methane adsorbed on the cleavage face of $FeCl_2$. It was proposed that the plot of the inverse slope of the adsorption isotherm steps, $T\ln(P/P_0)$, against temperature follows two linear trends and the inflection point locates the critical temperature (Nardon and Laher, 1974). Following this method, Millot et al. (1982) obtained the critical temperature of Ar, Kr, and Xe on a number of lamellar dihalides and Morishige et al. (1997) recognized the critical temperature of Ar, N_2, O_2, C_2H_4, and CO_2 adsorbed in mesoporous MCM-41 at different pore sizes. Figure 2.7 (d)

demonstrated the determination of the confined critical temperature of N_2 within SBA-15 nanopores (Morishige and Ito, 2002). All the above studies and the results of some other experimental works (Quateman and Bretz, 1984) proved the validity of the proposed method by Nardon and Laher (1974) to determine the critical point of confined fluids. Barsotti et al. (2018) measured the critical temperature of propane and n-butane confined in MCM-41 via this method.

Nanoscale isotherm adsorption is valid to obtain the capillary condensation pressure and confined critical point. However, its applicability for investigating capillary evaporation process within nanopores is still under discussion because of the ambiguous underlying physics. One widely accepted theory is that capillary condensation represents thermodynamic equilibrium transitions within nanopores, while capillary evaporation proceeds through metastable states (Morishige and Nakamura, 2004; Grosman and Ortega 2005). Experimental verification of such a statement is, however, extremely difficult even with leading edge technique (Morishige, 2016). Limited by the experimental apparatus, nanoscale isotherm adsorption is more applicable for pure gases. The validity for gas mixtures need to be further examined with consideration of the competitive adsorption, which contributes significantly to the capillary condensation of mixtures (Yang et al., 2019). Moreover, the effect of morphology and topology of the nanopores on capillary condensation and evaporation has not been experimentally investigated even though numerous theoretical works have demonstrated so.

2.2.2 Differential scanning calorimetry (DSC)

Differential scanning calorimetry (DSC) has long been used to investigate the phase transitions such as melting, crystallization, glass transition, and vaporization at bulk conditions. The underlying principle is that when a material undergoes a physical transformation, the

associated exothermic or endothermic heat is monitored, as demonstrated in Figure 2.8 (a). To investigate the fluid phase behavior deviation in nanopores, well-characterized nanomaterials are usually applied to impose the confinement effect (Luo et al. 2018), as in Figure 2.8 (b).

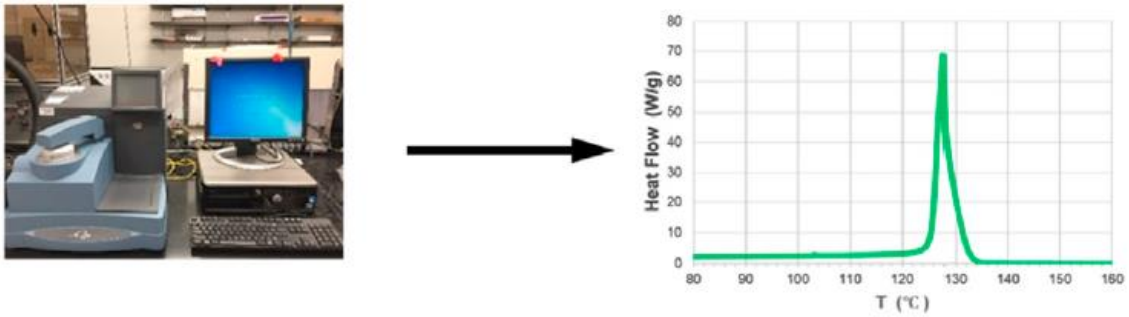

(a) Schematic diagram of DSC measurement

(b) Introduction of the confinement effect

Figure 2.8: DSC Experimental setup for confined phase behavior in nanopores (Luo et al., 2018).

Jackson and Mckenna (1990, 1991, and 1996) conducted their pioneering work to investigate the effect of confinement on the solid-liquid phase transition and the glass transition behavior of organic fluids by DSC. They claimed that both the melting point and the glass transition temperature are suppressed in confined space and the suppression rate increased as the pore size decreases. After their work, numerous studies have been performed with the glass transition behavior and the liquid dynamics of different materials in various confining geometries (Alcoutlabi and McKenna, 2005). In recent years, DSC has been widely applied to investigate the phase transitions of confined hydrocarbons. Luo et al. (2016) measured the bubble-point

temperature of *n*-octane and *n*-decane confined in controlled pore glasses at 4.3 and 38.1 nm and concluded that the confinement effect is insignificant at 38.1 nm but imposed a 15 K increase to the bubble-point temperature at 4.3 nm. They also measured the bubble-point temperature of *n*-hexane, *n*-octane, and *n*-decane under multiple confinement scales of silicate materials with pore diameter ranging from 2-40 nm and claimed that the confined fluid generally vaporized at a temperature higher than the bulk fluid. Qiu et al. (2018) proposed a novel isochoric DSC procedure to measure the vapor–liquid phase transition and this method is later applied to obtain the suppressed vapor pressure of pure fluids and dew point of mixtures in nanopores (Qiu et al., 2019).

Unlike nanoscale isotherm adsorption, well-designed DSC experiments can potentially generate the complete phase diagram of confined fluids, including bubble point, dew point, and critical point. Experimental results of both pure fluids and binary mixtures have been reported in current works. However, it has been demonstrated that the loading of fluids and the heterogeneous distribution of fluids within nanopores both have obvious effect on the experimental results (Luo et al., 2016). Hence, extra attention should be paid for the measurement and interpretation of multicomponent fluids to avoid questionable or false conclusions. Qiu et al (2021) studied the phase behavior of binary mixtures confined in SBA-15 using DSC and claimed that the confined mixtures do not exhibit phase coexistence region as the bulk mixtures do. This conclusion is highly questionable considering the formation of capillary condensation of confined mixtures within nanopores, where condensed phase and vapor phase coexist in nanopores.

2.2.3 Nanofluidic chip

Nonofluidic chip is another promising approach applicable for investigating the confined phase behavior. Nanofluidic visualization experiments, as schematically demonstrated in Figure

2.9, have enabled direct observation of phase and flow behavior in nanopores, including vaporization, capillary filling, imbibition, pressure-driven flow, and multiphase displacement measurements (Bao et al., 2017). Mostowfi et al. (2012) designed a novel microfluidic device to analyze phase diagrams of gas-liquid systems, mimicking the phase transitions of a reservoir fluid travelling through the wellbore from the formation. Alfi et al. (2016) applied nanofluidic device to visualize the evaporation of hexane, heptane, and octane in nano-channels 5 um wide by 50 nm deep, they claimed that the bubble-point temperature measured on the nanofluidic chip was almost equal to the bulk bubble-point temperature, representing that the confinement effect at 50 nm is negligible. Yang et al. (2019) conducted the lab-on-chip approach to measure n-butane condensation in slit pores of 50, 10, and 4 nm and concluded that the dew-point pressure can deviate as high as 14% from the bulk values. Furthermore, silicon glass nanofluidic devices compatible with high temperature (up to 573 K) and pressure (up to 20 MPa) were proposed by Zhong (2019), to directly quantify fluid behaviors in nanoconfinement down to sub-10 nm. The full characterization of hydrocarbon phase transition and transport properties for both single component and mixtures are performed.

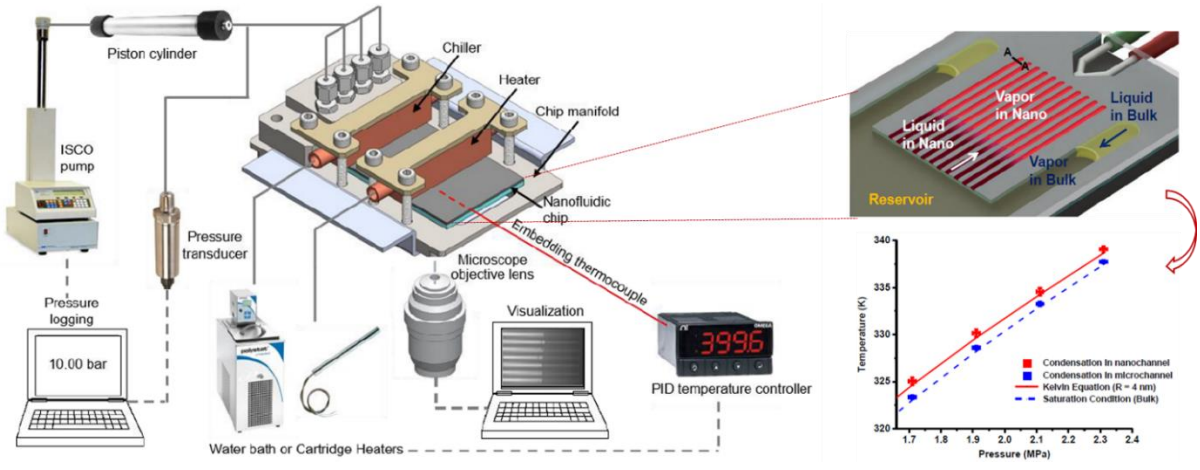

Figure 2.9: Schematic of the experimental setup connecting nanofluidic chip

Nanofluidic chip can be applied to measure the bubble point and dew point of both pure and multicomponent fluids within nanopores. However, no results of critical point, which may require further experimental setup, have been reported (Nikitin and Popov 2015). Moreover, unlike the nanoscale isotherm adsorption or DSC where well-defined nanomaterials can be applied, nanofluidic chip method is highly dependent on the fabrication of the chips where nanoscale pores are created by chemical etching techniques (Zhong 2019). Specifically, how to establish and maintain the desired nanopores at a specific size, especially for extremely small size (sub-10 nm) at extreme temperature/pressure conditions (unconventional reservoir), remains a significant challenge. In addition, it seems even more challenging to incorporate shale with highly complicated and interconnected nanopore systems into this approach, which limits its practical application for unconventional reservoirs.

2.2.4 Microscopy method

Microscopy method has the capability to capture fluid dynamics at nanoscale, as shown in Figure 2.10. Transmission electron microscopy (TEM) demonstrated that closed carbon nanotubes can retain fluids trapped during synthesis (Gogotsi et al., 2001). X-ray diffraction studies illustrated water freezing into crystalline solids i.e., ice nanotubes within open-ended single-walled carbon nanotubes (SWNTs) (Maniwa et al. 2002). Environmental scanning electronic microscopy (ESEM) was used to reflect the in-situ dynamics of condensation, evaporation, and transport of water inside carbon nanotubes (Rossi et al., 2004). Yaziciogglu et al. (2005) visualized the aqueous multiphase fluids trapped in closed multiwall carbon nanotubes with high resolutions using TEM. Sirghi et al. (2006) performed AFM pull off experiments with hydrophilic tips and claimed that the stretched nanoscopic water bridges are in mechanical equilibrium with the external pull-off

force but not in thermodynamic equilibrium with the water vapor in air. These highly sophisticated experimental approaches manifest significant potential to reveal the underlying physics of confined phase behavior.

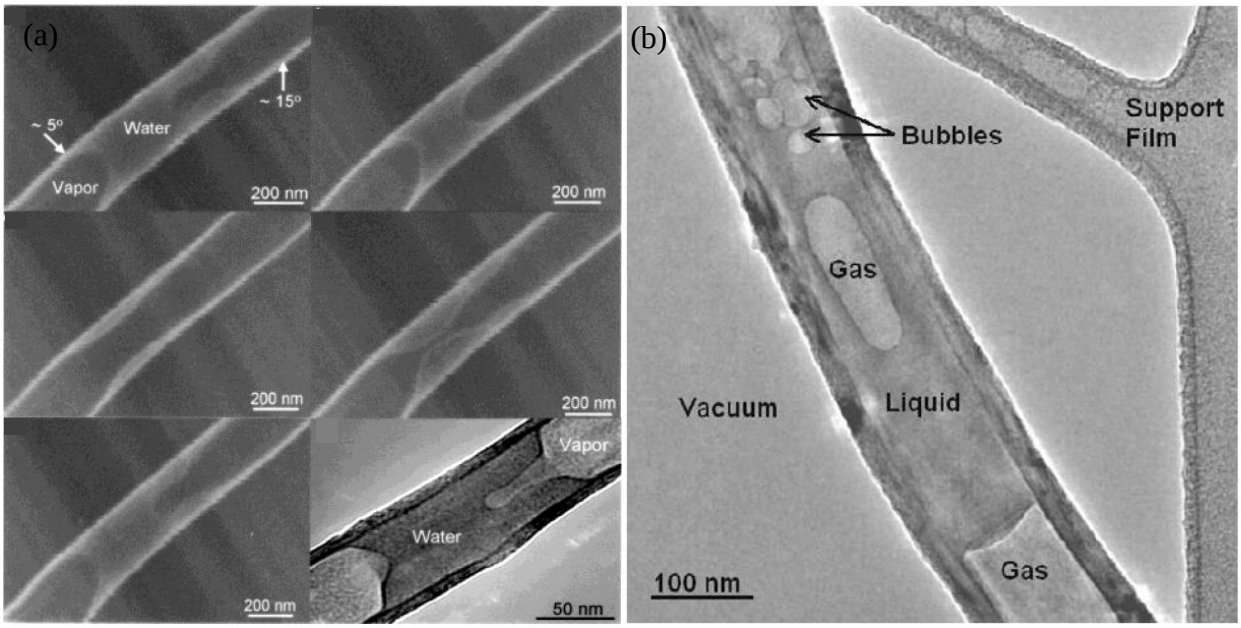

Figure 2.10: Dynamic behavior of confined fluids within nanopores (a) ESEM images and TEM image of water under different pressure in CNT (Rossi et al., 2004); (b) TEM image from a dynamic heating experiment on a fluid-filled CNT (Yazicioglu et al., 2005).

Like nanoscale isotherm adsorption and DSC, the confined space of microscopy method is usually established by well-defined nanomaterials. Image analyses by electron microscopy have also been widely performed to understand the pore-size distribution, organic geochemistry, mineralogy of shale rocks (Zhang et al. 2019). In addition, it is applicable for the dynamics capture of both pure and multicomponent fluids confined in nanopores. Despite its drastic potential in revealing the underlying physics behind confined fluid systems, microscopy methods have rarely been reported to quantify the deviations of confined fluid properties. Moreover, this method is usually limited by its testing conditions of sub-ambient atmosphere pressure and sub-room

temperature (Zhong 2019). The high cost of the sophisticated apparatus also limits its industrial accessibility. Furthermore, no results have been reported of microscopy method being applied to investigate confined fluids within any complicated or interconnected nanopores, such as shale core with pore size distribution.

Table 2.2 summarizes the comparison of different experimental approaches. Firstly, both nanoscale isotherm adsorption and DSC are non-visual methods, in which the experimental results require further interpretation before obtaining the confined fluid properties. On the contrary, nanofluidic chip and microscopy method belong to the visual category through which the phase transitions of confined fluids can be directly observed. Secondly, for nanofluidic chip method, the confined space is fabricated by etching into designed chips, which sets high standard for the fabrication process of chips with desired pore size range. While for the other three approaches, the confined space is obtained from well-defined nanomaterials. Thirdly, DSC is the only method capable of generating the complete phase diagram of confined fluids, while the other three can only be applied to investigate specific properties. Fourthly, most of the methods are valid for both pure and multicomponent fluids in either gas or liquid phase, except for the fact that liquid phase adsorption in nanopores cannot be applied for the capillary condensation investigation. For future work, further efforts need to be spared to investigate the phase behavior of complex mixtures within advanced confined systems of wider pore size distribution, specifically shale hydrocarbons within shale samples. More experimental works can be conducted to investigate the effect of pore geometry and pore chemistry on confined fluid phase behavior. The variation of the pore chemistry and pore structure with temperature, pressure, or entrapment of the guest molecules can also be explored.

Table 2.2: Comparison of different experimental approaches

Experiments	Visual	Nanopores	Bubble point	Dew point	Critical point	Gas	Liquid	Pure fluids	Fluid mixtures
Nanoscale isotherm adsorption	No	Nanomaterials	No	Yes	Yes	Yes	No	Yes	Yes
Differential scanning calorimetry	No	Nanomaterials	Yes	Yes	Yes	Yes	Yes	Yes	Yes
Nanofludic chip	Yes	Fabricated chips	Yes	Yes	No	Yes	Yes	Yes	Yes
Microscopy method	Yes	Nanomaterials	Yes	Yes	No	Yes	Yes	Yes	Yes

2.3 Theoretical Works on Confined Phase Behavior

Experimental and theoretical approaches are both important methods to characterize the confined fluid phase behavior deviations. However, theoretical works, including the extended/modified EOS, molecular simulation, and density functional theory (DFT), are currently dominant because of the significant challenges and time consumption of experimental approaches. Numerous theoretical studies have enlightened our understanding of confined fluid systems and provided insightful ideas and basis for the experimental design.

2.3.1 Extended/modified EOS

The classic cubic equations of state (EOS) are not applicable to describe the confined fluid phase behavior because of the drastic deviations of confined fluid properties (Yang et al., 2018). Great efforts have been devoted to extending or modifying the classic EOS models, where different factors, such as capillary pressure, critical property shift, molecule-wall interaction, etc., have been incorporated to represent the effect of nanoscale confinement.

Capillary pressure

At nanoscale pores, the effect of capillary pressure is significant compared with that in bulk space. For unconventional reservoirs, not accounting for increased capillary pressure in small pores can lead to erroneous reserve estimation and inaccurate ultimate recovery (Nojabaei et al., 2013). Hence, capillary pressure is coupled with phase equilibrium equations to reflect the capillarity effect in nanopores (Sandoval et al., 2015, Yang et al., 2018), as shown below:

$$f(X)=\begin{cases}\ln K_i+\ln F_i^g(T,P^g,y_i)-\ln F_i^l(T,P^l,x_i); \\ \sum_i^{N_c}(y_i-x_i) \\ P^l-P^g+P_c(T,P^g,P^l,x,y)\end{cases}=0 \qquad (2.1)$$

where $K_i=y_i/x_i$, $F_i^{\alpha}=(P\varphi_i)^{\alpha}$, P^l, P^g, and P_c stand for the liquid phase pressure, gas phase pressure, and capillary pressure, x_i and y_i are the composition of liquid phase and vapor phase, respectively.

It is widely accepted that the incorporation of capillary pressure imposes changes to the whole phase diagram except at the critical point, although few researchers also claimed the unchanged cricondentherm (Nojabaei et al., 2013). Results demonstrate that both the bubble point pressure and the lower dew-point pressure are suppressed, while the upper dew point pressure is elevated (Sandoval et al. 2015; Yang et al., 2018).

Critical property shift

Critical property shift of confined fluids is widely observed in numerous experiments and simulation works (Yang and Li, 2019). The correlations of critical property shift with dimensionless pore size (r_p/σ_{LJ}) have been extensively established (Zarragoicoechea and Kuz, 2004; Tan et al., 2019). The shifted critical properties are calculated and incorporated into the phase equilibrium calculations for confined fluids.

$$\begin{cases} \Delta T_c^* = \dfrac{T_{cb} - T_{cp}}{T_{cb}} = 0.9409 \dfrac{\sigma_{LJ}}{r_p} - 0.2415 (\dfrac{\sigma_{LJ}}{r_p})^2 \\ \Delta P_c^* = \dfrac{P_{cb} - P_{cp}}{P_{cb}} = 0.9409 \dfrac{\sigma_{LJ}}{r_p} - 0.2415 (\dfrac{\sigma_{LJ}}{r_p})^2 \end{cases} \tag{2.2}$$

$$\begin{cases} \Delta T_c^* = \dfrac{T_{cb} - T_{cp}}{T_{cb}} = 0.0519 (\dfrac{\sigma_{LJ}}{r_p})^2 + 25.7585 (\dfrac{\sigma_{LJ}}{r_p})^4 \\ \Delta P_c^* = \dfrac{P_{cb} - P_{cp}}{P_{cb}} = 0.7689 \dfrac{\sigma_{LJ}}{r_p} + 28.7529 (\dfrac{\sigma_{LJ}}{r_p})^3 \end{cases} \tag{2.3}$$

Both experimental and simulation works have demonstrated that the critical pressure shift is higher than the critical temperature shift, which proves the inaccuracy of the correlations of Zarragoicoechea and Kuz (Tan et al., 2019, Yang and Li, 2020). It has been well recognized that the consideration of the shifted critical properties results in the overall shrinkage of the two-phase envelope (Yang et al., 2018).

Adsorption

Physical adsorption, as an important phenomenon in confined systems, cannot be ignored on influencing the fluid phase behavior in nanopores (Dong et al., 2016; Sandoval et al., 2018). Sandoval et al. (2018) investigated the effect of fluid adsorption by incorporating the adsorption film thickness into the calculation of the effective capillary radius.

$$f(X) = \begin{cases} \ln K_i + \ln F_i^g(T, P^g, y_i) - \ln F_i^l(T, P^l, x_i); \\ \sum_i^{N_c} (y_i - x_i) \qquad = 0 \text{ coupled with } r_c = r - t_a \\ P^l - P^g + \dfrac{2\sigma \cos\theta}{r_c} \end{cases} \tag{2.4}$$

The adsorption thickness enhances the capillary pressure between the liquid and gas phases by modifying the effective capillary radius inside a porous material. The increase of the capillary pressure becomes relevant in the bubble point branch far away from the critical point where the

interfacial tension is higher (Sandoval et al. 2018). Song et al. (2020), on the other hand, proposed to modify the molar volume term in PR EOS by considering the reduced mole number of fluids caused by adsorption and analyzed its induced shift in critical properties.

Molecule-wall interaction

The interaction between guest molecules and the nanopore wall is an important aspect of the confinement effect. Numerous works have been proposed to incorporate the molecule-wall interaction into the classic EOS models. These include the direct diminish from the attractive parameter (Yang et al., 2019), the microscopic descriptor (Wu et al., 2016), and the extra pressure term derived from statistical thermodynamic theory (Travalloni et al. 2014).

$$P = \frac{RT}{v-b} - \frac{a[1-3.374\times(r_p/\sigma_{LJ})^{-1.637}]}{v(v+b)+b(v-b)} \tag{2.5}$$

$$K_{fs} = K_h^{\exp[A(1-K_{ff})]} \begin{cases} a' = aK_{fs} \\ b' = b/K_{fs} \end{cases} \tag{2.6}$$

$$P = \frac{RT}{v-b_p} - \psi - \sum_{i=1}^{Nc}(x_i\theta_i\frac{x_ib_{p,i}}{v^2}(1-\frac{x_ib_{p,i}}{v})^{\theta_i-1}(1-F_{pa,i})\times(RT(1-\exp(-\frac{N_{av}\varepsilon_{p,i}}{RT}))-N_{av}\varepsilon_{p,i})) \tag{2.7}$$

The modified EOS models with consideration of the molecule-wall interaction can predict different phase configurations under confinement (Travalloni et al., 2014) and relate well the methane storage behavior within nanopores of different pore size and surface properties (Wu et al., 2016). Moreover, the effect of molecule-wall interaction can cause a significant overall shrinkage of the phase diagram of confined fluids (Yang et al., 2019; Yang and Li, 2020).

Combination of factors

Nanoscale confinement is not generally defined in the current works. All the above factors, including capillary pressure, critical property shift, adsorption, and molecule-wall interaction are

considered to partly represent the confinement effect. Numerous models have been proposed by combing different factors, as demonstrated in Table 2.3.

Table 2.3: Modified/extended EOS models with combined factors

References	EOS	Modification/extension	General assumptions or insights
Teklu et al. 2014	PR EOS	Critical property shift +capillary pressure	Bubble-point suppression; upper dew-point increase and lower dew-point decrease.
Zuo et al.2018	PR EOS	Critical property shift +capillary pressure	Modified Yong-Laplace equation with consideration of molecule-wall interaction.
Cui et al. 2018	PR EOS	Adsorption+ capillary pressure	Linear decrease of critical temperature and quadratic decrease of critical pressure, suppression of bubble-point pressure.
Sandoval et al.2018	PR EOS	Adsorption+ capillary pressure	Introduction of the excess adsorbed phase; Langmuir equation to model the adsorbed phase.
Yang et al. 2019	PR EOS	Molecule-wall interaction +capillary pressure	Exponential decrease of critical temperature; molecule-wall interaction causes shrinkage of two-phase envelope.
Song et al. 2020	PR EOS	Critical property shift +adsorption	Adsorption-dependent PR EOS and its induced critical properties shift correlations.

Despite all the works, how these factors should be combined to comprehensively reflect the confinement effect and whether some new factors should be included have barely been discussed. It is addressed in several works that the overall confinement effect consists of two essential aspects: (a) the molecule-wall interaction, which is the van der Waals forces arising from the interaction between guest molecules and the nanopore walls and (b) the geometric constraints which limit the number of guest molecules within nanopores, imposing size constraint effect on nucleation and crystal growth (Qian and Bogner, 2012) and causing variations to the effective molecular volume (covolume) (Derouane, 2007; Wu et al., 2016; Yang et al., 2020). Hence, molecule-wall interaction and geometric constraints are the two dominant factors of nanoscale confinement. However, the modification with respect to the geometric constraints has been sparsely seen in the existing work. To explore the variation of covolume in confined space and

further propose a more accurate EOS model for confined fluids, modification in terms of geometric constraints is required to be considered. The critical property shift, which is an important aspect of confined fluid phase behavior deviation, can be used to determine the introduced parameters in the modified/extended EOS models (Yang et al., 2019).

2.3.2 Molecular simulation

Molecular simulation, as a bridge between microscopic length/time scales and the macroscopic properties in the laboratory, has been widely used to investigate the dynamics and phase behavior of confined fluids. With its essence of achieving 'exact' predictions of the macroscopic properties by estimating the microscopic interactions, molecular simulation is capable of imposing valuable insights into truly microscopic level, usually not accessible by experiments (Patrykiejew 1996). Monte Carlo (MC) simulation and molecular dynamics (MD) simulation are the two widely seen approaches for phase equilibria calculations. The first type is mainly used to obtain phase diagrams, while the second type can be applied to achieve not only the static properties, but also dynamic properties based on time correlation functions (Wang 2010).

Monte Carlo (MC) simulation

MC is a stochastic method that allows efficient sampling of the multidimensional phase space of the system. With a probability proportional to the Boltzmann factor of the energy, the system goes from one configuration (state) to the next configuration (state) based on different types of moves that satisfy microscopic reversibility and preserve the macroscopic properties of the system. MC simulation particles are displaced randomly one at a time within the simulation box and the new configuration is accepted or rejected according to the Boltzmann factor of the energy difference between the two states (Economou 2004). To calculate the energy of each configuration

(state), the intermolecular interactions need to be specified and carefully truncated (Frenkel and Smit, 2002). Vishnyakov et al. (2001) studied the critical properties of Lennard-Jones fluid in slit-like pores by Gibbs ensemble Monte Carlo method and claimed a linear dependence of the critical temperature on the inverse of pore width. Jiang et al. (2004) simulated the phase transitions of n-alkanes confined in carbon nanotube by using the gauge-cell Monte Carlo method at a subcritical temperature and the coexisting vapor-liquid phases are determined from a Maxwell construction along the adsorption isotherm. Hamada et al. (2007) examined the correlation between the phase behaviors of a Lennard-Jones fluid in and outside a pore by grand canonical Monte Carlo (GCMC) simulations and claimed that the surface tension decreases linearly with the inverse of the pore diameter or width. Singh and Singh (2011) investigated the effect of pore shape and surface-fluid strength on the crossover behavior of critical properties of a square-well fluid and found that critical temperature approaches the 3D bulk value monotonically irrespective of the pore shape and surface. Lowry and Piri (2018) employed GCMC simulations to investigate the effects of three different pore types on the fluid phase behavior and thermodynamic properties of ethane. They concluded that the pore structure leads to distinct shifts in the confined critical temperature depending upon the level of pore material disorder and surface chemistry.

Molecular dynamics (MD) simulation

MD simulation consists of the step by step solution of the classical Newton's law of motion for many-particle systems, which can be written as (Allen 2004):

$$\mathbf{f}_i = -\frac{\partial}{\partial \mathbf{r}_i} u \tag{2.8}$$

The forces $\boldsymbol{f}_i$ acting on the atoms are usually derived from the potential energy u, which are defined by different empirical potential functions for various systems of practical interest. Molecules with

initial positions and velocities are exposed to collisions governed by the empirical potentials. The force acting on the molecules can be obtained from the summation of the spatial derivative of potentials. With the calculated force, the position and velocity of each molecule are updated within each step. The system behavior is concisely described by the evolution of all the molecules and desired properties can be easily extracted (Zhang et al., 2015). Wang (2010) investigated the melting point, surface tension of several model fluids by means of MD simulation and revealed new structures and transport behaviors of confined water. Moreover, the capillary condensation pressure of cylindrical nanopores with various pore sizes from 2 to 4 nm were determined by Miyahara et al. (2000) via a molecular dynamic technique. Monson (2012) demonstrated the formation of liquid phase from a liquid bridge between the pore walls by simulating the dynamics of capillary condensation in the duct pores. Wang et al. (2015) investigated the adsorption behavior of oil within nanoscale carbonaceous slits and illustrated the density oscillation from the pore surface to the central plane, which indicates the distinct adsorbed layers and bulk phase fluid. Sedghi and Piri (2018) studied the pressure of methane molecules confined in graphite pores of various sizes and demonstrated that the capillary condensation could be identified with abrupt drop in the pressure of the confined phase.

Molecular simulation has been well applied to investigate the shifted phase transitions of simple fluids at small scales, such as the critical property shift, the varied surface tension, and the dynamics of capillary condensation. This method can explicitly consider the intermolecular interactions and molecular configurations (Jin 2018). However, it is still currently a method more widely used to reflect the pore size effect with simplified pore chemistry. To establish a simulation model that can represent the real materials with surface heterogeneity, chemistry, and roughness is highly challenging. In addition, the variation of the surface properties regarding temperature,

pressure, and introduction of guest molecules is usually ignored. The intermolecular potentials are often assumed to be the same as those for the bulk and the importance of the electrostatic, induction, and three body and higher body interactions are often ignored (Gelb 1999). Most importantly, a slight increase in either fluid complexity (heavy hydrocarbons) or system scale imposes a large obligation for higher level of approximation, less reliable empirical force field, and much heavier computational cost, resulting in its inapplicability for complex mixtures in large system scales (González 2011; Travalloni et al., 2014).

2.3.3 Density functional theory (DFT)

As a generic method in quantum mechanics, classical density functional theory (DFT) offers a powerful alternative to a variety of conventional theoretical methods and molecular simulations (Wu 2006). Classical DFT stems from a mathematical theorem that the Helmholtz energy can be expressed as a unique functional of the density profiles of the constituent molecules, independent of the external potential. The grand potential, which is also a functional of the molecular density, is defined as

$$\Omega[\rho_i(\mathbf{R})] = F[\rho_i(\mathbf{R})] + \sum_i d\mathbf{R}\rho_i(\mathbf{R})[\psi_i(\mathbf{R}) - u_i] \tag{2.9}$$

Since the second law of thermodynamics requires that the grand potential be minimized at equilibrium, minimization of the grand potential functional yields a variational equation

$$\delta F[\rho_i(\mathbf{R})] / \delta\rho_i(\mathbf{R}) + \psi_i(\mathbf{R}) - u_i = 0 \tag{2.10}$$

Given an expression for the intrinsic Helmholtz energy functional, the equilibrium density profiles can be obtained by solving the above equation. Then, both structural and thermodynamic properties of the system can be calculated by following the standard statistical-mechanical

relations. DFT is useful not only for inhomogeneous systems that are subject to an external field but also for uniform systems such as conventional bulk vapor and liquid phases, and for anisotropic fluids such as liquid crystals. The practical value of DFT is reflected by its versatility for solving problems that may not be attained by conventional theories (Wu 2006), such as the confined fluid phase behavior investigation.

Inhomogeneous density distribution, as a typical characteristic of confined fluids, makes DFT a promising method to investigate the confined phase behavior (Salahshoor et al., 2018). A new DFT was proposed by Peng and Yu (2008) to yield accurate density distribution, adsorption-desorption isotherms, and capillary phase transitions for Lennard-Jones fluid confined in slit like pores with different widths and solid-fluid interactions. By combining with PR EOS, Li and Firoozabadi (2009) developed a DFT to investigate the interfacial tension of both pure and binary fluids over a wide range of pressures and temperatures. They also applied DFT to study the adsorption and phase behavior of pure substances and mixtures in nanopores with predicted adsorption data agrees well with experimental results (Li et al., 2014). After comparing the phase behavior of confined hydrocarbons in nanopores obtained by PR EOS with capillary effect and DFT, Liu et al (2017) claimed that assuming homogeneous distribution in nanopores might mislead the prediction of confined phase behavior. Jin (2018) studied the effect of pressure, temperature, and nanopore size on the bubble/dew point and adsorption hysteresis of confined hydrocarbons by using GCMC and DFT. He concluded that DFT reliably predicts the vapor-liquid equilibrium of confined hydrocarbon fluids.

Although the application of DFT is not as wide as the modified EOS models or molecular simulation because of its theoretical complexity, it is applicable to characterize the physical adsorption, inhomogeneous density distribution, and deviated phase transitions of confined fluids.

Compared with molecular simulation, DFT can obviously reduce the calculation time (Jin 2018). And the approximate expressions for the excess Helmholtz energy functional allow us to reflect most nonbonded interactions in a complex fluid. However, significant efforts are still required for the development of more accurate density functionals accounting for realistic intermolecular forces (Wu 2006). As a result, the effect of heterogeneous surface chemistry and pore geometry has rarely been reported by DFT. This, to some degree, may limit its accuracy in characterizing the confined fluid phase behavior in nanoconfined systems.

Theoretical works, as a significant and mandatory supplement of the experimental approaches for investigating the confined phase behavior, have revolutionized our understanding of confined fluid systems. Table 2.4 lists a generalized comparison of three different theoretical approaches. Firstly, unlike molecular simulation or DFT, modified/extended EOS models are not associated with sophisticated theoretical background, which makes it easily accessible by numerous researchers. Secondly, although molecular simulations can predict results not accessible by current state-of-the-art experimental instruments, they are usually computationally expensive and time consuming. In contrast, modified/extended EOS models provide instantaneous calculation results and identifies the effect of the key physical parameter, and yields general predictions and observations as well, which makes it more eligible for industrial applications. As for DFT, it can properly bridge the gap between molecular simulations and modified/extended EOS with modest computational cost (Wu et al., 2016). Thirdly, although all three approaches are applicable for investigating the pore size effect, molecular simulation is the only method that can establish realistic models of nanopores with surface roughness, heterogeneity, and pore size distribution (Sonwane et al., 2005; Coasne et al., 2006). It is highly required that the force field represents accurately the inter- and intramolecular interactions to make the simulation results

accurate and match well with the experimental results (Economou 2004). Lastly, limited by the theoretical complexity and computational cost, both molecular simulation and DFT are better suitable for simple fluid systems of small scales. While the modified/extended EOS approach can potentially be applied for highly complicated systems in field scale, such as unconventional reservoirs.

Table 2.4: Comparison of different theoretical approaches

Theoretical methods	Theoretical Complexity	Computational cost	Pore size effect	Pore geometry	Surface chemistry	Complicated systems	Field application
Modified/ extended EOS	Low	Low	Yes	Barely	Barely	Yes	Yes
Molecular simulation	High	High	Yes	Yes	Yes	No	No
Density Functional Theory	High	Modest	Yes	Barely	Barely	No	No

2.4 Confinement in Unconventional Reservoirs

Unconventional reservoirs are dominated by microscale pores. The pore size distribution (PSD) imposes significant effect on both the storage and transport phenomenon of confined reservoir fluids (Sigal, 2015; Zhang 2019). Different radiation and fluid invasion approaches, including the field-emission scanning electron microscopy (FE-SEM), X-ray computed tomography (CT), small (ultra-small) angle neutron scattering techniques (SANS/USANS), and nuclear magnetic resonance (NMR), have been adopted to characterize the pore size of unconventional reservoirs. Loucks et al. (2009) illustrated back-scattered SEM images of nanometer-scale pores associated with clays and kerogen in Barnett shale and revealed pores as small as 4 nm. Javadpour (2009) used the AFM technique to reflect pores and grooves with dimensions of about a few nanometers associated with clays. Kuila et al. (2011) studied the PSD in shales using a nitrogen adsorption technique and claimed that shale matrix has predominantly

micro (pores less than 2 nm diameter) to meso-pores (pores with 2-50 nm diameter) highly associated with clay minerals and organic matter. Clarkson et al. (2013) characterized the pore structure of typical shale gas reservoirs using SANS/USANS, gas adsorption, and mercury intrusion. They concluded that the results of SANS/USANS and gas adsorption are in good agreement and the accessible porosity is pore-size dependent. Zhang et al. (2019) determined the PSD of multiple shale samples with four different techniques and concluded that the PSD of shale reservoirs are widely ranging from micropores to macropores (> 1000 nm). Essentially, the widespread nanoscale pores induce strong confinement effect to the constrained hydrocarbons, resulting in significant deviations to both the phase and transport behavior of confined reservoir fluids, which imposes further impact on the reserve estimation, primary production, and enhanced oil recovery (EOR) of unconventional reservoirs.

2.4.1 Reserve estimation

Reserve estimation is significant for reservoir-engineering analysis in both conventional and unconventional reservoirs (Ambrose et al. 2012). The complex PSD in shale reservoirs significantly influences the storage of shale hydrocarbons, which in turn determines the accuracy of reserve estimation. In conventional reservoirs, once pore volume is known, the amount of fluid in place can be easily estimated. In unconventional reservoirs, however, the confined fluids can potentially exist in multiple different phases, as shown in Figure 2.11, causing drastic uncertainty to the reserve estimation by using volumetric method. Ambrose et al. (2012) illustrated different thermodynamic states of shale gas in nanopores and formulated a new gas in place (GIP) equation by combining Langmuir adsorption isotherm with volumetric method. Jin and Firoozabadi (2016) demonstrated the three different states of fluid molecules in shale media: free, adsorbed, and

dissolved molecules and concluded that species dissolution in kerogen may provide an additional fluid in place mechanism in shale formations. Furthermore, capillary condensation has also been proved to be significant for reserve estimation in shale reservoirs. Chen et al. (2012. 2013) verified the occurrence of capillary condensation in kerogen pores and proved that capillary condensation is an important storage mechanism in organic-rich shale formations. Li et al. (2014) extended the GIP model with capillary condensation to a high-pressure range and pointed out that the GIP can be underestimated by more than 10% with the conventional model. Moreover, Zhang and Ionkina (2018) introduced capillary condensation in nano-scale pores as the third component to the conventional GIP model, which predicted an increase of nearly 300% in gas reserve.

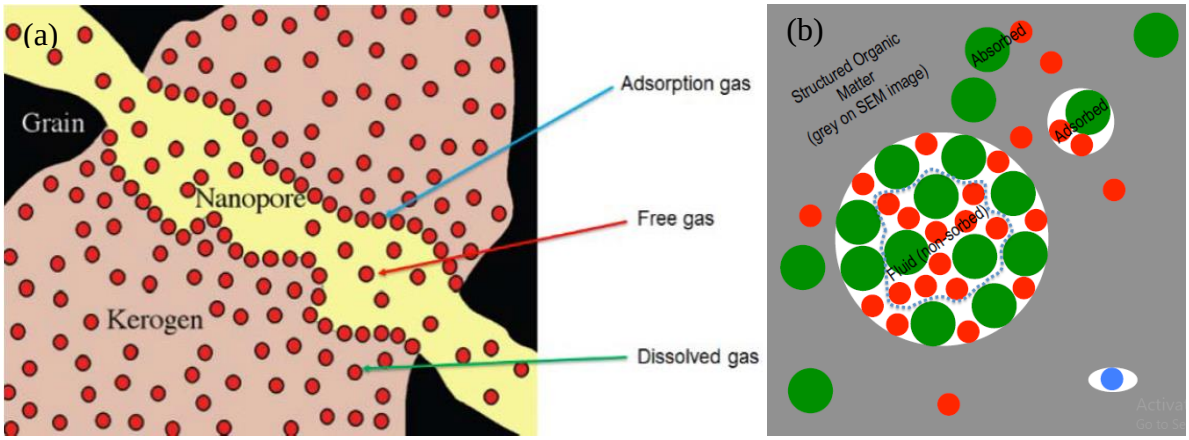

Figure 2.11: Schematic diagram of organic matrix storage in unconventional reservoirs. (a) Shale gas reservoir (Guo 2015); (b) Shale oil reservoir (Pepper et al., 2019) (green “oil” molecules, red “gas” molecules, blue water molecules).

2.4.2 Unconventional hydrocarbon recovery

The success of shale hydrocarbon recovery is highly attributed to horizontal drilling and hydraulic fracturing. However, factors related to the reservoir formation and confined reservoir fluid should also be taken into consideration. Limited by the extremely low matrix permeability, the presence of interconnected microfractures is an important contributing factor for the fluid flow

in shale reservoirs (Kurtoglu and Kazemi 2012). In addition, low-viscosity and high-compressibility hydrocarbon fluids, abnormally high initial pressure, and favorable phase envelope shift are all reasons of successful hydrocarbon production in shale formations (Kurtoglu et al. 2013). In shale gas reservoirs, gas desorption is proved to be an important recovery mechanism, leading to improved gas recovery (Cipolla et al. 2010; Yu and Sepehrnoori, 2014). Thomson et al. (2011) showed that desorption gas accounts for 17% of the expected ultimate recovery and Arogundade and Sohrabi (2012) claimed that 5-15% of the total gas production is desorption gas. For gas-condensate systems, a large gas-to-oil volume split in the nano and meso-pores plays a crucial role in hydrocarbon recovery during depletion (Alharthy et al. 2013). Consequently, the use of bulk fluid measurement in modeling and predicting the performance of unconventional reservoirs result in significant underestimation of the reservoir potential (Firincioglu, 2013).

Considering the dominance of nanopores, the favorable phase envelope shift is an important contributing factor for unconventional reservoir production, as demonstrated in Figure 2.12. For shale oil reservoir, the suppressed bubble-point pressure results in the late evolution of solution gas, providing a wider favored operation window, a higher liquid saturation and therefore higher oil production. While for the gas condensate reservoirs, the suppressed upper dew-point pressure delays the condensation of the supercritical fluid, causing hydrocarbon mixture to produce with minimal liquid dropout and therefore higher gas production. Alharthy et al. (2013) introduced the critical properties shift into a dual-permeability compositional model to investigate the hydrocarbon production of unconventional reservoirs. Stimpson et al. (2017) proved that capillary pressure significantly impacts simulated oil and gas production from unconventional reservoirs. Furthermore, the impact of both capillary pressure and critical property shift on hydrocarbon production were analyzed in multiple realistic scenarios of shale reservoirs by Haider and Aziz

(2017). Their findings indicate that the impact of different factors on hydrocarbon production is influenced by variations of shale reservoir and fluid properties.

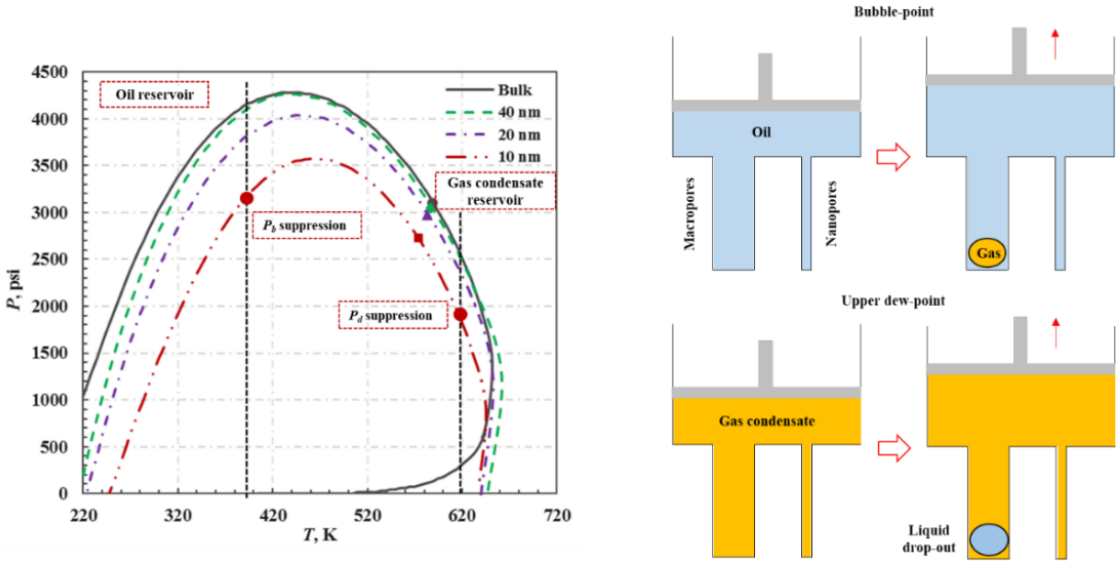

Figure 2.12: Conceptual demonstration of different phase behavior paths in the depletion process of unconventional reservoirs with confined property shift (Yang et al. 2019). As pressure decreases, both the appearance of evaporation and condensation are delayed in nanopores, late evolution of solution gas and liquid drop-out in nanopores are favorable for the production of shale oil and gas condensate reservoir, respectively (Kurtoglu et al. 2013).

2.4.3 Enhanced oil recovery in unconventional reservoirs

With the primary recovery factor of unconventional reservoirs as low as 1/3 of the conventional reservoirs, enhanced oil recovery (EOR) has attracted great attention in recent years. Gas huff-n-puff with CO_2 or natural gas injection is proved to be the most promising approach. Like in conventional reservoirs, three processes are included for gas huff-n-puff in unconventional reservoirs: gas injection, soaking and production. For each huff-n-puff cycle, gas injection is followed by well shut-in as the soaking time, and then the well is put back into production before

the next cycle starts. Hawthorne et al. (2013) proposed mechanisms controlling CO_2 EOR in Bakken formations, as shown in Figure 2.13, and experimentally demonstrated that nearly complete (>95%) hydrocarbon recovery can be achieved from Bakken shale. Gamadi et al. (2014) conducted laboratory study using shale cores from Mancos and Eagle Ford to evaluate the performance of cyclic CO_2 injection. They concluded that cyclic CO_2 injection improved recovery of shale oil cores from 33% to 85% depending on the shale core type and operating parameters. Alharthy et al. (2018) presented both laboratory and numerical modeling of EOR in Bakken shale cores by injecting carbon dioxide, methane/ethane mixture, and nitrogen. They demonstrated that the experiments recovered 90+% oil from several Middle Bakken cores and nearly 40% from Lower Bakken cores. Despite the unsatisfactory performance of some field pilot tests of CO_2 huff-n-puff in Bakken shale (Hoffman and Evans, 2016; Yang and Li, 2020), the natural gas injection in Eagle Ford shale turned out to be highly successful (Hoffman 2018).

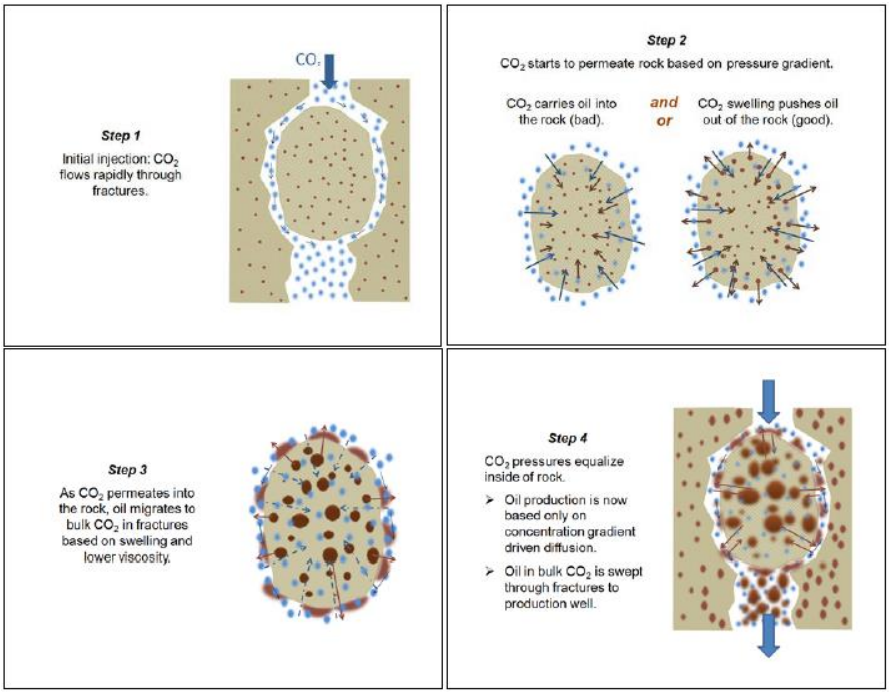

Figure 2.13: Conceptual steps for CO_2 EOR in fractured tight reservoirs (Hawthorne et al. 2013).

Like in primary production, nanoscale confinement is highly essential for the compositional simulation and operational design of EOR processes in unconventional reservoirs. However, some of the current works fail to consider the nanoscale confinement, others reflect it by the critical properties shift of confined fluid systems. Yu et al. (2019) simulated the CO_2 huff-n-puff process in an Eagle Ford well by considering the molecular diffusion and critical properties shift. The relative increase of the cumulative oil production for 20 years was approximately 12%. Shabib-Asl et al. (2020) investigated the effect of pore confinement on the incremental recovery of CO_2 huff-n-puff in shale formations by considering the critical properties shift. Their results demonstrated that the nanoscale confinement has a significant impact on the production forecasts of unconventional reservoirs. In the current works, the widely used method to calculate the critical properties shift is the correlations of Zarragoicoechea and Kuz (2004), which have been experimentally and theoretically proved not accurate (Tan et al., 2019; Yang et al., 2019). More reliable correlations for the critical properties shift calculation need to be established. In summary, nanoscale confinement is a significant aspect for both the primary and gas injection EOR simulations of unconventional reservoirs and further work needs to be conducted to accurately reflect its overall effect.

Confinement effect on minimum miscibility pressure (MMP)

Minimum miscibility pressure (MMP), which is defined as the lowest pressure above which the injected gas and the reservoir fluid achieve dynamic miscibility, is an important parameter for evaluating the feasibility of the miscible gas injection EOR in unconventional reservoirs. A widely used and accurate approach to measure the MMP is the slim-tube method (Yellig and Metcalfe 1980), other experimental approaches include the rising bubble apparatus (Christiansen and Haines 1987) and the vanishing interfacial tension technique (Rao 1997).

Several theoretical approaches are also available to estimate MMP, including the slim-tube simulation, multiple mixing cell calculation, EOS based method, and empirical correlations. In recent years, confinement effect on MMP within nanopores has been widely investigated. Teklu et al. (2014) applied the multiple mixing cell algorithm and the modified VLE procedure to determine the MMP of Bakken oil with CO_2 injection and concluded that MMP is suppressed under confinement. Zhang et al. (2017) proposed a diminishing interface method (DIM) to determine the MMP of light oil-CO_2 systems in both bulk and nanopores. The MMPs of the Pembina live light oil-CO_2 system in nanopores with radius of 100, 20, and 4 nm are 15.4 (2233.58), 13.7 (1987.02), and 13.4 (1943.51) MPa (psi), respectively. Zhang et al. (2020) investigated the effect of capillary pressure on MMP for tight reservoirs and claimed that the change of MMP does not go beyond a couple hundred psi. Yang and Li (2020) calculated the MMP of 100% CO_2 injection into Eagle Ford shale condensate reservoir by combining the vanishing interfacial tension (VIT) algorithm with a modified PR EOS. The values of 20 nm and 10 nm are 3553 psi and 3263 psi, respectively.

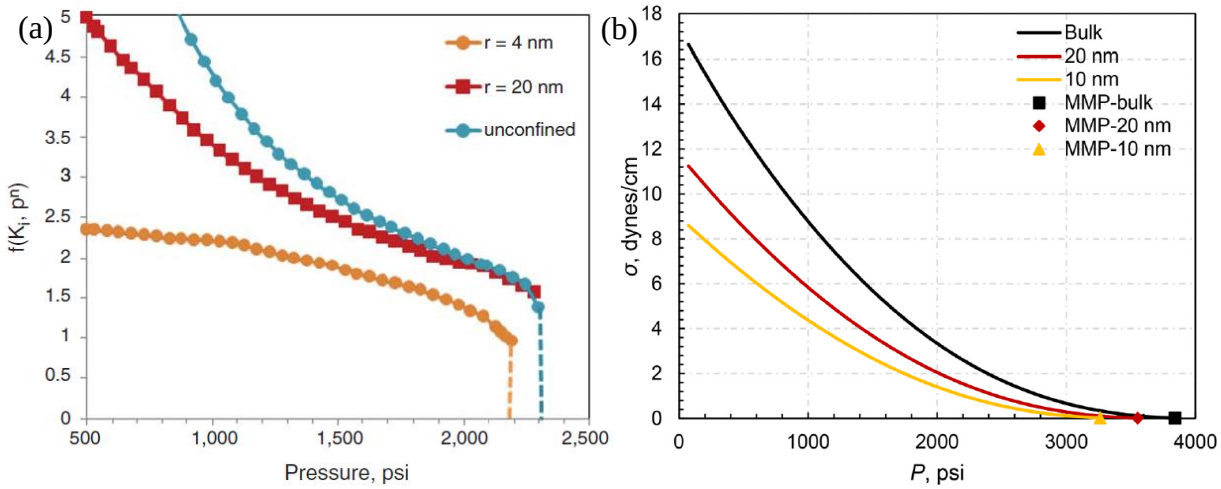

Figure 2.14: MMPs of shale hydrocarbons and CO_2 injection by different methods. (a) Multiple mixing cells (Teklu et al., 2014); (b) Vanishing interfacial tension (Yang and Li, 2020).

2.5 Summary

Confined fluid phase behavior has been extensively studied by numerous experimental and theoretical approaches. Significant insights have been revealed to revolutionize our understanding of the dynamics and phase transitions within confined systems, which can be summarized as below:

- ✓ Confinement imposes contortion or rearrangement to the encapsulated molecules, which in turn affects the dynamics and properties of confined fluids.
- ✓ Confinement induces unusual phase behavior to the confined fluids, including capillary condensation or unique nanotube ice in water.
- ✓ Confined phase behavior deviates significantly from that of bulk fluids, including the critical property shift, the saturation pressure shift, and the two-phase diagram shift.
- ✓ Confinement reflects a counterbalance between geometric constraints and molecule-wall interaction, which is highly dependent on both pore size and pore chemistry.
- ✓ Confinement tends to be negligible at a critical pore size, the value of which is not universally defined in the current works.

Despite the widely accepted conclusions, there also exist some controversial and even conflicting results among current works: such as the shift of dew-point pressure in confined systems, the mechanisms underlying capillary hysteresis, and the accurate correlations defining confined critical properties shift. Further experimental and theoretical works need to be conducted to obtain highly convincing results.

With respect to the unconventional reservoirs, it is widely accepted that the strong confinement effect resulted from the dominance of nanoscale pores has significant effect on both the reserve estimation and the unconventional hydrocarbon recovery.

- ✓ Different storage states and existence of capillary condensation in confined reservoir fluids impose additional mechanisms to the reserve estimation of unconventional reservoirs.
- ✓ Favorable phase envelope shift, such as the bubble-point pressure suppression, is an important contributing factor for the economical production of unconventional reservoirs.
- ✓ Nanoscale confinement is highly essential for the compositional simulation and operational design of unconventional EOR processes.

The general conclusions about confined phase behavior can be instructive for the development of unconventional reservoirs. However, because of its high complexity and heterogeneity, shale has rarely been used in current experimental approaches, such as DSC or nanofluidic chips. Although crushed shale is applicable for the nanoscale adsorption isotherm, capillary condensation of confined fluids within shale has sparsely been reported. One promising focus of the future work is to propose creative ways to combine shale with applicable experimental approaches, aiming to provide direct observations of the confined phase behavior of reservoir fluids under actual reservoir conditions.

Chapter 3: Modified PR EOS for Confined Fluid Phase Behavior

This chapter is to establish a modified PR EOS with consideration of the confinement effect on both attractive parameter and covolume to describe the phase behavior of confined fluid systems within nanopores (Yang and Li, 2020a). The modification to attractive parameter illustrates the competition of the molecule-wall interaction against the intermolecular interaction, while the modification to covolume represents the effect of geometric constraints within confined space. Phase behavior of CO_2+*n*-C_4H_{10} and CO_2+*n*-$C_{10}H_{22}$ binary mixtures, CO_2+*n*-C_4H_{10}+*n*-$C_{10}H_{22}$ ternary mixture, and CO_2+Eagle Ford condensate are calculated by using the modified PR EOS, which will provide practical instructions for the design and optimization of the CO_2 EOR in shale reservoirs. This chapter is organized as follows: the modeling methodology section elaborates the modification of both the attractive parameter *a* and covolume *b* with application of the proposed critical property shift correlations; followed by the results and discussion section, where the phase diagrams of several CO_2-hydrocarbon systems are calculated and discussed.

3.1 Modeling Methodology

As one of the most widely used cubic EOS in petroleum industry (Li et al., 2016, 2017), the PR EOS demonstrates satisfactory prediction of bulk fluid phase behavior and liquid-density prediction (Whitson and Brulé, 2000). The original PR EOS is presented in Equations (3.1) to (3.4), which is the basic thermodynamic model in this work.

$$P = \frac{RT}{v-b} - \frac{a}{v(v+b)+b(v-b)} \tag{3.1}$$

$$a = 0.45724\frac{R^2T_c^2}{P_c}\alpha \tag{3.2a}$$

$$b = 0.07780\frac{RT_c}{P_c} \tag{3.2b}$$

$$\alpha = [1+\kappa(1-\sqrt{T_r})]^2 \tag{3.3}$$

$$\kappa = 0.37464 + 1.54226\omega - 0.26992\omega^2 \tag{3.4}$$

where R is the universal gas constant; v is the molar volume; P and T are pressure and temperature, respectively; T_c and P_c are the critical temperature and pressure, respectively; a and b are constants describing attractive force and the covolume, respectively; and α is a dimensionless function of reduced temperature (T_r) and acentric factor (ω).

For a mixture system, van der Waals mixing rules are used to calculate the parameters a and b in this work,

$$a = \sum_i \sum_j x_i x_j (a_i a_j)^{0.5}(1-\delta_{ij}) \tag{3.5}$$

$$b = \sum_i x_i b_i \tag{3.6}$$

where x_i and x_j are the compositions of the ith and jth component, respectively, and δ_{ij} is the binary interaction parameter between the ith and jth components.

3.1.1 Modified PR EOS

In the original PR EOS, the parameter a is regarded as a measure of the intermolecular attraction force, which can be interpreted as the attractive component of pressure. While the parameter b accounts for the actual volume of fluid molecules, also referred as the covolume (effective molecular volume). The term of $RT/(v-b)$ in Equation (1) represents the repulsive component of pressure on a molecule scale (Whitson and Brulé, 2000). The intermolecular interaction and the actual molecular volume are combined as the real gas effect. Since the pore

size and the size of fluid molecules are comparable to each other in confined space, the interaction between fluid molecules and the pore walls, along with the geometric constraints on the confined volume cannot be neglected, as demonstrated in Figure 3.1. The nanoscale confinement is reflected by the molecule-wall interaction and the geometric constraints, both of which impose significant effect on confined fluid phase behavior.

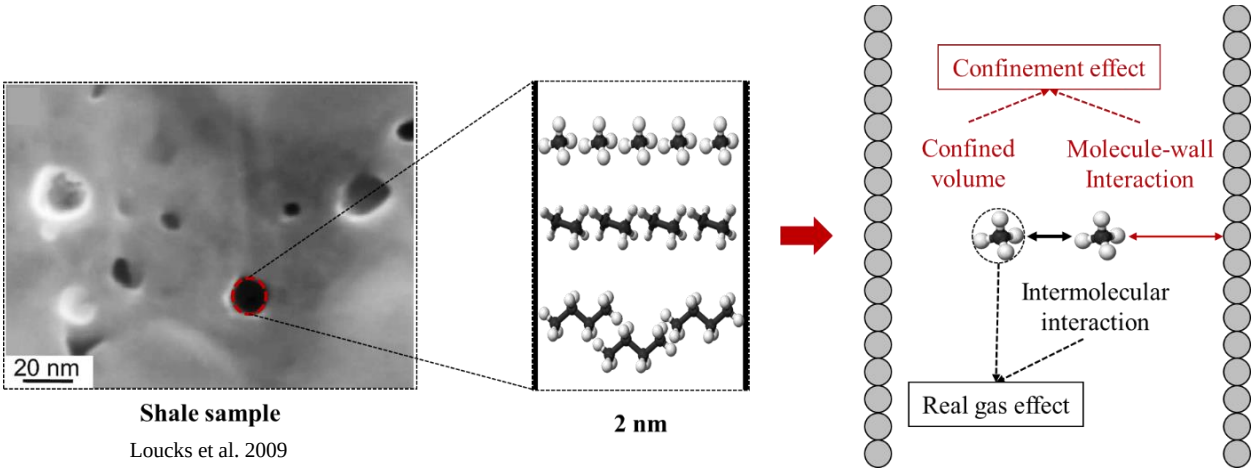

Figure 3.1: Schematic demonstration of nanoscale confinement

Based on the demonstration in Figure 3.1, this work proposed modifications to both the attractive parameter *a* and covolume *b* to reflect the effect of molecule-wall interaction and geometric constraints, respectively. The modified PR EOS is expressed with the following equations:

$$P = \frac{RT}{v - b_c} - \frac{a_c}{v(v + b_c) + b_c(v - b_c)} \tag{3.7}$$

$$a_c = 0.45724 \frac{R^2 T_{cc}^2}{P_{cc}} \alpha \tag{3.8a}$$

$$b_c = 0.07780 \frac{RT_{cc}}{P_{cc}} \tag{3.8b}$$

where a_c and b_c are the attractive parameter and the covolume in the confined space, respectively. While P_{cc} and T_{cc} are the critical pressure and critical temperature in the confined space, respectively. The parameters a and a_c are assumed to share the same α function. The modified EOS carries the similar expression as the original one for the convenience of application. Only the attractive parameter a and covolume b need to be replaced by the confined values, respectively.

A molecule-wall interaction term c is introduced to compete against the intermolecular interaction term a. Since the molecule-wall interaction in a confined system is essentially the interaction between fluid molecules and the molecules of pore walls, the term c can be introduced directly to diminish the attractive parameter a (Derouane 2007). We also propose to modify the covolume parameter b in this work by considering the confinement effect on the effective molecular volume, representing the geometric constraints within confined space. The equation for the confined attractive parameter a_c and the confined covolume b_c are demonstrated in Equations (3.9a) and (3.9b), respectively:

$$a_c = a - c \tag{3.9a}$$

$$b_c = b\beta \tag{3.9b}$$

where c represents the diminishment of the attractive parameter a under the impact of molecule-wall interaction and β is defined as the covolume ratio representing the ratio of the covolume between the confined fluid and the bulk fluid. Then the proposed EOS can be expressed as:

$$P = \frac{RT}{v - \beta b} - \frac{a - c}{v(v + \beta b) + \beta b(v - \beta b)} \tag{3.10}$$

3.1.2 Determination of β and c

Derivation of expressions for β and c

Combing Equations (3.8a) and (3.9a), (3.8b) and (3.9b) yields:

$$a_c = a - c = 0.45724 \frac{R^2 T_{cc}^2}{P_{cc}} \alpha \tag{3.11a}$$

$$b_c = b\beta = 0.07780 \frac{RT_{cc}}{P_{cc}} \tag{3.11b}$$

Based on Equations (3.11a) and (3.11b), T_{cc} and P_{cc} can be expressed as:

$$T_{cc} = 0.17015 \frac{a - c}{\alpha \beta R b} \tag{3.12a}$$

$$P_{cc} = 0.01324 \frac{a - c}{\alpha \beta^2 b^2} \tag{3.12b}$$

Thus, the critical properties shift can be calculated as follows:

$$\Delta T^* = \frac{T_c - T_{cc}}{T_c} = 1 - (1 - \frac{c}{a}) \frac{1}{\beta} \tag{3.13a}$$

$$\Delta P^* = \frac{P_c - P_{cc}}{P_c} = 1 - (1 - \frac{c}{a}) \frac{1}{\beta^2} \tag{3.13b}$$

Combing Equations (3.13a) and (3.13b) yields:

$$\beta = \frac{1 - \Delta T^*}{1 - \Delta P^*} = \left(\frac{T_{cc}}{T_c} \right) / \left(\frac{P_{cc}}{P_c} \right) \tag{3.14}$$

$$c = a \left[1 - \beta (1 - \Delta T^*) \right] \tag{3.15}$$

Based on Equations (3.14) and (3.15), both parameters β and c can be determined using the critical temperature and critical pressure shift data.

Correlation of critical properties shift

The critical properties shift, as an important aspect of confined fluid phase behavior deviation, has been demonstrated in numerous experimental and simulation results (Yang et al.,

2019). Table 3.1 lists 63 critical temperature shift (ΔT^*) data points of 9 different fluids (Ar, N_2, O_2, CO_2, CH_4, C_2H_4, C_2H_6, Lattice gas, and square-well fluid) by both experimental and simulation method. In addition to ΔT^*, the pore size r_p, the Lennard-Jones molecular size parameter σ_{LJ}, the dimensionless pore size r_p/σ_{LJ}, the critical temperature at bulk conditions T_c, and the critical temperature of confined fluids T_{cc} are also presented. The first 58 data points are used to establish the correlation between the critical temperature shift (ΔT^*) and the dimensionless pore size (r_p/σ_{LJ}), while the last 5 data points of five different fluids (Ar, N_2, O_2, CO_2, and C_2H_4) are applied to validate the predictability of the proposed model. Table 3.2 lists 40 critical pressure shift (ΔP^*) data points of 5 different fluids (CO_2, C_2H_6, C_4H_{10}, C_8H_{18}, and square-well fluid) at different pore sizes, which also includes both experimental and molecule simulation data. The pore shape (slit or cylinder), the pore chemistry (hard or attractive), and the dimensionless pore size (r_p/σ_{LJ}) are also listed. In Table 3.2, the first 34 data points are applied to obtain the correlation between the critical pressure shift (ΔP^*) and the dimensionless pore size (r_p/σ_{LJ}), while the last 6 data points of two different fluids (CO_2 and C_2H_6) are used to validate the proposed model. It's worth noting that the critical properties shift (both critical temperature and critical pressure) in this work are generally correlated with the dimensionless pore size only, regardless of the pore geometry, or pore chemistry because of the limited data points available.

Table 3.1: Critical temperature shift with the confinement effect

References	Method	No. of data points	Fluid	r_p [nm]	σ_{LJ} [nm]	$\frac{r_p}{\sigma_{LJ}}$	T_c [K]	T_{cc} (reported) [K]	ΔT^*	T_{cc} (calculated) [K]	Relative deviation [%]	Overall deviation[%]
Burgess et al., 1990	Experiment	1	CO_2	3.18	0.41	7.8	304.21	261.46	0.141	273.071	4.441	
Dillmann, 2001	Lattice simulation	7	Lattice gas	-	-	4	4.51	3.8705	0.142	3.351	13.434	
						8		4.2409	0.060	4.064	4.167	
						12		4.3561	0.034	4.255	2.318	
						16		4.4084	0.023	4.339	1.583	
						24		4.4549	0.013	4.412	0.963	
						28		4.4665	0.010	4.431	0.800	
						32		4.4749	0.008	4.444	0.688	
Vishnyakov et al., 2001	Molecular simulation	7	CH_4	-	0.38	10	190.6	169.44	0.111	176.750	4.314	
						8.5		165.25	0.133	173.271	4.854	
						7.5		161.63	0.152	170.006	5.182	
						7		160.68	0.157	167.951	4.525	
						6.5		153.43	0.195	165.514	7.876	
						6		151.91	0.203	162.586	7.028	
						5		108.45	0.431	154.578	42.534	
Singh and Kwak, 2007	Molecular simulation	4	SW	-	-	4	1.225	1.015	0.172	0.910	10.338	
						8		1.143	0.067	1.104	3.420	
						12		1.177	0.039	1.156	1.803	
						16		1.201	0.020	1.178	1.878	
Jana et al., 2009	Molecular simulation	12	SW	-	-	10	1.809	1.703	0.059	1.678	1.506	
						8		1.658	0.084	1.630	1.650	
						6		1.617	0.106	1.543	4.590	
						4		1.438	0.205	1.344	6.565	
						3		1.287	0.289	1.117	13.156	
						2.5		1.192	0.341	0.920	22.822	
						2		0.984	0.456	0.599	39.058	
						1.9		0.896	0.505	0.511	42.991	6.483
Singh and Singh, 2011	Molecular simulation	10	SW	-	-	40	1.22	1.209	0.009	1.207	0.174	
						30		1.204	0.013	1.201	0.290	
						20		1.193	0.022	1.186	0.594	
						16		1.183	0.03	1.174	0.792	
						12		1.158	0.051	1.151	0.600	
						8		1.091	0.106	1.099	0.771	
						6		1.021	0.163	1.041	1.928	
						5		0.9424	0.228	0.989	4.990	
						4		0.841	0.311	0.906	7.771	
						3		0.8099	0.336	0.754	6.948	
Didar and Akkutlu, 2013	Molecular simulation	4	CH_4	4.1	0.38	10.79	190.6	177	0.071	178.128	0.637	
				3.7		9.74		170	0.108	176.231	3.665	
				2.9		7.63		168	0.119	170.494	1.485	
				1.5		3.95		150	0.213	140.696	6.203	
Pitakbunkate et al., 2014	Molecular simulation	7	CH_4	1	0.38	2.63	190.45	99	0.480	103.228	4.270	
				2		5.26		127	0.333	156.914	23.555	
				3		7.89		155	0.186	171.278	10.502	
				4		10.53		169	0.113	177.556	5.063	
				5		13.16		175	0.081	180.971	3.412	
				6		15.79		178	0.065	183.078	2.853	
				7		18.42		181.5	0.047	184.490	1.647	
Jin and Nasrabadi, 2016	Molecular simulation	6	CH_4	10	0.38	26.32	190.6	185.195	0.029	186.953	0.949	
				7		18.42		182.545	0.043	184.635	1.145	
				4		10.53		174.909	0.083	177.696	1.593	
			C_2H_6	10	0.44	22.73	305.3	295.268	0.033	298.149	0.976	
				7		15.91		292.050	0.043	293.605	0.532	
				4		9.09		273.880	0.103	279.999	2.234	
Morishige and Shikimi, 1998	Experiment	5	Ar	1.2	0.34	3.53	150.7	98	0.350	104.658	6.794	8.403
			N_2		0.37	3.24	126.2	87	0.311	82.875	4.742	
			O_2		0.35	3.43	154.58	102	0.340	105.426	3.359	
			C_2H_4		0.44	2.73	282.34	184	0.348	159.249	13.452	
			CO_2		0.41	2.93	304.21	213	0.300	183.890	13.666	

Table 3.2: Critical pressure shift with the confinement effect

References	Method	No. of data points	Fluid	Material	Shape	$\frac{r_p}{\sigma_{LJ}}$	ΔP^* (reported)	ΔP^* (calculated)	Relative deviation [%]	Overall deviation [%]
Singh et al., 2009	Molecular simulation	6	C_4H_{10}	Mica	slit	3.514	0.306	0.431	40.879	27.838
						2.334	0.640	0.600	6.152	
						1.868	0.754	0.718	4.719	
						1.401	0.837	0.906	8.213	
						1.330	0.846	0.945	11.608	
						1.283	0.831	0.973	17.061	
		6		Graphite		5.862	0.106	0.285	170.364	
						4.680	0.269	0.342	27.171	
						3.506	0.525	0.432	17.738	
						2.334	0.794	0.600	24.405	
						1.871	0.856	0.717	16.159	
						1.401	0.890	0.906	1.828	
						1.354	0.874	0.931	6.530	
		4	C_8H_{18}	Mica		2.431	0.427	0.581	36.128	
						1.618	0.683	0.806	18.104	
						1.296	0.800	0.965	20.603	
						1.133	0.815	1.075	31.838	
		4		Graphite		3.246	0.374	0.460	22.911	
						2.438	0.630	0.579	8.081	
						1.621	0.859	0.805	6.235	
						1.296	0.852	0.965	13.177	
Singh and Singh, 2011	Molecular simulation	7	SW	Hard	slit	2	0.582	0.680	16.753	
						4	0.441	0.389	11.971	
						8	0.253	0.222	12.374	
						12	0.181	0.160	11.331	
						16	0.120	0.127	5.363	
						20	0.082	0.106	29.764	
						30	0.051	0.076	50.487	
		7			cylindrical	3	0.846	0.496	41.424	
						4	0.714	0.392	45.130	
						6	0.577	0.280	51.497	
						8	0.424	0.222	47.610	
						10	0.321	0.185	42.287	
						12	0.210	0.160	23.894	
						16	0.172	0.127	25.706	
						24	0.060	0.092	52.704	
						30	0.054	0.076	42.735	
Tan et al., 2019	experiment	6	CO_2	SBA	cylindrical	10.05	0.100	0.185	84.312	39.248
						7.48	0.162	0.234	44.716	
						5.63	0.303	0.295	2.850	
			C_2H_6			10.37	0.113	0.180	58.687	
						7.69	0.159	0.229	44.545	
						5.80	0.287	0.288	0.380	

By applying the collected experimental and simulation data in Tables 3.1 and 3.2, the correlations between the critical properties shift and the dimensionless pore size can be obtained and demonstrated in Figure 3.2.

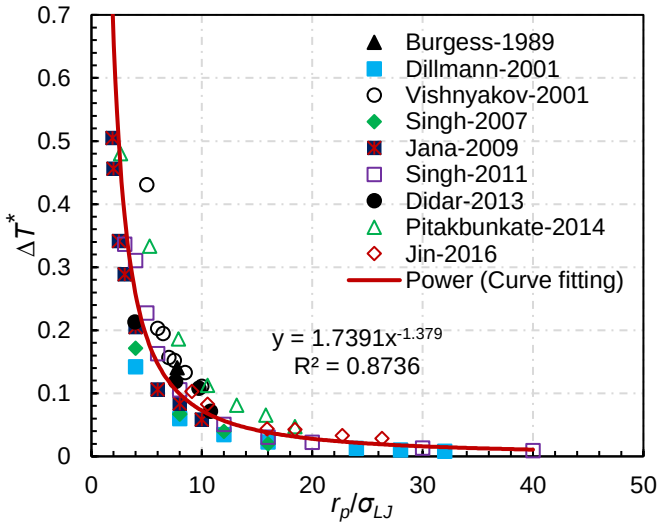

(a) Critical temperature

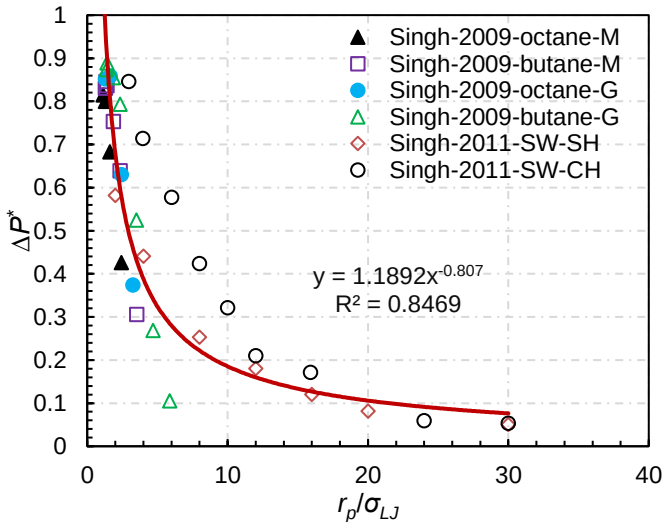

(b) Critical pressure

Figure 3.2: Critical properties shift with dimensionless pore size

As demonstrated in Figure 3.2, the correlations of critical properties shift with dimensionless pore size are:

$$\Delta T^* = 1.7391 \times (r_p / \sigma_{LJ})^{-1.379} \tag{3.16}$$

$$\Delta P^* = 1.1892 \times (r_p / \sigma_{LJ})^{-0.807} \tag{3.17}$$

With application of the critical properties shift correlations, the covolume ratio β and the molecule-wall interaction term c can be calculated with Equations (3.14) and (3.15) when a specific fluid is confined in a nanopore with known pore size r_p. Hence, the modified PR EOS is finalized as follows:

$$P = \frac{RT}{v-\beta b} - \frac{a\beta[1-1.7391\times(r_p/\sigma_{LJ})^{-1.379}]}{v(v+\beta b)+\beta b(v-\beta b)} \tag{3.18a}$$

$$\beta = \frac{1-\Delta T^*}{1-\Delta P^*} = \frac{1-1.7391\times(r_p/\sigma_{LJ})^{-1.379}}{1-1.1892\times(r_p/\sigma_{LJ})^{-0.807}} \tag{3.18b}$$

3.2 Results and Discussion

3.2.1 Variation of β and c

Covolume ratio β

Based on Equation (3.14), the correlation of the covolume ratio β can be obtained through the critical temperature and critical pressure shift data, as shown in Equation (3.18b). The variation of β with dimensionless pore size (r_p/σ_{LJ}=0.5-100) is demonstrated in Figure 3.3.

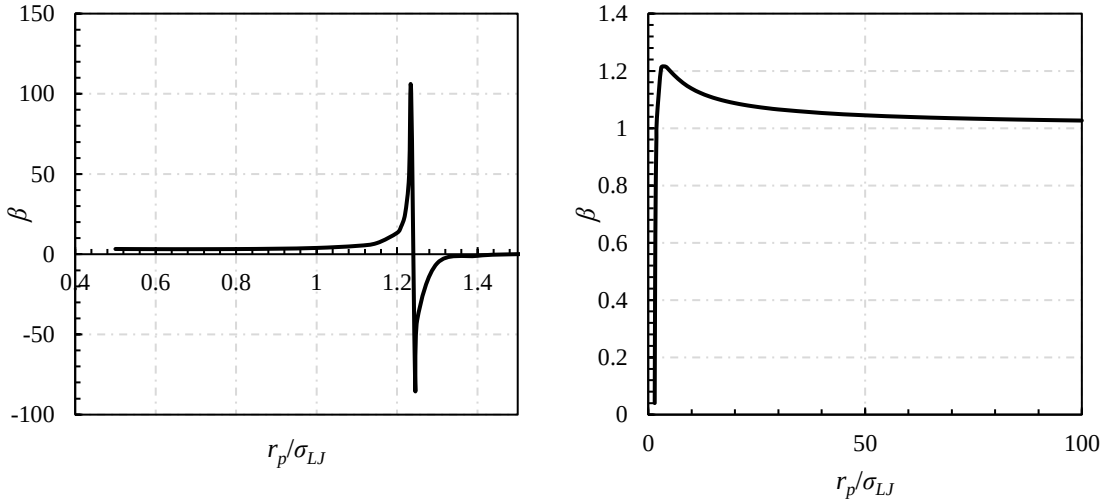

(a) r_p/σ_{LJ}=0.5-1.5 (b) r_p/σ_{LJ}=1.5-100

Figure 3.3: Variation of β with dimensionless pore size

As can be seen in Figure 3.3 (a), a drastic fluctuation of β appears at r_p/σ_{LJ} between 0.5-1.5, implying the inapplicability of Equation (3.18b) in this pore size range because of the severely lack of data and unclear physics. With r_p/σ_{LJ} varying from 1.5 to 100 in Figure 3.3 (b), β first increases and then decreases with the dimensionless pore size. It is resulted from the transition of the repulsive and attractive van der Waals forces between fluid molecules and pore walls under different geometric constraints. When the pore size is extremely small, the geometric constraints are significantly high, causing the molecule-wall interaction dominated by repulsive forces because of the closeness between the fluid molecules and the pore walls. These repulsive forces impose a decrease to the effective molecular volume, resulting in the β values to be smaller than unity. However, the molecule-wall interaction experiences a quick transition from the repulsion-dominated to attraction-dominated with the increase of the pore size. These attractive forces cause the effective molecular volume to increase, making the β value greater than unity. With the pore size continuously increasing, the geometric constraints and attractive forces become weaker, resulting in the decrease of the β value. It is worth noting that β being greater than unity represents that the confined covolume is generally larger than the bulk covolume at microporous media. Plus, the shift of the critical pressure is usually greater than the shift of critical temperature, based on Equation (3.14), which is in accordance with the collected data in Tables 3.1 and 3.2. At r_p/σ_{LJ} greater than 50, the β value is almost equal to unity, representing that the confined covolume b_c can be replaced by the bulk covolume b in pores of this size, i.e. the effect of geometric constraints can be neglected.

Molecule-wall interaction term c

With application of Equation (3.15) and the calculated results of covolume ratio β, the molecule-wall interaction term c can be calculated at different pore sizes and plotted in Figure 3.4.

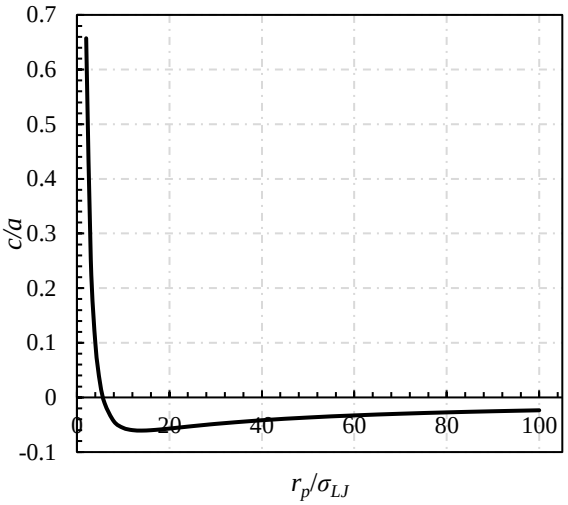

Figure 3.4: Variation of *c* with dimensionless pore size

Figure 3.4 demonstrates that the variation of the molecule-wall interaction term *c* with dimensionless pore size (r_p/σ_{LJ}) is consistent with the typical Lennard-Jones potential variation (Lennard-Jones, 1931). The value of *c/a* equals to 0 when r_p/σ_{LJ} is around 6, while at r_p/σ_{LJ}=14, the minimum value of *c*/*a* is obtained. As r_p/σ_{LJ} is less than 6, *c* is positive, representing that the molecule-wall interaction will decrease the overall pressure (see Equation 3.10) because the repulsive interaction between fluid molecules and the pore walls would decrease the possibility of collision. At r_p/σ_{LJ} greater than 6, the negative *c* value shows that molecule-wall interaction will increase the overall pressure, where the attractive interactions between fluid molecules and pore walls are dominant, increasing the possibility of collision. Figure 3.4 also demonstrates that the absolute value of *c*/*a* decreases with the increase of pore size after r_p/σ_{LJ}=14, representing that the effect of molecule-wall interaction can also be neglected after a specific dimensionless pore size, which is similar to that of the geometric constraints.

3.2.2 Model validation

The proposed EOS model is validated by the experimental data of both the critical temperature and critical pressure of different fluids.

Critical temperature

Table 3.1 lists the reported and the calculated confined critical temperature T_{cc} for both the data points included for proposing the critical temperature shift correlation and the data points excluded to validate the predictability of the proposed model. Both the reported and calculated T_{cc} are obviously lower than the bulk critical temperature T_c. The lower dimensionless pore size achieves lower T_{cc} value. Most of the relative derivation between the reported and the calculated T_{cc} values for the first 58 data points are less than 10%. The overall relative deviation is 6.48%, representing that the proposed correlation shown in Equation (3.16) is in good match with the collected data. As for the 5 predicted T_{cc} of 5 different fluids, the relative deviation is satisfactory, with an overall deviation of 8.40%, meaning that the proposed correlation is reliable enough to predict the critical temperature shift of different confined fluids at various pore sizes. However, the calculation errors tend to increase drastically at small dimensionless pore size (r_p/σ<5) due to the availability and accuracy of the critical shift data at that pore size range (Yang et al., 2019). As a result, the proposed EOS model generally warrants high validity from macropores down to pore size of 2 nm.

Critical pressure

The reported critical pressure shift and the calculated critical pressure shift for all the collected data points are listed in Table 3.2. The lower dimensionless pore size achieves higher ΔP^* value, which results in a lower critical pressure. Compared with critical temperature shift, the relative deviation between the reported and the calculated critical pressure shift data are much higher, with some values close to or higher than 100% (two data points). The overall relative

deviation for the 34 data points included for the correlation establishment is 27.84%, while that for the 6 excluded data points is 39.25%. The reasons for such high relative deviations are: (1) as can be seen in Figure 3.2 (b), the collected critical pressure shift data points are scattered and inconsistent in the literature, causing the fitted correlation less representative; (2) compared with critical temperature shift, the critical pressure shift is more sensitively affected by factors such as fluid types, pore geometry, and pore chemistry. Those factors plus topology (how different structures are connected) have all been proved to have obvious effect on confined fluid phase behavior (Singh and Singh, 2011, Lowry, M. Piri, 2018, Boelens et al., 2020). Hence, the improvement of the critical pressure shift measurement or more categorized correlation establishment based on different properties of both confined fluids and pores will further improve the accuracy of the proposed EOS model, resulting in a more accurate confined fluid phase behavior prediction.

3.2.3 Model application

Binary mixture CO_2+hydrocarbon

The proposed EOS is used to determine the phase diagrams of two binary mixtures of CO_2+*n*-C_4H_{10} and CO_2+*n*-$C_{10}H_{22}$ at various mole fractions of CO_2, as shown in Figure 3.5. Phase diagrams #1 through #4 represent the CO_2 molar composition of 10%, 30%, 50%, and 80%, respectively. Red lines stand for the mixture of CO_2+*n*-C_4H_{10}, while the black lines stand for CO_2+*n*-$C_{10}H_{22}$. Solid lines denote the bulk phase diagrams calculated by the PR EOS, while the dashed lines represent the phase diagrams at nanopores of 10 nm obtained by the proposed model. The critical points of each binary mixtures in both bulk and confined space are also demonstrated

(circle-bulk CO_2+*n*-C_4H_{10}, square-confined CO_2+*n*-C_4H_{10}, diamond-bulk CO_2+*n*-$C_{10}H_{22}$, triangle-confined CO_2+*n*-$C_{10}H_{22}$).

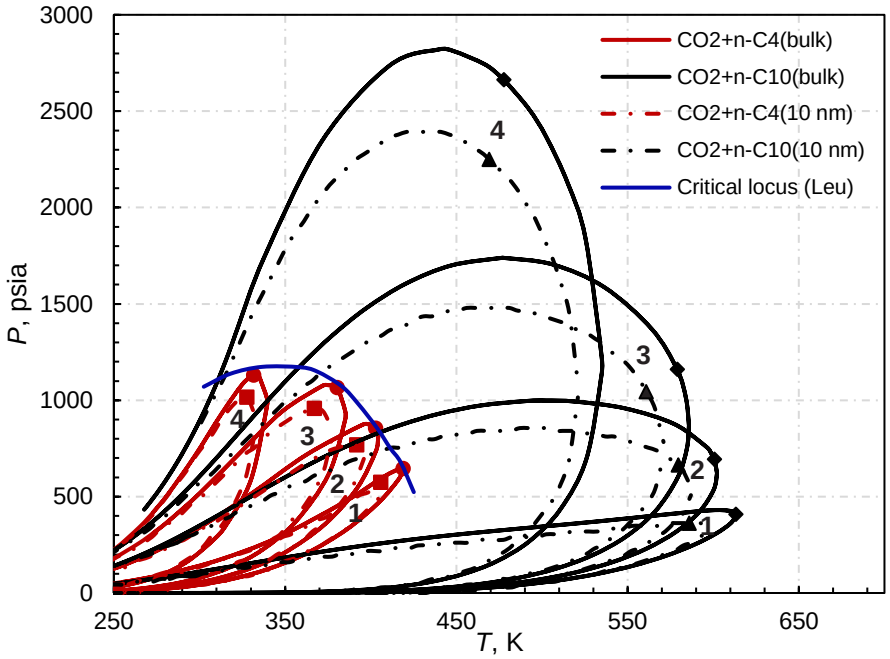

Figure 3.5: Phase diagrams of CO_2+*n*-C_4H_{10} (red) and CO_2+*n*-$C_{10}H_{22}$ (black) at different compositions (#1 through #4 represent the CO_2 molar composition of 10%, 30%, 50%, and 80%, respectively) in bulk (solid) and 10 nm confined (dashed) conditions. Solid blue line is the experimental CO_2+*n*-C_4H_{10} critical locus from Leu and Robinson (1987).

As demonstrated, the critical point of all the bulk CO_2+*n*-C_4H_{10} systems locate on the experimental critical locus obtained by Leu and Robinson (1987), representing the validity of the bulk calculation using PR EOS. Furthermore, the increasing CO_2 mole fraction results in the two-phase envelopes moving towards the top left side of Figure 3.5 (comparison of #1 through #4). And the confinement effect of nanopores causes the overall shrinkage of the two-phase envelopes and the shift of the critical points. As for the binary mixture of 50% CO_2+ 50% *n*-C_4H_{10} and 50% CO_2+ 50% *n*-$C_{10}H_{22}$ (#3 in Figure 3.5), the suppression rate of the critical temperature from bulk

to 10 nm are 2.43% and 2.79%, respectively; while the suppression rate of the critical pressure are 9.46% and 12.59%. The higher suppression rate of the CO_2+*n*-$C_{10}H_{22}$ mixture is caused by the larger molecule size of *n*-$C_{10}H_{22}$. Because larger molecule size is imposed of higher confinement effect at the same pore size, resulting in higher suppression rate.

Ternary mixture CO_2+n-C_4H_{10}+n-$C_{10}H_{22}$

Firstly, the binary interaction coefficients among different components are obtained by fitting the experimental pressure-composition diagram of CO_2+*n*-C_4H_{10}+*n*-$C_{10}H_{22}$ at 344.3 K (160 °F) in Nagarajan et al. (1990) using the original PR EOS, as shown in Figure 3.6. The newly proposed EOS is then applied to determine the phase diagram of a synthetic ternary mixture containing 75 mol% CO_2, 20 mol% *n*-C_4H_{10}, and 5 mol% *n*-$C_{10}H_{22}$, as demonstrated in Figure 3.7 (a) and (b).

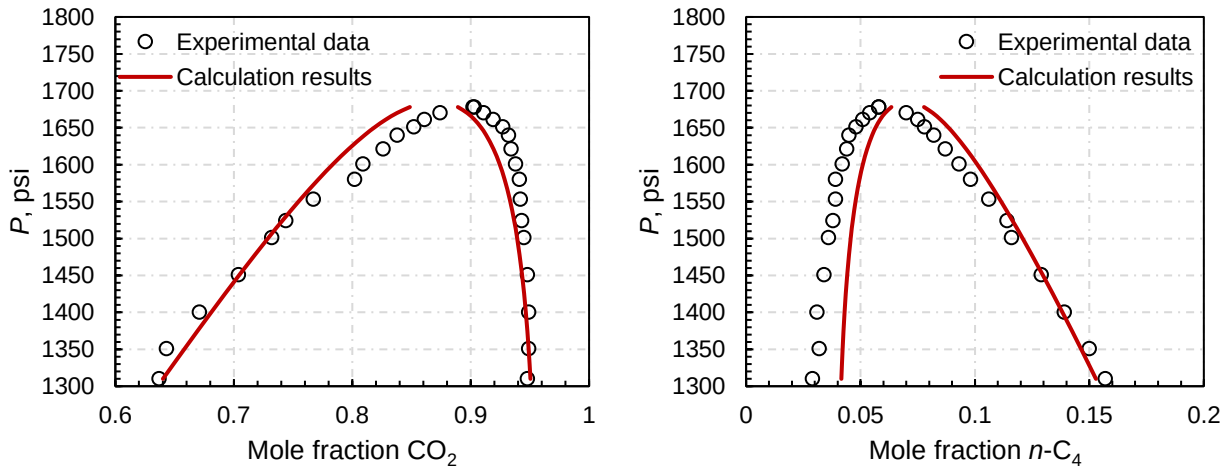

Figure 3.6: CO_2+*n*-C_4H_{10}+*n*-$C_{10}H_{22}$ pressure-composition diagram fitting with PR EOS at 344.3 K (160 °F)

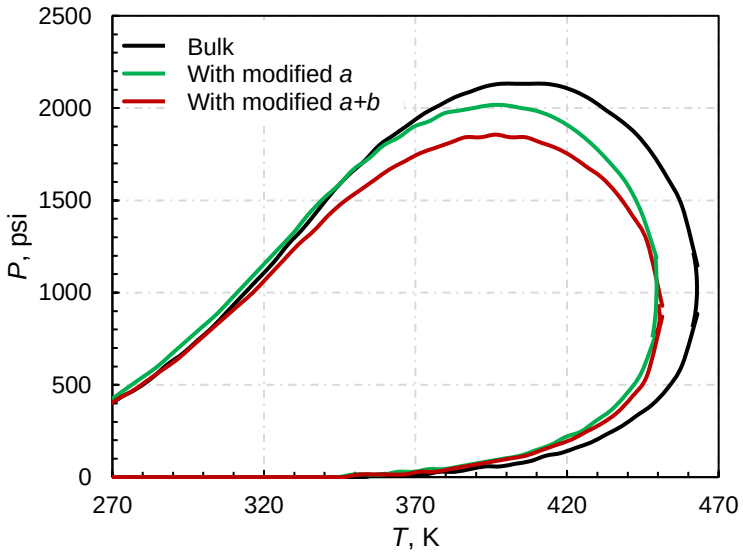

a) Phase diagram with different modifications

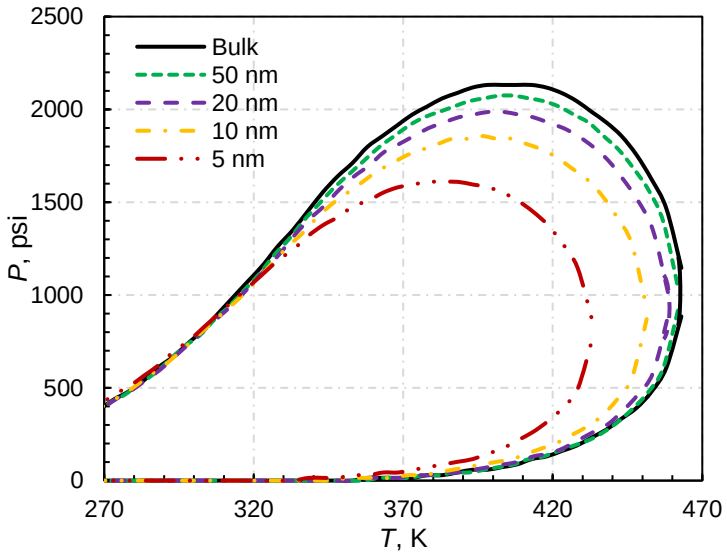

b) Phase diagram at various pore sizes using the modified EOS

Figure 3.7: Phase diagrams of ternary mixture CO_2+*n*-C_4H_{10}+*n*-$C_{10}H_{22}$

As demonstrated in Figure 3.7 (a), the modification of only *a* results in the shrinkage of the two-phase diagram. However, in the lower temperature region, the bubble-point pressure of the ternary mixture increases slightly, which is against the widely accepted results (Yang et al., 2019).

The result with modification of both *a* and *b* is more consistent with the well-accepted results with an overall shrinkage of the two-phase diagram. Figure 3.7 (b) shows the phase diagrams of the ternary mixture at various pore sizes. As can be seen, the smaller the pore size, the more shrinkage of the two-phase region because of the stronger confinement effect. Also, the phase diagram at 50 nm is almost the same with that of the bulk condition, representing that the confinement effect is not significant for pores of the size above mesopores (2-50 nm). This is in accordance with the results previously discussed for both the geometric constraints and molecule-wall interaction. Considering that the shale matrix is predominantly composed of micropores (less than 2 nm) and mesopores (2–50 nm) (Kuila and Prasad, 2013), it is of great significance to incorporate the nanoscale confinement into the development of shale hydrocarbon reservoirs.

In addition to the *P*-*T* diagrams, the ternary diagram of CO_2+*n*-C_4H_{10}+*n*-$C_{10}H_{22}$ at 1700 psi is also predicted by using the proposed EOS model (*T*=370 K, r_p=10nm), as demonstrated in Figure 3.8. The black line surrounds the two-phase region at bulk conditions, while the two-phase region of 10 nm pore is surrounded by the red line. The green dot represents the feed composition of 75 mol% CO_2, 20 mol% *n*-C_4H_{10}, and 5 mol% *n*-$C_{10}H_{22}$. As demonstrated in Figure 3.8, the size of the two-phase region decreases with consideration of the confinement effect. At 1700 psi, CO_2 is not miscible with the ternary mixture at the bulk condition but achieves the first contact miscibility at 10 nm. It demonstrates that the confinement effect is beneficial for achieving miscibility by suppressing the two-phase region with respect to the synthetic ternary mixture. As for the actual reservoir fluids, further investigation needs to be conducted.

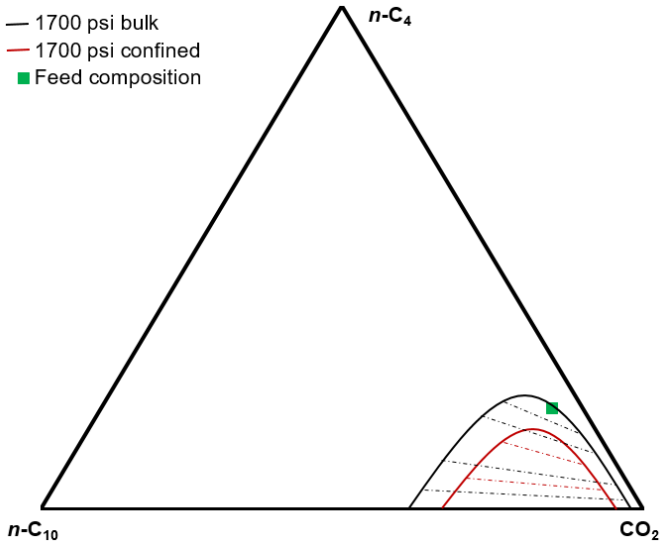

Figure 3.8: Ternary diagrams of CO_2+*n*-C_4H_{10}+*n*-$C_{10}H_{22}$ confined in a 10 nm pore at 370 K

Reservoir fluid

To investigate the potential of huff and puff EOR to increase the condensate production in tight reservoirs, Sheng et al. (2016) conducted a simulation study of gas condensate recovery in Eagle Ford gas condensate reservoir. The initial reservoir pressure is 9985 psi and the reservoir temperature is 270 °F. Tables 3.3 and 3.4 list the parameters of the condensate components and their binary interaction parameters, accordingly.

Table 3.3: Composition of the Eagle Ford condensate (Sheng et al., 2016)

Component	Molar fraction	*Pc* (kPa)	*Tc* (K)	Molecular weight, (g/mole)	Acentric factor	Parachor coefficient
CO_2	0.0188	7376.46	304.2	0.225	44.01	78
N_2	0.0036	3394.39	126.2	0.04	28.01	41
CH_4	0.5695	4600.16	190.6	0.008	16.04	77
C_2H_6	0.1431	4883.87	305.4	0.098	30.07	108
C_3H_8	0.0637	4245.52	369.8	0.154	44.1	150.3
IC_4	0.0145	3647.70	408.1	0.176	58.12	181.5
NC_4	0.0244	3799.69	425.2	0.193	58.12	189.9
IC_5	0.0143	3384.26	460.4	0.227	72.15	225
NC_5	0.011	3374.12	469.6	0.251	72.15	231.5
FC_6	0.0177	2631.41	483.1	0.33	86	250.11
FC_7	0.1194	3765.24	651.8	0.36996	168	278.41

Table 3.4: Binary interaction parameters of Eagle Ford condensate (Sheng et al., 2016)

Comp	CO_2	N_2	CH_4	C_2H_6	C_3H_8	IC_4	NC_4	IC_5	NC_5	FC_6	FC_7
CO_2	0	0	0.105	0.13	0.125	0.12	0.115	0.115	0.115	0.115	0.115
N_2	0	0	0.025	0.01	0.09	0.095	0.095	0.1	0.11	0.11	0.11
CH_4	0.105	0.025	0	0.00269	0.00854	0.0157	0.0147	0.0209	0.0206	0.0253	0.0296
C_2H_6	0.13	0.01	0.00269	0	0.00166	0.00549	0.00491	0.00873	0.00858	0.0117	0.0147
C_3H_8	0.125	0.09	0.00854	0.00166	0	0.00112	0.000866	0.0028	0.00271	0.00462	0.00657
IC_4	0.12	0.095	0.0157	0.00549	0.00112	0	1.59E-05	0.00038	0.00035	0.0012	0.00229
NC_4	0.115	0.095	0.0147	0.00491	0.00087	1.6E-05	0	0.00055	0.000515	0.00149	0.00268
IC_5	0.115	0.1	0.0209	0.00873	0.0028	0.00038	0.000554	0	7.17E-07	0.00023	0.0008
NC_5	0.115	0.11	0.0206	0.00858	0.00271	0.00035	0.000515	7.2E-07	0	0.00026	0.00085
FC_6	0.115	0.11	0.0253	0.0117	0.00462	0.0012	0.00149	0.00023	0.000255	0	0
FC_7	0.115	0.11	0.0296	0.0147	0.00657	0.00229	0.00268	0.0008	0.000849	0	0

Figure 3.9 presents the calculated phase diagrams of the Eagle Ford condensate at different pore sizes (5-50 nm) by using the proposed EOS. The phase diagram at bulk conditions is calculated by the original PR EOS. The black dashed line represents the reservoir temperature (405 K).

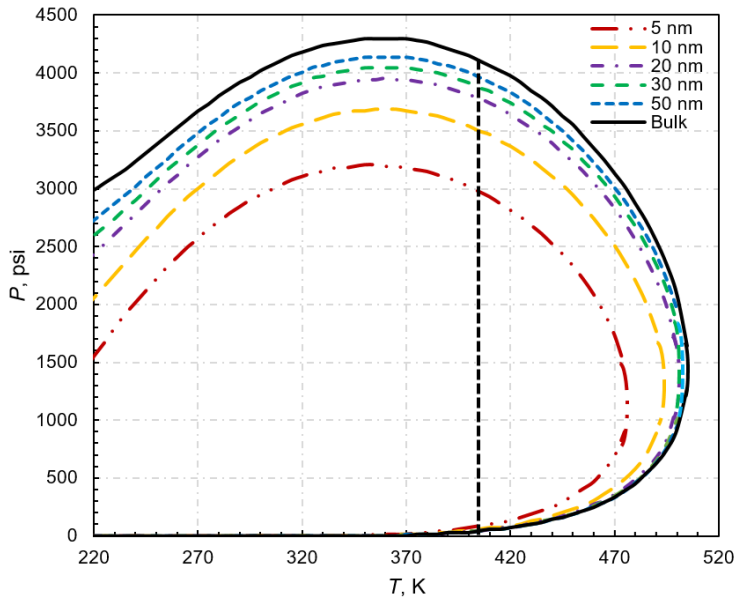

Figure 3.9: Phase diagrams of Eagle Ford condensate at various pore sizes

As can be seen, in accordance with the case of synthetic ternary mixture CO_2+*n*-C_4H_{10}+*n*-$C_{10}H_{22}$, confinement effect also results in the overall shrinkage of the phase diagrams of Eagle Ford condensate. With a decrease in pore size, more shrinkage of the phase diagrams is

demonstrated. Figure 3.10 shows the upper dew-point pressure of Eagle Ford sample at reservoir temperature varying with pore size. At 5 nm, the upper dew-point pressure is 2972.6 psi, demonstrating a suppression of 27.56% (compared with the bulk value of 4103.6 psi), while the suppression of 20 nm (3784.6 psi) is 7.77%. The upper dew-point pressure suppression of 50 nm (3958.6 psi) is 3.53%, which is relatively low. Thus, the original PR EOS is applicable to describe the phase behavior of fluids confined in pores of size above 50 nm, which is in accordance with the value for the synthetic ternary mixture.

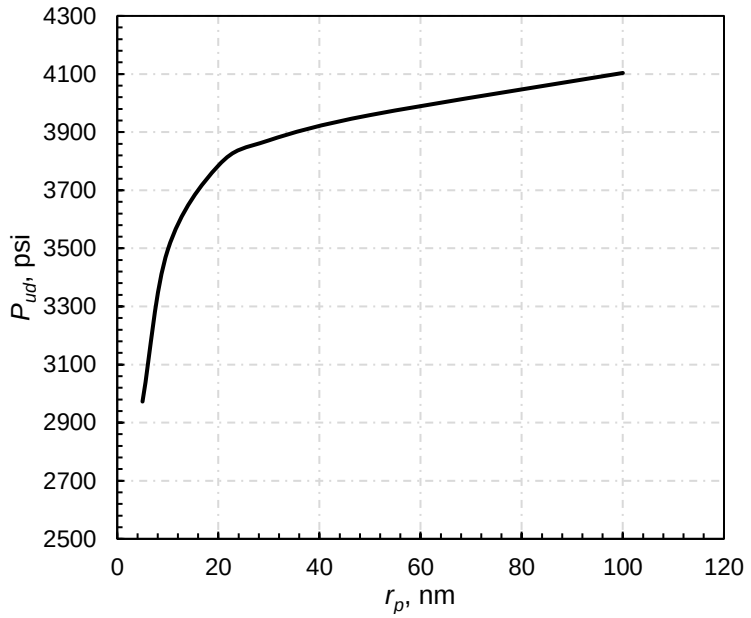

Figure 3.10: Upper dew-point pressure at reservoir temperature with pore size

Ternary diagram with pseudo-components

To investigate the miscible behavior of injection gas and the Eagle Ford condensate, ternary diagram with three pseudo-components under both bulk and confined conditions are calculated and demonstrated in Figure 3.11. The rule of grouping the pseudo-components is: a volatile pseudo-component composed of nitrogen and methane, plus CO_2, an intermediate pseudo-component of ethane through hexane, and a relatively nonvolatile pseudo-component composed

of C_{7+} (Stalkup, 1984). As can been seen, with consideration of the confinement effect, the size of the two-phase region decreases, which is in accordance with the results observed in the *P-T* diagrams. At 4100 psi, with bulk conditions, gas injection (volatile gases) is not able to achieve a first contact miscibility with the Eagle Ford condensate sample (represented by the green dot). With consideration of the confinement effect at 10 nm, gas injection can achieve a first contact miscibility with the condensate sample, which will obviously benefit the condensate recovery. This demonstrates that confinement effect is in favor of the miscible gas injection EOR by increasing the possibility of achieving first contact miscibility.

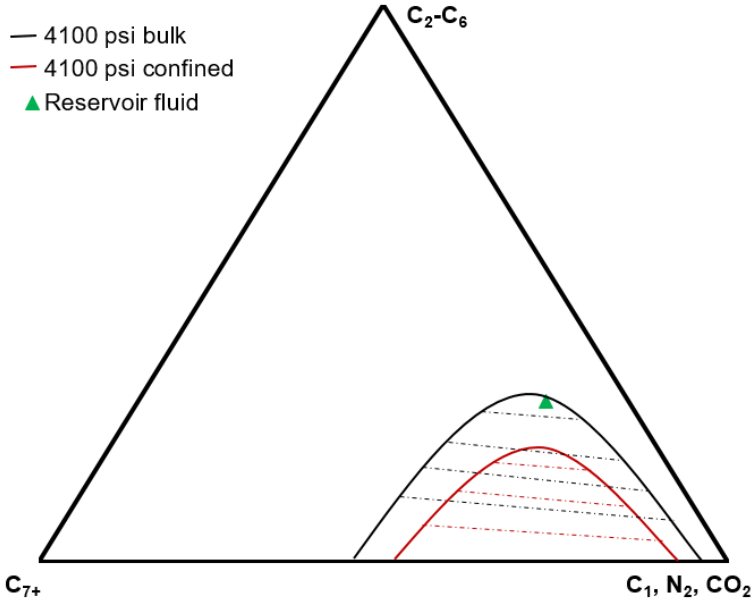

Figure 3.11: Ternary diagram of Eagle Ford condensate at reservoir temperature of 405 K

3.3 Summary

A modified PR EOS with consideration of the confinement effect on both attractive parameter *a* and covolume *b* is proposed to represent the molecule-wall interaction and geometric constraints. The proposed model is validated to be able to predict the confined fluid phase behavior at various pore sizes. Analyses show that the modification of parameters *a* and *b* cooperatively

impose the overall shrinkage to the two-phase envelope of confined CO_2/hydrocarbon systems. Moreover, molecule-wall interaction can demonstrate as repulsion- or attraction-dominant under different pore sizes, having a similar variation trend with the typical Lennard-Jones potential. With consideration of the geometric constraints, confined covolume is generally greater than the bulk covolume and the variation with dimensionless pore size is not monotonic. Confinement effect imposes an overall shrinkage to both the *P*-*T* diagram and the two-phase region in a ternary diagram of CO_2/hydrocarbon systems, benefiting the miscible EOR in shale reservoirs by increasing the possibility of achieving the first contact miscibility.

Chapter 4: Modified Kelvin Equation for Capillary Condensation Pressure

Phase behavior of confined fluids deviates significantly from that of bulk fluids. However, the effect of nanoscale confinement on the capillary condensation within nanopores has not been well understood. In this chapter, the classic Kelvin equation is modified by incorporating the real gas effect, along with the pore size effect on surface tension, the multilayer adsorption, and the molecule-wall interaction potential to improve its accuracy in calculating the capillary condensation pressure. The modified Kelvin equation is further extended for multicomponent fluids in nanopores. More specifically, the modified Peng-Robinson equation of state (PR EOS) is applied to describe the real gas effect. The pore size effect on surface tension is reflected by accounting for the meniscus variation with pore size. The multilayer adsorption of both single- and multicomponent fluids are computed by the Brunauer–Emmett–Teller (BET) model and the Frenkel-Halsey-Hill equation is used to calculate the molecule-wall interaction potential.

4.1 Modeling Methodology

Figure 4.1 demonstrates a schematic diagram of the capillary condensation dynamics for a single-component fluid in a nanopore. As the fluid is confined in a nanopore, the fluid molecules absorb onto the pore walls with increasing pressure from P_1 to P_4. After completion of the monolayer adsorption at P_2, multilayer adsorption commences at P_3 (Thommes 2004). The capillary condensation happens through liquid bridges between pore walls when the adsorbate

reaches to a critical film thickness (see P_4) (Monson 2012). Such a phenomenon occurs at a pressure lower than the bulk saturation pressure, which is the capillary condensation pressure.

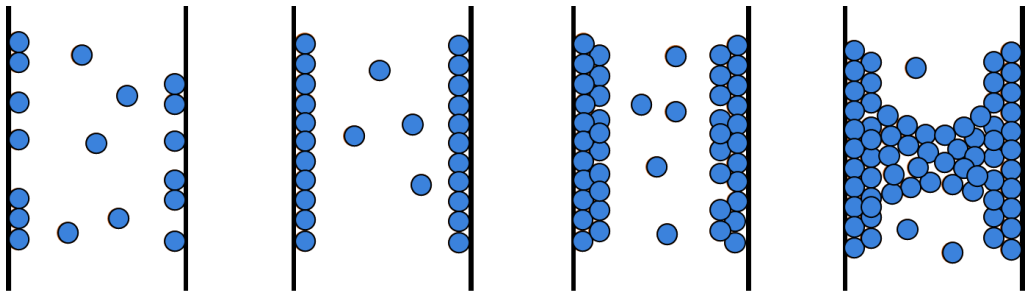

Figure 4.1: Schematic diagram of the capillary condensation dynamics for a single-component fluid with increasing pressure. Thick black lines stand for pore walls and filled circles represent molecules. Schematic diagram refers to Thommes (2004) and Monson (2012)

The capillary condensation pressure is usually obtained by isotherm adsorption experiments in nanomaterials, taking the midpoint of the step change in the adsorption isotherm branch (Horikawa et al., 2011; Morishige and Nakamura, 2004), as shown in Figure 4.2.

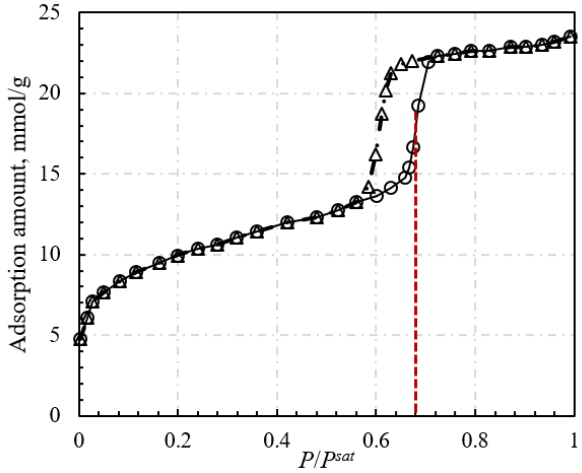

Figure 4.2: Determination of the capillary condensation pressure. Isotherm adsorption/desorption data of N_2 in SBA-15 material; solid black line is the adsorption branch and dashed black line is the desorption branch; red dashed line points to the ratio of the capillary condensation pressure and the bulk saturation pressure, which is 0.68. Data from Ravikovitch and Neimark (2001)

The original Kelvin equation describes the pressure difference between the confined and the bulk phases in terms of capillary pressure (Thomson, 1872). It is used extensively in both experiments and models to mathematically describe the capillary condensation phenomenon. As shown in Equation (4.1), the Kelvin equation gives a relation between the pore size and the capillary condensation pressure:

$$RT \ln \frac{P^{con}}{P^{sat}} = -\frac{2\gamma_{\infty} v^{L}}{r_p} \tag{4.1}$$

where R is the universal gas constant, T is the absolute temperature, P^{con} is the capillary condensation pressure which is the saturation pressure for the fluid confined in capillary, P^{sat} is the saturation pressure of the bulk fluid, γ_{∞} is the surface tension between the vapor and liquid phase at bulk condition, v^{L} is the molar volume of the liquid phase, and r_p is the pore radius.

Assumptions used to derive the Kelvin equation include: (a) the gas was assumed to be an ideal fluid; (b) the surface tension was assumed to be constant; (c) the gas adsorption was neglected; and (d) the adsorbate potential change under the effect of confinement was neglected. However, such assumptions are invalid when the pore size is reduced to nanoscale. Drastic errors may occur when the original Kelvin equation is used to directly calculate the capillary condensation pressure in nanopores due to these incompatible assumptions. Therefore, it is necessary to modify the Kelvin equation with respect to these incompatible assumptions to make it applicable for the fluids confined in nanopores. In this work, the real gas effect, the pore size effect on surface tension, the multilayer adsorption, and the molecule-wall interaction potential have been incorporated into the Kelvin equation. The methodology of such modifications is elaborated below.

4.1.1 Modified kelvin equation for single-component fluids

Real gas effect

Considering a vapor-liquid system by assuming that the liquid phase completely wets the solid surface, i.e., the contact angle θ is zero, the mechanical and chemical equilibrium equations can be written as:

$$\mu^V = \mu^L \tag{4.2}$$

$$P^V - P^L = 2\gamma_\infty / r_p \tag{4.3}$$

where μ^V and μ^L are the chemical potentials of the vapor and liquid phases, respectively; P^V and P^L are the pressures of the vapor and liquid phases, respectively.

Passing from one equilibrium state to another at a constant temperature yields:

$$d\mu^V = d\mu^L \tag{4.4}$$

$$dP^V - dP^L = d(2\gamma_\infty / r_p) \tag{4.5}$$

Under isothermal conditions, the Gibbs-Duhem equation for each phase can be written as:

$$-v^V dP^V + d\mu^V = 0 \tag{4.6}$$

$$-v^L dP^L + d\mu^L = 0 \tag{4.7}$$

where v^V is the molar volume of the vapor phase.

Combing Equations (4.4)-(4.7) leads to

$$\frac{v^L - v^V}{v^L} dP^V = d(\frac{2\gamma_\infty}{r_p}) \tag{4.8}$$

It is assumed that the molar volume of the liquid phase is much smaller than that of the vapor phase ($v^V >> v^L$):

$$-v^V dP^V = 2v^L d(\frac{\gamma_\infty}{r_p}) \tag{4.9}$$

Instead of further assuming that the vapor phase can be described by the ideal gas law, the real gas effect is considered in this work,

$$P^V v^V = ZRT \tag{4.10}$$

where Z is the compressibility factor of the vapor phase and is calculated by the modified PR EOS.

Combing Equations (4.9) and (4.10) obtains:

$$-\frac{ZRT}{P^V} dP^V = 2v^L d(\frac{\gamma_\infty}{r_p}) \tag{4.11}$$

Integrating equation (4.11) from $r=\infty$ to any r, the pressure changes from the saturation pressure of bulk fluid P^{sat} to P^{con} at r_p:

$$-RT\int_{P^{sat}}^{P^{con}} \frac{Z}{P^V} dP^V = 2\int_\infty^r v^L d(\frac{\gamma_\infty}{r_p}) \tag{4.12}$$

Based on the Standing-Katz Z-factor chart (Standing and Katz, 1942), it is reasonable to assume a linear correlation between the compressibility factor and pressure at a low-pressure range, i.e., between 0 and P^{sat}.

$$Z = 1.0 - \alpha P^V \tag{4.13}$$

Here, α is determined by establishing the correlation between the gas compressibility factor and pressure up to the bulk saturation pressure at constant temperature.

Combing Equations (4.12) and (4.13) yields:

$$RT \ln \frac{P^{con}}{P^{sat}} + \alpha RTP^{sat}(1-\frac{P^{con}}{P^{sat}}) = -\frac{2\gamma_\infty v^L}{r_p} \tag{4.14}$$

Pore size effect on surface tension

As aforementioned, errors could be introduced if the surface tension variation in confined space is not considered (Takei et al., 1997; Wongkoblap et al., 2011). The pore size effect on surface tension is considered by the following equation (Tan and Piri, 2015):

$$\gamma = \frac{\gamma_\infty}{1-\lambda / r_m} \tag{4.15}$$

where γ is the surface tension at the confined space, r_m is the mean radius of the meniscus (r_m=2r_p for cylindrical meniscus). The λ value is estimated to be equal to $\sigma_{LJ}\sqrt{2/3}$ for a hexagonal close-paced structure (Sonwane and Bhatia, 1998). By replacing γ_∞ in Equation (4.11) with Equation (4.15), Equation (4.14) further becomes:

$$RT\ln\frac{P^{con}}{P^{sat}}+\alpha RTP^{sat}(1-\frac{P^{con}}{P^{sat}})=-\frac{2\gamma_\infty v^L}{r_p-\lambda/2} \tag{4.16}$$

Multilayer adsorption

Based on the capillary condensation dynamics, capillary condensation occurs essentially in the core of the pore after adsorption reaching to a critical film thickness (see Figure 4.1). Thus, the formation of the adsorbed film greatly affects the dynamics of capillary condensation (Thommes, 2004). To account for the multilayer adsorption, the BET model (Brunauer et al., 1938) is used in this work.

$$V_a=V_m\frac{Cx_p}{(1-x_p)\left[1+(C-1)x_p\right]} \tag{4.17}$$

where V_a is the adsorption amount of the adsorbate, x_p=P/P^{sat}, V_m is the amount of adsorbate covering the surface area of the adsorbent in a monomolecular coverage, which is known as the monolayer capacity, C is the constant connected with the difference between the enthalpy of the first layer and the enthalpy of condensation. The thickness of the multilayer adsorption can be calculated by Equation (4.18) (Dong et al., 2016).

$$\frac{t}{t_m}=\frac{V_a}{V_m} \tag{4.18}$$

where t is the thickness of the multilayer adsorption, $t_m=(v^L/N_A)^{1/3}\approx\sigma_{LJ}$, N_A is the Avogadro number. After computing the multilayer adsorption thickness by the BET model, the thickness can be coupled into Equation (4.18) to account for the effect of adsorption:

$$RT\ln\frac{P^{con}}{P^{sat}}+\alpha RTP^{sat}(1-\frac{P^{con}}{P^{sat}})=-\frac{2\gamma_{\infty}v^{L}}{r_p-t-\lambda/2} \tag{4.19}$$

It is worth noting that the constants, V_m and C, in BET model need to be obtained first before calculating the multilayer adsorption thickness. A simple conversion of Equation (4.17) will demonstrate a linear relationship between $x_p/V_a(1\text{-}x_p)$ and x_p. The BET constants can be determined from the slope of the linear relationship and the intersection point with the vertical axis. In addition, because of the exothermic feature of the adsorption process, the adsorption amount decreases with increasing temperature. Thus, the BET constants also change with temperature, and the correlations can be established by computing BET constants at different temperatures.

Molecule-wall interaction potential

It is widely accepted that the strong confinement effect caused by molecule-wall interaction is the reason for the dramatic phase behavior deviation of confined fluids, which should also have significant influence on the capillary condensation in nanopores. Gregg and Sing (1982) claimed that proximity of the solid surface, along with the capillarity effect (original Kelvin equation), are the two main reasons responsible for the reduction of adsorbate chemical potential, which results in capillary condensation. In this work, the molecule-wall interaction potential is introduced to represent the proximity effect of the solid surface in the form of the Frenkel-Halsey-Hill equation (Shkolnikov et al., 2011):

$$F(t)=\frac{K}{t^{m}} \tag{4.20}$$

where *F(t)* is the adsorbate potential change under the proximity effect of solid surface, i.e. molecule-wall interaction. *K* and *m*, which can be determined by regression of the collected P^{con}/P^{sat} data of single-component fluids with the adsorption thickness (*t*), are constants to calculate the molecule-wall interaction potential. With consideration of the molecule-wall

interaction potential and the approach of incorporating it by Broekhoff and De Boer (1967), Equation (4.21) is obtained:

$$RT \ln \frac{P^{con}}{P^{sat}} + \alpha RTP^{sat}(1 - \frac{P^{con}}{P^{sat}}) = -\frac{2\gamma_{\infty} v^{L}}{r_p - t - \lambda/2} - \frac{K}{t^m} \tag{4.21}$$

Equation (4.21) is the modified Kelvin equation with consideration of the real gas effect, the pore size effect on surface tension, the multilayer adsorption, and the molecule-wall interaction potential. This modified equation is for the calculation of single-component fluids. However, with consideration of the real cases, calculation of multicomponent fluids is of higher necessity, which requires an extension of the modified Kelvin equation for multicomponent fluids.

4.1.2 Extended kelvin equation for multicomponent fluids

As aforementioned, it is more practical to apply the simple Kelvin equation to multicomponent fluids due to its wider applications in multi-disciplinary. However, less effort has been reported to extend the Kelvin equation for mixtures. A major difference between pure component and mixture is that the vapor pressure is split into a bubble-point pressure and a dew-point pressure when the fluid contains more than one component. Since the capillary condensation phenomenon of multicomponent fluids is essentially a process of liquid dropout, the capillary condensation pressure is closer to the dew-point pressure of bulk fluid (Shapiro and Stenby, 1997). Therefore, the modified Kelvin equation is extended in the neighborhood of bulk dew-point pressure with respect to aforementioned four factors. Liquid dropout happens at the dew-point pressure if it is in bulk condition and capillary condensation happens at a pressure lower than the bulk dew-point pressure.

Real gas effect

Considering a vapor-liquid system with multicomponents, assuming that the liquid phase completely wets the solid surface, the mechanical and chemical equilibrium equations, the Gibus-Duhem equations for each component are the same with that of single-component fluid.

$$d\mu_i^V = d\mu_i^L \tag{4.22}$$

$$-v^V dP^V + \sum_{i=1}^{c} y_i d\mu_i^V = 0 \tag{4.23}$$

$$-v^L dP^L + \sum_{i=1}^{c} x_i d\mu_i^L = 0 \tag{4.24}$$

In the neighborhood of the dew point, Equation (4.23) can be expressed as:

$$d\mu_i^V = v_i^V dP^V \tag{4.25}$$

Combing Equations (4.22), (4.24), and (4.25), along with the Young–Laplace equation yields:

$$-v^L \left[dP^V - d(2\gamma_\infty / r_p) \right] + \sum_{i=1}^{c} x_i v_i^V dP^V = 0 \tag{4.26}$$

For each of the component in the multicomponent fluid, $v_i^V >> v_i^L$, Equation (4.26) can be written as:

$$-\sum_{i=1}^{c} x_i v_i^V dP^V = v^L d(2\gamma_\infty / r_p) \tag{4.27}$$

By considering the term $v^V dP^V = \sum_{i=1}^{c} y_i v_i^V dP^V$, it yields:

$$-\sum_{i=1}^{c} (x_i - y_i) v_i^V dP^V - v^V dP^V = v^L d(2\gamma_\infty / r_p) \tag{4.28}$$

The pressure at r is the capillary condensation pressure P^{con}, while the pressure at $r=\infty$ is the bulk dew-point pressure P_d of the multicomponent fluid.

$$-\int_{P_d}^{P^{con}} \sum_{i=1}^{c} (x_i - y_i) v_i^V dP^V - \int_{P_d}^{P^{con}} v^V dP^V = \int_{\infty}^{r} v^L d(2\gamma_\infty / r_p) \tag{4.29}$$

Since P^{con} is close to the bulk dew-point pressure, according to Shapiro and Stenby (1997), in the neighborhood of dew-point pressure, the second order terms of the pressure difference P_d-P^{con} can be omitted. Based on this assumption, the first term on the left side of Equation (4.29) which represents the contribution of the compositional shift can be neglected. It means that the effect of compositional shift on capillary condensation pressure is insignificant in the neighborhood of dew point.

$$-\int_{P_d}^{P_{con}} v^V dP^V = \int_{\infty}^{r} v^L d(2\gamma_\infty / r_p) \tag{4.30}$$

As can be seen, Equation (4.30) is almost the same with the integration of Equation (4.12). Hence, the extended Kelvin equation with consideration of the real gas effect is basically the same with that of the single-component fluid as Equation (4.14), except that P^{sat} should be replaced by P_d, as shown in Equation (4.31).

$$RT \ln \frac{P^{con}}{P_d} + \alpha RTP_d (1 - \frac{P^{con}}{P_d}) = -\frac{2\gamma_\infty v^L}{r_p} \tag{4.31}$$

It is worth noting that the compressibility factor of the multicomponent fluid is also calculated with the modified PR EOS (Yang et al., 2019). And the linear correlation between the compressibility factor and pressure is still applied here.

Surface tension calculation

As for the single-component fluid, its surface tension can be easily obtained from literature. While for the multicomponent fluid, the surface tensions are difficult to obtain. It can be either measured by experiments or computed by theoretical models. In this work, a theoretical algorithm

is applied based on the model proposed by Danesh et al. (1991) to calculate the surface tension of a multicomponent fluid. Figure 4.3 demonstrates the flow chart of the algorithm used in this work.

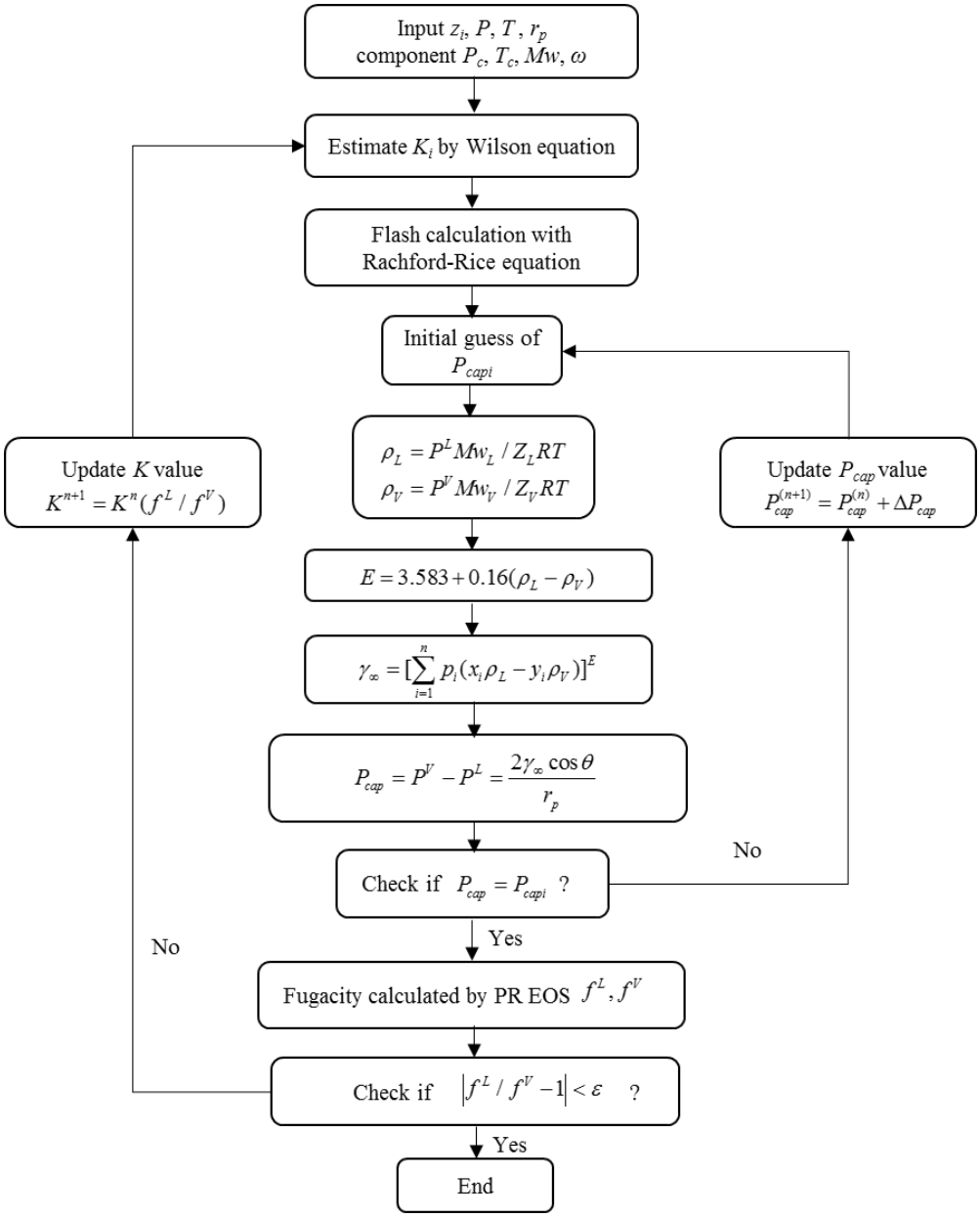

Figure 4.3: Flow chart of surface tension calculation for multicomponent fluid

The procedures are as follows:

1) Input the feed composition, temperature, pore size and the properties of each component.

2) Use the Wilson equation to estimate the initial *K* values.

$$K_i^1 = \frac{\exp[5.37(1+\omega_i)(1-T_{ri}^{-1})]}{P_{ri}} \tag{4.32}$$

where T_{ri} and P_{ri} are the reduced temperature and pressure of the *i*th component, respectively.

3) Flash calculation with the Rachford-Rice equation.

$$\sum(x_i - y_i) = \frac{z_i(K_i - 1)}{F_v(K_i - 1) + 1} = 0 \tag{4.33}$$

where z_i is the feed composition; F_v is the mole fraction of the vapor phase in the overall mixture.

4) With the initial guess of a small value of the capillary pressure, calculate the confined fluid capillary pressure iteratively.

5) Compute the fugacities of liquid and vapor phase by using the original PR EOS.

6) The convergence is checked to make sure it is within the tolerance. If not, the *K* value needs to be updated and repeated from step #2. The superscripts (*n*) and (*n*+1) represent the iteration level.

7) Output the surface tension value γ_∞.

This algorithm is used to calculate the surface tension of a multicomponent fluid at bulk conditions, the pore size effect on surface tension will still be considered with Equation (4.15). By considering the pore size effect on surface tension, Equation (4.34) can be obtained:

$$RT\ln\frac{P^{con}}{P_d} + \alpha RTP^{sat}(1 - \frac{P^{con}}{P_d}) = -\frac{2\gamma_\infty v^L}{r_p - \lambda/2} \tag{4.34}$$

Multilayer adsorption

Capillary condensation of a multicomponent fluid also happens when the multilayer adsorption reaches to a critical thickness. It is assumed that the adsorption of each component can be described by the BET model and the total adsorption thickness equals to the sum of the

adsorption thickness of each component. The adsorbed amount of each component (V_{ai}) at a given temperature is:

$$V_{ai} = V_m^i \frac{C^i x_p}{(1-x_p)\left[1+(C^i-1)x_p\right]} \tag{4.35}$$

where $x_p = \frac{P^i}{P^{sat}}$ and $P^i = y_i P$, V_m^i is the monolayer capacity of the *i*th component and C^i is the enthalpy related constant for the *i*th component. For the same adsorbate and the same adsorbent, with an increase in temperature, both parameters of V_m and C in the BET equation are reduced.

The multilayer adsorption thickness of each component is calculated by:

$$\frac{t_i}{t_{mi}} = \frac{V_{ai}}{V_{mi}} \tag{4.36}$$

$$t = \sum_{i=1}^{n} t_i \tag{4.37}$$

Equation (4.37) provides the multilayer adsorption thickness of multicomponent fluid confined in nanopores (Dong et al., 2016) The incorporation of the adsorption thickness yields Equation (4.38):

$$RT \ln \frac{P^{con}}{P_d} + \alpha RTP^{sat}\left(1-\frac{P^{con}}{P_d}\right) = -\frac{2\gamma_\infty v^L}{r_p - t - \lambda/2} \tag{4.38}$$

Molecule-wall interaction potential

In this work, it is assumed that the molecule-wall interaction potential of each component can be described by the Frenkel-Halsey-Hill equation (Shkolnikov et al., 2011) and the potential of each component ε_i is proportional to the total potential ε of the multicomponent fluid (Shapiro and Stenby, 1998):

$$F_i(t_i) = \frac{K_i}{t_i^{m_i}} \tag{4.39}$$

$$\varepsilon_i(t_i) = \eta_i \varepsilon(t) \tag{4.40}$$

where K_i and m_i are the constants of the ith component to calculate the molecule-wall interaction potential, t_i is the adsorption thickness of the ith component, and η_i is the potential fraction of the ith component over the total potential of the multicomponent fluid. Here, K_i and m_i values of each component are different because of the property difference. These two constants will be obtained by regression of the capillary condensation pressure data of each single component.

This leads to the extended Kelvin equation for multicomponent fluid with consideration of the real gas effect, the pore size effect on surface tension, the multilayer adsorption, and the molecule-wall interaction potential which is demonstrated in Equations (4.41).

$$RT \ln \frac{P^{con}}{P_d} + \alpha RTP_d \left(1 - \frac{P^{con}}{P_d}\right) = -\frac{2\gamma_\infty v^L}{r_p - t - \lambda/2} - \sum_{i=1}^{c} \frac{K_i}{(t_i)^{m_i}} \tag{4.41}$$

The extended Kelvin equation, i.e., Equations (4.41) can be degraded into the modified Kelvin equation of the single-component fluid as shown in Equations (4.21) when i=1.

As aforementioned, Shapiro and Stenby (1997) also proposed a modified Kelvin equation for non-ideal multicomponent fluid, as shown in Equation (4.42).

$$\frac{P_{cap}}{P_d} = \frac{v^{VL}}{v^L} Z_{av} \ln \frac{P^{con}}{P_d} - \frac{P^{con}}{P_d} + 1 \tag{4.42}$$

where, $v^{VL} = \sum_{i=1}^{c} x_i v_i^V$, Z_{av} is the logarithmic mean of the compressibility factor ratio, $Z(P)/Z(P_d)$, and with a linear assumption, $Z_{av} = 1 - \frac{\alpha}{2}\left(\frac{P}{P_d} - 1\right)$. The calculation results of Equations (4.41) and (4.42) will be compared later to demonstrate the validation of the proposed model in this work.

4.2 Model Validation

This section demonstrates the validation of the modified Kelvin equation for four single-component fluids (N_2, Ar, CO_2, and n-C_5H_{12}) and a binary mixture (CO_2+n-C_5H_{12}) by using collected experimental data. Table 4.1 lists 42 measured P^{con}/P^{sat} data points of N_2, Ar, CO_2, n-C_5H_{12}, and CO_2+n-C_5H_{12} mixture together with the temperature T and pore size r_p. The first four groups of pure N_2, Ar, CO_2, and n-C_5H_{12} data (31 data points in total) are included in the parameter determination process of the model. The last three groups of pure N_2, Ar, and CO_2+n-C_5H_{12} mixture data (11 data points in total) are excluded to determine the parameters in the models and used to demonstrate the predictability of the model. The following parameters in the models of Equations (4.21) and (4.41) are determined by using the first 31 data points: the compressibility factor variation constant α, the surface tension γ_∞ (only for multicomponent fluids), the multilayer adsorption thickness t, and the molecule-wall interaction potential constants K and m.

Table 4.1: Database of this work and the model validation of different fluids

Reference	Fluid	T (K)	r_p (nm)	α	γ_∞ (mN/m)	t (nm)	K	m	P^{con}/P^{sat} (measured)	P^{con}/P^{sat} (calculated this work)	Relative deviation this work (%)	P^{con}/P^{sat} (calculated other work)	Relative deviation other work (%)
Qiao et al. (2003)	N_2	77	2.41	0.0004	8.88	0.27	0.264	1.477	0.12	0.100	16.34	0.819	582.47
			3.04			0.43			0.23	0.261	13.45	0.854	271.12
			3.46			0.48			0.29	0.315	8.46	0.870	200.04
			3.8			0.51			0.37	0.354	4.29	0.881	138.12
			4.25			0.57			0.44	0.403	8.46	0.893	102.94
			4.93			0.65			0.51	0.470	7.87	0.907	77.84
Ravikovitch and Neimark (2001)			7.6			1.07			0.67	0.667	0.37	0.939	40.09
			8.1			1.16			0.69	0.693	0.49	0.942	36.57
			8.8			1.30			0.71	0.725	2.07	0.947	33.35
			9			1.34			0.73	0.733	0.37	0.948	29.85
			9.5			1.44			0.75	0.751	0.15	0.951	26.75
Kruk and Jaroniec (2000)	Ar	87	2.05	0.0003	12.73	0.17	0.149	1.427	0.12	0.100	16.67	0.710	491.87
			2.77			0.31			0.20	0.241	20.36	0.776	288.15
			3.08			0.37			0.26	0.308	18.39	0.796	206.28
			3.59			0.45			0.33	0.388	17.52	0.823	149.25
			3.78			0.48			0.38	0.413	8.67	0.831	118.59
			3.89			0.50			0.39	0.427	9.39	0.835	114.11
			4.15			0.54			0.43	0.457	6.23	0.844	96.39
			4.23			0.55			0.44	0.465	5.79	0.847	92.55
			4.55			0.59			0.50	0.498	0.39	0.857	71.43
			5.11			0.67			0.55	0.547	0.48	0.872	58.50
			5.53			0.73			0.60	0.579	3.48	0.881	46.81
			5.97			0.80			0.62	0.608	1.87	0.889	43.41
			6.54			0.88			0.66	0.641	2.81	0.898	36.11

Table 4.1: Database of this work and the model validation of different fluids (continued)

Reference	Fluid	T (K)	r_p (nm)	α	γ_∞ (mN/m)	t (nm)	K	m	P^{con}/P^{sat} (measured)	P^{con}/P^{sat} (calculated this work)	Relative deviation this work (%)	P^{con}/P^{sat} (calculated other work)	Relative deviation other work (%)
Morishige et al (2004)	CO_2	245	3.7	0.0001	10.36	0.74	0.211	1.908	0.60	0.564	5.74	0.945	57.83
Barsotti et al (2018)			4.4			1.07			0.60	0.696	15.06	0.954	57.74
Qiu et al. (2019)			4.89			1.33			0.73	0.754	2.80	0.958	30.66
			6.56			2.06			0.84	0.841	0.18	0.969	14.97
Russo et al. (2012)	n-C_5H_{12}	298	3.7	0.0003	15.28	0.82	0.511	2.500	0.28	0.249	10.88	0.824	194.81
Barsotti et al. (2018)			4.57			1.02			0.34	0.394	14.84	0.855	149.12
			6.32			1.61			0.62	0.616	0.27	0.893	44.53
Barsotti et al. (2018)	N_2	77	2.9	0.0004	8.88	0.41	0.264	1.477	0.31	0.241	22.12	0.847	173.25
			4.19			0.56			0.39	0.396	1.66	0.891	128.58
			8.08			1.16			0.75	0.692	7.68	0.942	25.62
Thommes et al. (2002)	Ar	87	3	0.0003	12.73	0.36	0.149	1.427	0.27	0.293	8.43	0.791	192.99
			4.25			0.55			0.42	0.468	11.34	0.848	101.79
			6.7			0.90			0.70	0.650	7.17	0.900	28.63
			11			1.56			0.87	0.790	9.20	0.938	7.83
			16			2.36			0.92	0.859	6.63	0.957	4.02
Barsotti et al. (2018)	Fluid #1	218.15	3.7	0.0002	21.33	0.80	0.211/0.511	1.908/2.500	0.55	0.555	1.09	0.924	68.31
	Fluid #2	224.35		0.0001	20.25	1.45			0.55	0.492	11.03	0.952	72.15
	Fluid #3	233.75		0.0002	20.41	1.37			0.53	0.486	7.43	0.934	77.90

Note: Surface tension of pure nitrogen and argon are from Adolphs (2016), and that of CO_2 and n-C_5H_{12} are from the Dortmund Data Bank (DDB). For single-component fluids, P^{con}/P^{sat}(calculated other work) denotes the calculated results with the original Kelvin equation, while that for multicomponent fluid represents the calculated results by Shapiro's modified Kelvin equation (Shapiro and Stenby, 1997). Fluid #1, #2, and #3 represents the binary mixture of 85 mol% CO_2+15 mol% n-C_5H_{12}, 86 mol% CO_2+14 mol% n-C_5H_{12}, and 96 mol% CO_2+4 mol% n-C_5H_{12}, respectively. One data for n-C_5H_{12} at 2.78 nm from Barsotti et al. (2018) is excluded in this database due to the suspicious measurement error.

4.2.1 Parameters determination

Compressibility factor variation constant α is determined by establishing the correlation between the gas compressibility factor and pressure up to the bulk saturation pressure (bulk dew-point pressure for mixture), as shown in Equation (4.13). In this work, the bulk saturation pressure P^{sat} of the single-component fluids are computed with the Antoine Equation from the National Institute of Standards and Technology (NIST). The P^{sat} of N_2 at 77 K and Ar at 87 K are found to be 101.325 kPa and 93.81 kPa, respectively. The bulk dew-point pressure of the multicomponent fluids are calculated with the original PR EOS, which is found to be 9.96 kPa for the mixture of 85 mol% CO_2+15 mol% *n*-C_5H_{12} at 224.35 K. The compressibility factors of N_2, Ar, and the binary mixture of CO_2+*n*-C_5H_{12} are all calculated with the modified PR EOS (Yang et al., 2019) in the pressure range of 0 to P^{sat}/P_d.

Figure 4.4 demonstrates the compressibility factor Z of N_2, Ar, and the mixture CO_2+*n*-C_5H_{12} at the desired temperatures and the pore sizes ranging from 2 to 500 nm. It is found that Z increases with the decreasing pore size. Within the pressure range of 0 to P^{sat}/P_d, the compressibility factor decreases linearly for N_2, Ar, and CO_2+*n*-C_5H_{12}. The compressibility factor variation constant α can be found as the slope of the trend line in Figure 4.4, which are 0.004, 0.003, and 0.002 for three fluids at the pore size of 3 nm, respectively. The non-unity compressibility factor in Figure 4.4 also justifies the incorporation of the real gas effect into the Kelvin equation, especially at a higher temperature. Table 4.1 lists the determined α values for all the fluids.

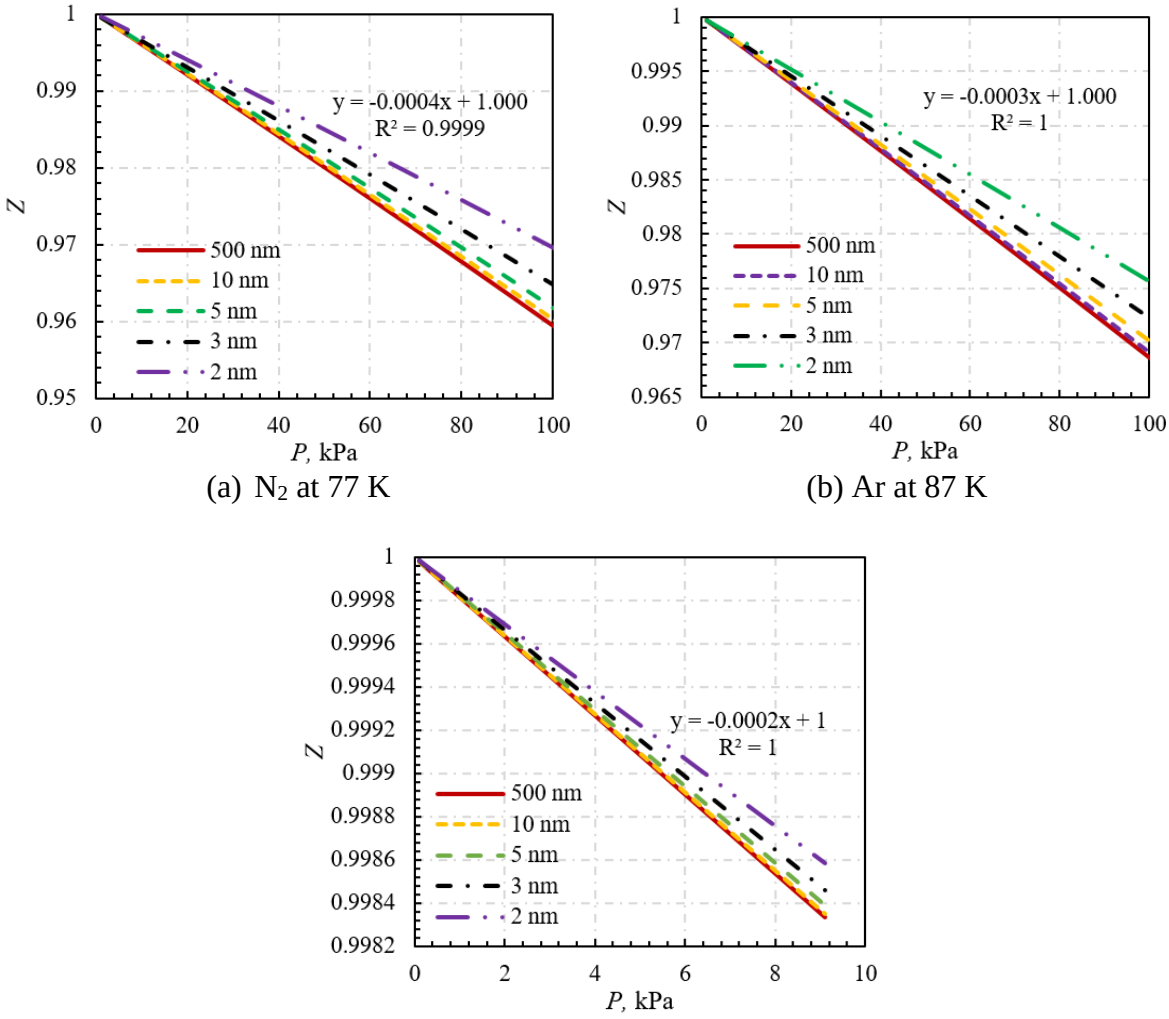

(a) N_2 at 77 K

(b) Ar at 87 K

(c) CO_2+*n*-C_5H_{12} at 224 K

Figure 4.4: Gas compressibility factor of different fluids at various pore sizes

Bulk surface tension γ_∞ of N_2 at 77 K and Ar at 87 K are 8.88 and 12.73 mN/m, respectively (Adolphs, 2016). Figure 4.5 plots the surface tension of CO_2+*n*-C_5H_{12} at bulk conditions varying with temperature, which is calculated from the algorithm demonstrated in Figure 4.3. As can be seen, the surface tension decreases with temperature because the cohesive forces decrease with an increase of molecular thermal activity. Surface tension of this binary mixture at 218.15, 224.35, and 233.75 K are 21.33, 20.25 and 20.41 mN/m, respectively. Table 4.1 lists the γ_∞ values for all the fluids.

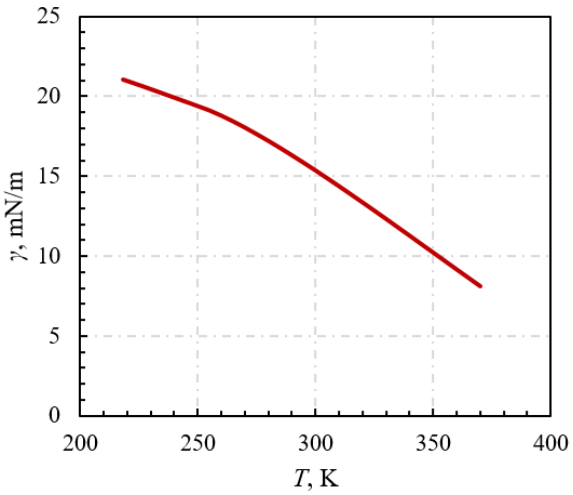

Figure 4.5: Surface tension of CO_2+*n*-C_5H_{12} bulk fluid with temperature

Multilayer adsorption thickness t of N_2, Ar, and CO_2+*n*-C_5H_{12} are calculated by Equations (4.18) and (4.37) after V_a is computed with the BET model. To calculate *t*, two constants of *C* and V_m in BET model need to be determined by curve fitting method using the experimental isotherm adsorption data which is listed in Table 4.2. Taking N_2 as an example, Figure 4.6 (a) demonstrates a good linear correlation between $x_p/[V_a(1-x_p)]$ and x_p by using the adsorption data from Thommes et al. (2002) with which the *C* and V_m values of N_2 at 77 K are calculated to be 19 and 9.78 mmol/g. Similarly, the *C* and V_m values of Ar at 87 K are 7 and 9.95 mmol/g, as shown in Table 4.2.

Because of the unavailability of the isotherm adsorption data of CO_2 and *n*-C_5H_{12} at 218.15 K, 224.35 K, and 233.75 K (data at other temperatures are available in Table 4.2), *C* and V_m values under these three temperatures cannot be obtained directly. Instead, they are predicted by establishing the correlations between *C* and V_m values versus available temperatures. Taking *n*-C_5H_{12} as an example, good linear relationships between $x_p/V_a(1-x_p)$ and x_p at various temperatures are demonstrated in Figure 4.6 (b) and the calculated *C* and V_m values based on these linear relationships are listed in Table 4.2. Hence, the correlations between *C* and V_m values versus available temperatures are demonstrated in Figure 4.7, i.e., Equations (4.43a) and (4.43b).

$$C = 2\times10^{17} / T^{5.523} \tag{4.43a}$$

$$V_m = 3.3675 - 0.006T \tag{4.43b}$$

As can be seen, both C and V_m decrease with temperature because of the exothermic feature of the adsorption process. Equations (4.43a) and (4.43b) illustrate that C decreases with temperature exponentially and V_m linearly, which is in accordance with the result of n-C_4H_{10} in Dong's work (2016).

Table 4.2: BET constants of various fluids at different temperatures

Data type	Reference	T (K)	Adsorbate	Adsorbent	C	V_m (mmol/g)
Calculated from adsorption data	Thommes et al. (2002)	77	N_2	MCM-48	19	9.78
		87	Ar	MCM-48	7	9.95
	Song et al. (2007)	303	n-C_5H_{12}	Zeolite	3296	1.52
		323			2294	1.45
		348			1882	1.33
		373			1228	1.02
		395			1072	0.85
		423			635	0.79
	Russell et al. (2017)	217	CO_2	ZIF 8	94	7.09
	Zhu et al. (2014)	273.15		Carbon	16	3.21
		298.15		Carbon	6	1.97
Predicted at desired temperatures		218.15	n-C_5H_{12}		11903	2.13
		224.35			10443	2.09
		233.75			8621	2.02
		218.15	CO_2		86	6.94
		224.35			67	6.54
		233.75			47	5.94

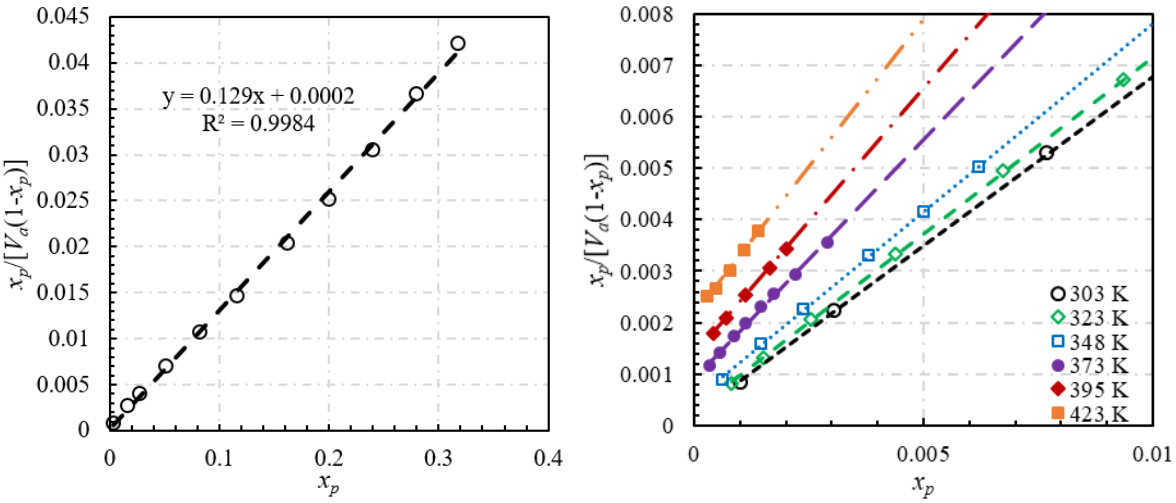

(a) N_2 (b) n-C_5H_{12}

Figure 4.6: Linear fitting of BET model for N_2 and n-C_5H_{12}

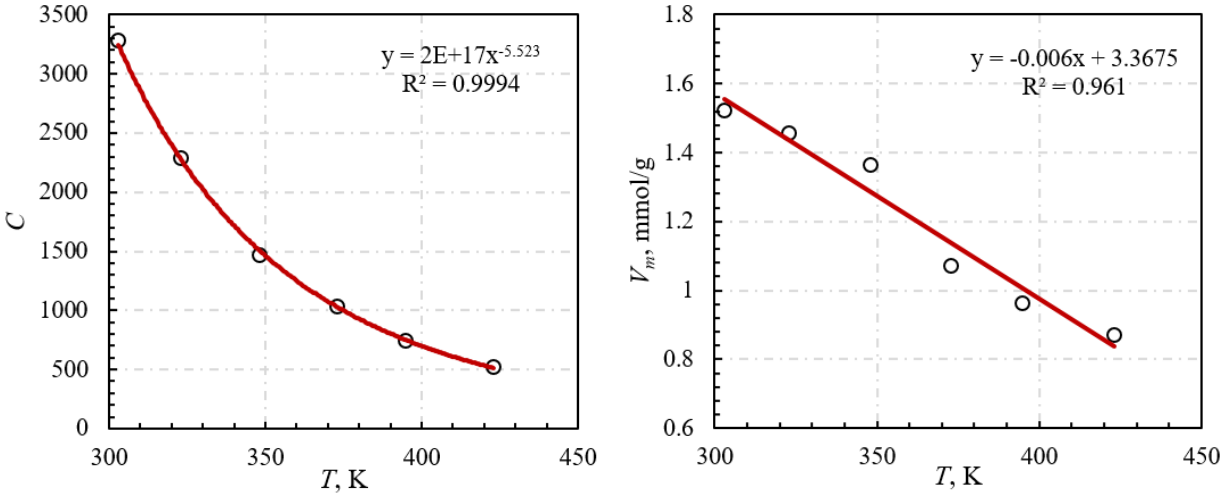

(a) C (b) V_m

Figure 4.7: BET constants variation of n-C_5H_{12} with temperature

By using Equations (4.43a) and (4.43b), the BET constants at 218.15 K, 224.35 K and 233.75 K can be predicted. Similarly, the BET constants of CO_2 can also be obtained, as demonstrated in Table 4.2. Consequently, the multilayer adsorption thickness t at desired temperatures can be computed. For example, the multilayer adsorption thickness t of n-C_5H_{12} in a pore of 3.7 nm is 0.82 nm at 298 K. Table 4.1 lists the determined t values for all the fluids.

Molecule-wall interaction potential constants K* and *m of single-component fluids can be obtained by the regression method using the experimental capillary condensation pressures. The first group of pure N_2 data (11 data points in total) in Table 4.1 are used as an example. With Equation (4.21), the molecule-wall interaction potential *F(t)* at different pore sizes can be calculated and correlated with the multilayer adsorption thickness *t*, as shown in Figure 4.8, i.e., Equation (4.44).

$$F(t) = 0.264RT\left(t\right)^{1.477} \tag{4.44}$$

Hence, the *K* and *m* values for N_2 at 77 K are 0.264 and 1.477, respectively. With a similar approach, the *K* and *m* values of other single-component fluids (Ar, CO_2, and *n*-C_5H_{12}) can be obtained and listed in Table 4.1. As can be seen, both *K* and *m* values are different for various fluids, representing the strength variation of molecule-wall interaction for different adsorbate-adsorbent system. Table 4.1 lists the determined *K* and *m* values for all the fluids.

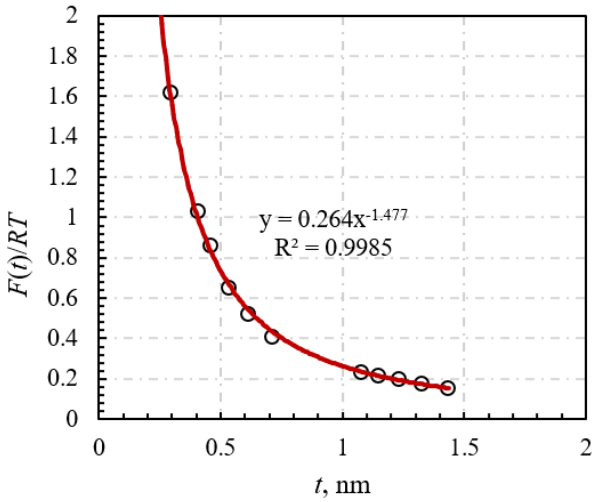

Figure 4.8: Correlation between the molecule-wall interaction potential and *t* for N_2 at 77 K

4.2.2 Validation results

Subsequently, the capillary condensation pressure of both single- and multicomponent fluids at different pore sizes are calculated with the modified Kelvin equation in this work, listed as P^{con}/P^{sat} (calculated this work) in Table 4.1. In addition, the capillary condensation pressure of single-component fluids is also calculated with the original Kelvin equation and that of multicomponent fluid with Shapiro's modified Kelvin equation, listed as P^{con}/P^{sat} (calculated other work) in Table 4.1. All the calculated results are compared with the collected experimental data, P^{con}/P^{sat} (measured). Overall, the relative deviations for all 42 data points are 7.57% by using this work and 113.89% by using other work, indicating that the modified Kelvin equation of this work is much more accurate in calculating the suppressed capillary condensation pressure of confined fluids in nanopores. This, on the other hand, reflects that the impact factors incorporated in this work can accurately represents the physical mechanism of the capillary condensation phenomenon.

Single-component fluids of N_2, Ar, CO_2, and n-C_5H_{12}

As demonstrated in Table 4.1, the overall relative deviation of P^{con}/P^{sat} (calculated this work) for N_2, Ar, CO_2, and *n*-C_5H_{12} are 6.70% (14 data points), 8.60% (18 data points), 5.95% (4 data points), and 8.66% (3 data points), respectively. The relative deviation of most data points is small (less than 10%), except for few data points. This proves that the modified Kelvin equation in this work is satisfactory to calculate the suppressed capillary condensation pressure of single-component fluids in nanopores. In comparison, the corresponding overall relative deviation of P^{con}/P^{sat} (calculated other work) are 133.33%, 119.37%, 40.30%, and 129.49%, respectively, indicating that the P^{con}/P^{sat} calculated by the original Kelvin equation are of enormous error, particularly when the pore size is below 4 nm. For example, the P^{con}/P^{sat} values of N_2 at 77 K and 2.41 nm calculated by the original Kelvin equation is 0.819, which is 582.47% higher than the experimental data 0.12. Figure 4.9 plots the P^{con}/P^{sat} with pore size of the four single-component

fluids obtained by different approaches. It shows that this work reaches an excellent agreement with the measured data for all four pure components. However, the original Kelvin equation cannot provide a reliable calculation, particularly in the pores smaller than 10 nm.

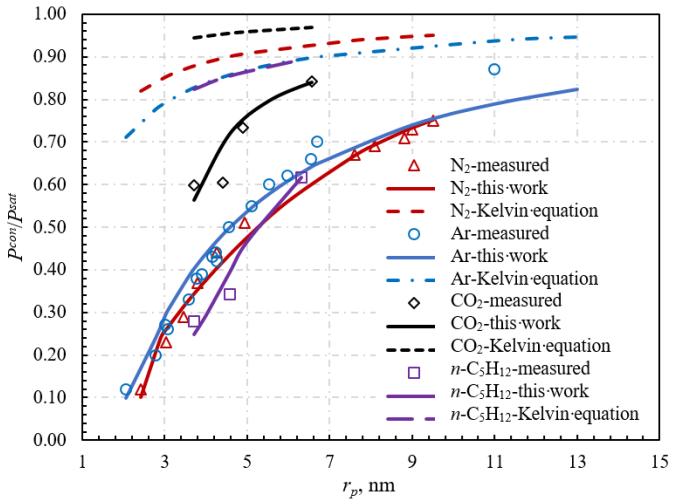

Figure 4.9: P^{con}/P^{sat} of single-component fluids with pore size (symbols denotes the measured data; solid lines denotes the calculated results using this work; and dashed lines denotes the calculated results using the original Kelvin equation)

In addition, it can be seen in Table 4.1 that the capillary condensation pressure of single-component fluids is significantly suppressed in nanopores and the degree of suppression decreases with increasing pore size. At 4 nm, the P^{con}/P^{sat} (measured) of N_2, Ar, CO_2, and *n*-C_5H_{12} are 0.40, 0.41, 0.60, and 0.31 (obtained by interpolation), showing the capillary condensation pressures are suppressed by 60%, 59%, 40% and 69%, respectively. At 6 nm, the values are 0.62, 0.62, 0.83, and 0.61, with decreasing suppressions of 38%, 38%, 17% and 39%, respectively. It is found that *n*-C_5H_{12} yields the largest suppression among these four single-component fluids, while CO_2 yields the smallest suppression. It is attributed to the fact that *n*-C_5H_{12} has the largest molecule with the diameter of 0.62 nm (Sing and Williams, 2004) and CO_2 has the smallest molecule with the

diameter of 0.33 nm. Within a same pore, the confinement/proximity effect of the larger molecules is stronger.

Binary mixture of CO_2+n-C_5H_{12}

As aforementioned, the capillary condensation pressure of a multicomponent fluid is closer to the bulk dew-point pressure. As can be seen in Table 4.1, the measured P^{con}/P^{sat} for the binary mixture CO_2+*n*-C_5H_{12} with three compositions at three temperatures are 0.55, 0.55, and 0.53, respectively. It implies that all the capillary condensation pressures are reduced by approximate 50%. The overall relative deviation by using this work is 6.52% for three points, proving that the extended Kelvin equation in this work can be applied to multicomponent fluids. In comparison, the overall relative deviation by using the Shapiro's modified Kelvin equation, listed as P^{con}/P^{sat} (calculated other work), is calculated to be 72.79%. Such a large deviation is because only the real gas effect was considered in Shapiro's work, instead of multiple physical mechanisms, such as adsorption and molecule-wall interaction.

Analyses of Impact factors

The analyses of impact factors are conducted for N_2 to clarify the cumulative contributions of the four factors in modifying the original Kelvin equation. Figure 4.10 (a) presents the measured data and the calculated results with cumulative consideration of the real gas effect *Z*, pore size effect on surface tension γ, the multilayer adsorption *t*, and the molecule-wall interaction potential *F(t)* in the model. The calculated one with the original Kelvin equation (black curve) yields the largest deviation from the measurement. When *Z* is considered in the model (green curve), the curve shifts downward slightly but still far from the measured points. Purple curve resulting from considering both *Z* and γ is also a slight improvement. Even though adding one more factor *t* in the model can improve the prediction in the small pores to a certain extent, but the results are still

unsatisfactory (yellow curve). Finally, the involvement of *F(t)* in the model significantly shifts the curve downward and accurately matches the measured data. Hence, the molecule-wall interaction potential *F(t)* contributes most to the confinement effect and thus is the most important factor. The contribution of each of the four factors are also considered separately and calculated for N_2 at 2.41 nm, as illustrated in Figure 4.10 (b). It is found that the contribution of *F(t)* accounts for 68% and 18% comes from *t*. The weights caused by *Z* and γ are relatively small which are 11% and 3%, respectively. Therefore, the parameter of *F(t)* which reflects the molecule-wall interaction potential cannot be neglected when the fluid is confined in nanopores.

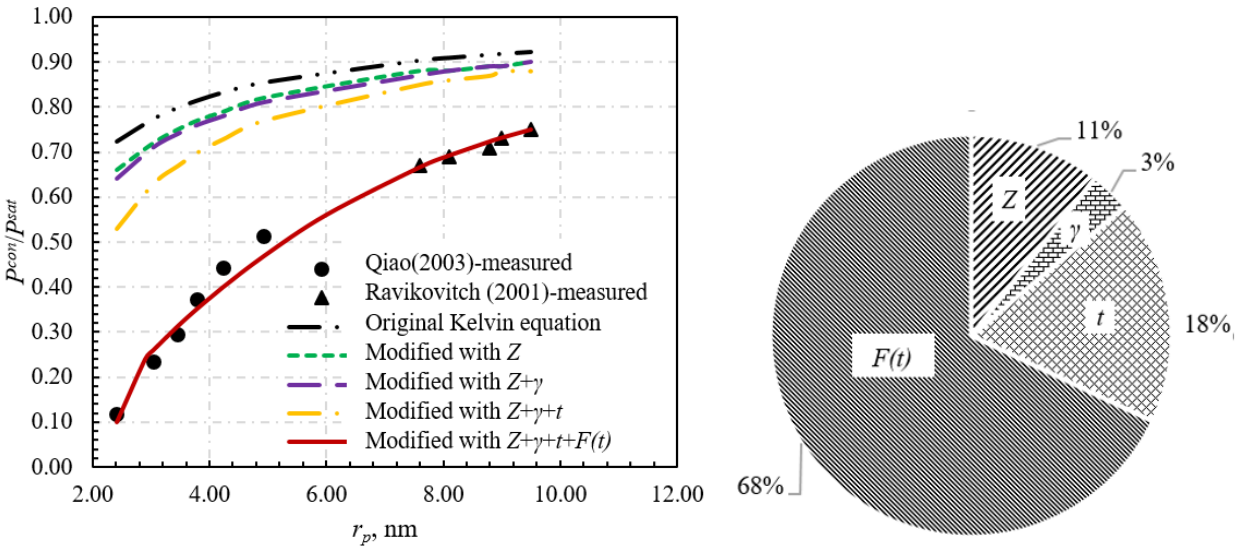

(a) Cumulative effect (b) Contribution break down at 2.41 nm

Figure 4.10: Effect analyses of real gas effect *Z*, pore size effect on surface tension γ, multilayer adsorption *t*, and molecule-wall interaction potential *F(t)* on P^{con}/P^{sat} of N_2 with pore size: (a) cumulative effect of four factors; (b) effect ratios of different factors at 2.41 nm.

4.3 Model Applications

The validated models are then applied to predict the capillary condensation pressures of fluids including CO_2 (single-component fluid) and a synthetic mixture of 15 mol% CO_2 + 40 mol% *n*-C_5H_{12} + 45 mol% *n*-C_6H_{14} at different temperatures. The results are plotted in Figure 4.11, where the bulk saturation pressure curve is included for comparison purpose. The bulk saturation pressure of CO_2 is obtained from the Dortmund Data Bank (DDB), while that for the synthetic mixture is calculated by the original PR EOS.

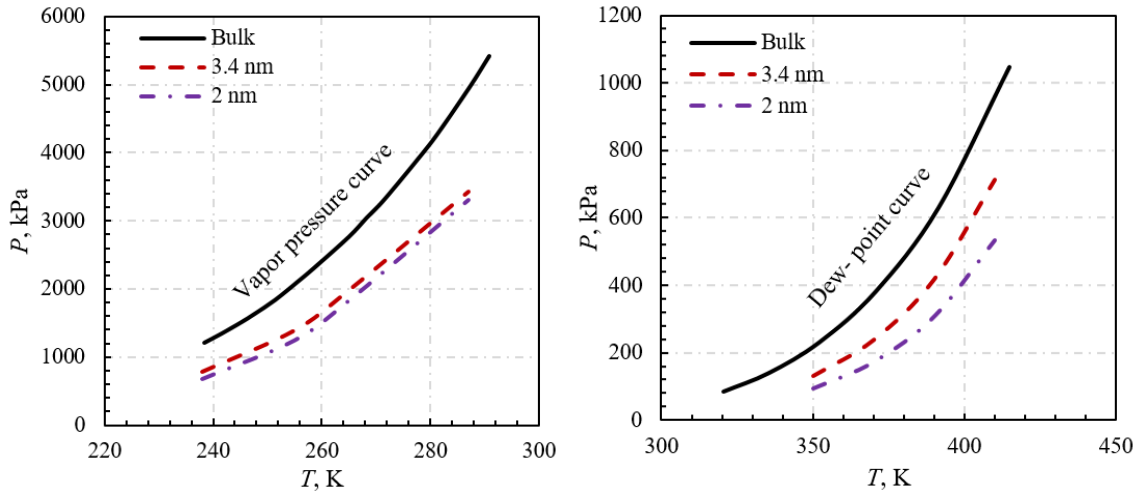

(a) CO_2 (b) CO_2+*n*-C_5H_{12}+*n*-C_6H_{14}

Figure 4.11: Capillary condensation pressure with temperature at pore sizes of 3.4 nm and 2 nm for (a) CO_2 and (b) 15 mol% CO_2 + 40 mol% *n*-C_5H_{12} + 45 mol% *n*-C_6H_{14}

It can be seen that the capillary condensation pressure of the confined fluids, both single-component and multicomponent, are lower than the bulk saturation pressure (lower dew-point pressure for mixture), implying that the confined fluids condense at a lower pressure than the bulk fluids because of the effect of pore confinement. Moreover, with the decease of pore size, the capillary condensation pressure is further suppressed, resulting from a stronger confinement effect caused by stronger molecule-wall interaction. The capillary condensation pressure of CO_2 at 265 K is suppressed by 28.17% (2767.5 kPa to 1988.0 kPa) and 33.96% (2767.5 kPa to 1827.7 kPa) in

3.4 nm and 2 nm pores, respectively. As for the mixture of CO_2+*n*-C_5H_{12}+*n*-C_6H_{14}, the capillary condensation pressure at 390 K is suppressed by 25.28% (600.8 kPa to 448.9 kPa) and 43.16% (600.8 kPa to 341.5 kPa) in 3.4 nm and 2 nm pores, respectively. Therefore, it is necessary to reasonably consider the confinement effect, which consists of various physical mechanisms as incorporated in this work, to thoroughly investigate the capillary condensation phenomenon.

4.4. Summary

A modified Kelvin equation with incorporation of the real gas effect, the pore size effect on surface tension, the multilayer adsorption, and the molecule-wall interaction potential has been successfully proposed to investigate the capillary condensation phenomenon of both single- and multicomponent fluids in nanopores. Model validation demonstrates that the proposed model is applicable to calculate the suppressed capillary condensation pressure of confined fluids in nanopores with the overall relative deviation of 7.65% and 6.52% for single- and multicomponent fluids, respectively. Moreover, the impact factor analyses illustrate that the molecule-wall interaction potential has the most significant contribution to the modification, while the pore size effect on surface tension has the least contribution among the four factors. By calculation, the capillary condensation pressure is reduced from 2767.5 kPa (bulk) to 1827.7 kPa (2 nm) for CO_2 at 265 K and from 600.8 kPa (bulk) to 341.5 kPa (2 nm) for the mixture CO_2+*n*-C_5H_{12}+*n*-C_6H_{14} at 390 K, respectively.

Chapter 5: Minimum Miscibility Pressure in Unconventional Reservoirs

Minimum miscibility pressure (MMP), as the lowest pressure above which the injected gas and the reservoir oil achieve dynamic miscibility, is an important parameter for designing and optimizing the miscible gas injection EOR in unconventional reservoirs. Since MMP is closely related to the phase behavior of confined fluids, it is inevitably affected by the nanoscale confinement. The objective of this chapter is to investigate the impact of nanoscale confinement on MMP of unconventional reservoir fluids and to recognize a reliable theoretical approach to calculate the MMP values in unconventional reservoirs. The modified PR EOS applicable for confined fluid characterization is applied to perform the EOS simulation of the vanishing interfacial tension (VIT) experiments. The MMP of a binary mixture at bulk and 50 nm are obtained via the VIT simulations. Meanwhile, the multiple mixing cell (MMC) algorithm coupled with the same modified PR EOS is applied to compute the MMP for the same fluid system. Comparison of the calculated results to the experimental values will recognize an accurate approach to determine the MMP of confined fluid systems. Moreover, this approach would be applied to predict the MMP values of both Bakken and Eagle Ford oil at different pore sizes with various injected gases.

5.1 Modeling Methodology

Theoretical methods of VIT simulation and MMC algorithm are modified and applied in this work. The MMPs of both synthesized mixture and unconventional reservoir fluids within nanopores are calculated and compared with the experimental measurements. The modified PR EOS proposed in Chapter 3 is incorporated to reflect the nanoscale confinement within various nanoscale pores and to perform the vapor-liquid equilibrium (VLE) calculations for confined fluids.

5.1.1 VIT simulation

In VIT experiment, the interfacial tension (IFT) of the gas-oil mixture are measured at a sequence of pressures. The MMP is estimated to be the pressure at which the IFT extrapolates to zero when plotted against pressure (Orr and Jessen, 2007). For VIT simulation, instead of direct experimental measurements, the IFT between the reservoir fluid and the injected gas is calculated by using the parachor approach algorithm (Yang et al., 2019), where the modified PR EOS is applied to conduct the VLE calculation. The algorithm can be summarized as below:

Step 1: Input temperature, pressure, pore size, and properties of each components.

Step 2: Estimate initial K values using the Wilson equation.

$$K_i = \frac{\exp[5.37(1+\omega_i)(1-T_{ri}^{-1})]}{P_{ri}} \tag{5.1}$$

Step 3: Conduct flash calculation with Rachford-Rice equation to obtain liquid and vapor composition.

$$\sum_{i=1}^{N}(y_i - x_i) = \sum_{i=1}^{N}\frac{z_i(K_i-1)}{1+F_v(K_i-1)} = 0 \tag{5.2}$$

Step 4: Specify initial guess of the capillary pressure.

Step 5: Calculate the actual capillary pressure using the equations below:

$$\sigma^{1/E} = \sum_{i=1}^{n} p_i(x_i\rho_L - y_i\rho_V) \tag{5.3}$$

$$E = 3.583 + 0.16(\rho_L - \rho_V) \tag{5.4}$$

$$p_i = (8.21307 + 1.97473\omega_i)T_{ci}^{1.30406}P_{ci}^{-0.82636} \tag{5.5}$$

$$P_{cap} = \frac{2\sigma \cos\theta}{r_p} \tag{5.6}$$

Step 6: Check if the actual capillary pressure is equal to the initial guess or within a specified tolerance. If yes, continue with the next step, if not, update the capillary pressure value and repeat step 4 to step 6.

Step 7: Calculate the fugacity of both liquid and vapor phase using the modified PR EOS and check if these two are equal or within a specified tolerance. If the fugacity of liquid and vapor phase are equal, output the IFT, if not, update K values and repeat step 2 to step 7.

Step 8: Compute the IFT values under a sequence of pressures and determine the MMP at the specific temperature and pore size.

This algorithm can generally calculate the IFT to small values at high pressure. The extrapolation of IFT to zero can be achieved by applying several lowest IFT values that are close to zero, where the MMP can be located.

5.1.2 MMC method

The MMC method applied in this work is based on the algorithm proposed by Ahmadi and Johns (2011), in which cell to cell contacts between equilibrium phases are repeatedly performed. Due to the consideration of nanoscale confinement, the EOS model for vapor-liquid equilibrium calculation in this algorithm is the modified PR EOS proposed in Chapter 3, instead of the original PR EOS. This algorithm can be summarized as the following steps:

Step 1: Specify temperature and initial pressure. The temperature is constantly equal to the reservoir temperature and the initial pressure should be a value significantly below the MMP (500 psi is often used).

Step 2: Start with mixing two cells filled with the injected gas and reservoir oil, respectively. The overall composition is obtained by flash calculation conducted using the modified PR EOS with consideration of the nanoscale confinement.

Step 3: By assuming gas phase moving ahead of oil phase, mix the liquid and vapor phase at equilibrium to obtain new compositions for the next contacts, as in Figure 5.1.

Step 4: Continue mixing two adjacent cells until N_c-1 key tie lines are developed, as illustrated in Figure 5.2.

Step 5: The length of key tie line is calculated by using Equation (5.7) and the minimum tie line length is stored under the specific pressure.

$$TL = \sqrt{\sum_{i=1}^{n} (x_i - y_i)^2} \tag{5.7}$$

Step 6: Update the pressure value and repeat step 2 to step 5 until the MMP value is obtained by computing the minimum tie line length extremely close to zero.

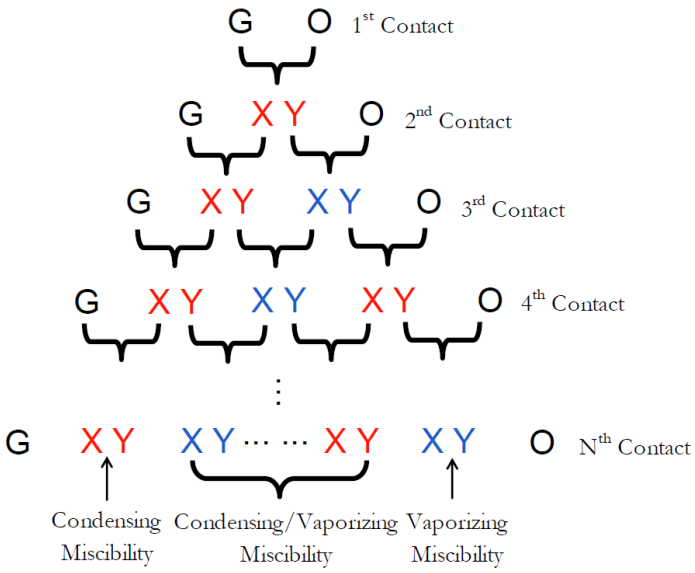

Figure 5.1: Illustration of multiple contact in MMC (Ahmadi and Johns, 2011)

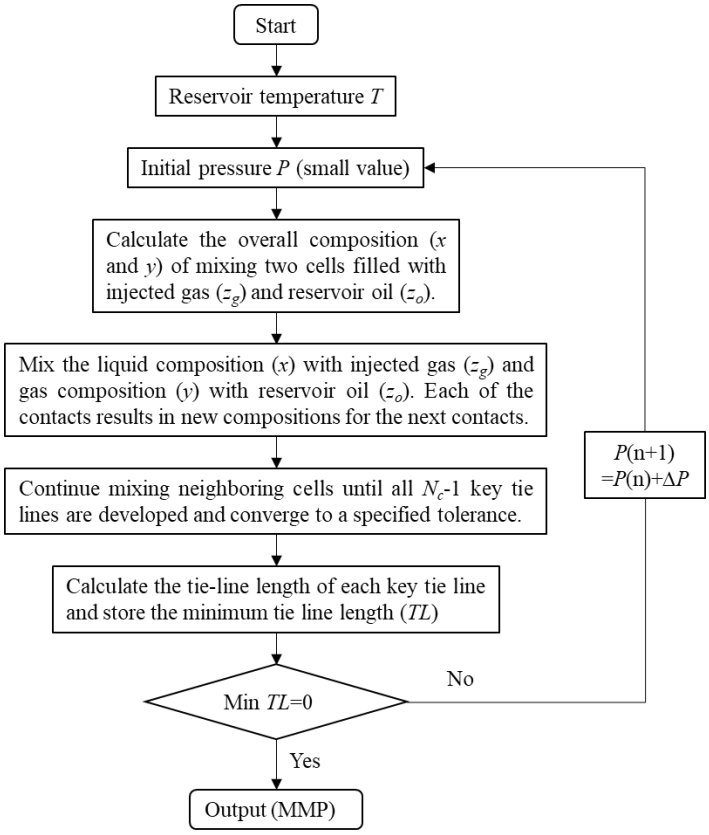

Figure 5.2: MMC algorithm for MMP determination

5.2 Applications on Synthesized Fluids

5.2.1 Methodology validation

Bao et al. (2020) measured the MMP of the binary mixture CO_2+*n*-C_{10} within nanoconfined channels of 50 nm using nanofluidic experiments. To validate the accuracy of both methods regarding confined fluids, the MMP of binary mixture CO_2+*n*-C_{10} are computed via both the VIT simulation and the MMC algorithm coupled with the modified PR EOS. Comparison of these calculated results to the measured MMP values are performed to recognize which method has higher accuracy in determining the MMP of confined fluid systems.

BIP determination

Due to the lack of validation in the original work, the BIP of this binary mixture is tuned based on the experimental data of pressure-composition diagram of CO_2 at 319.11 K from Jimenez-Gallegos et al. (2006), as demonstrated in Table 5.1 and Figure 5.3.

Table 5.1: Properties of Binary mixture

Components	T_c, °F	P_c, psi	w	*BIP* (tuned)
CO_2	87.9	1071	0.255	
n-C_{10}	652.1	305.7	0.49	0.1064

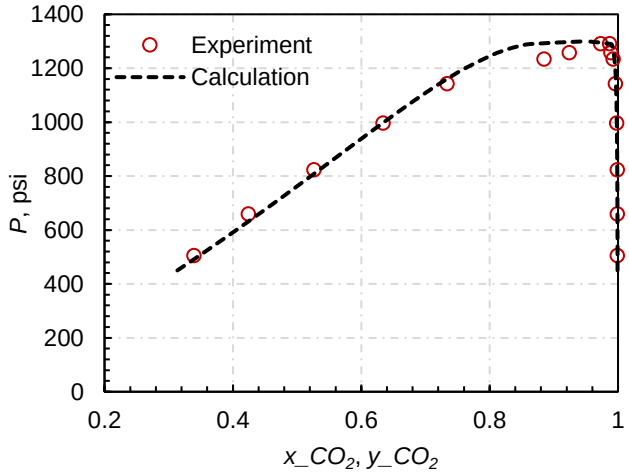

Figure 5.3: Measured pressure-composition diagram vs theoretical results

As shown in Figure 5.3, the well-matched calculation with the experimental data illustrates that the tuned BIP value is of high accuracy, which can be further used for the MMP calculation of this binary mixture.

VIT calculation

The IFT values between CO_2 and n-C_{10} under different pressures are calculated by the proposed parachor approach algorithm. Figure 5.4 demonstrates the IFT variation with pressure for the binary mixture within bulk and 50 nm. The MMP values can be obtained by extrapolating the plot of IFT versus pressure to zero.

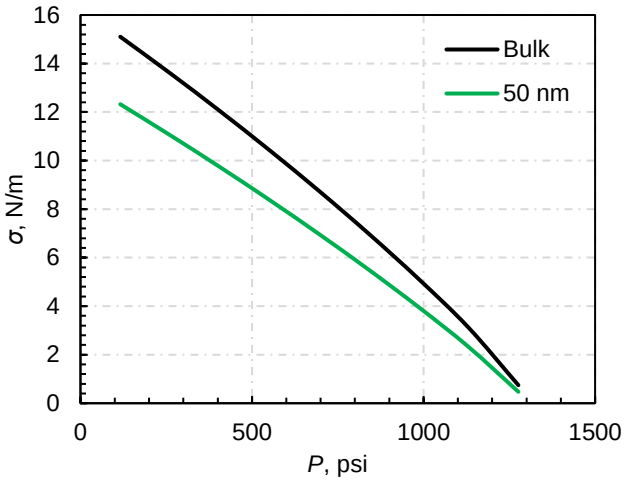

Figure 5.4: IFT with pressure for the binary mixture CO_2+*n*-C_{10}

MMC calculation

Figure 5.5 illustrates the tie line development for the binary mixture CO_2+*n*-C_{10} at 303.15 K, 800 psi and the quaternary mixture CO_2+C_1+*n*-C_4+*n*-C_{10} from Teklu et al. (2014) at 344.26 K, 1200 psi. The results of the quaternary mixture CO_2+C_1+*n*-C_4+*n*-C_{10} are shown for comparison. As demonstrated in Figure 5.5 (a), the tie line length (TL) of the binary mixture keeps one constant value with the contact number. While the TL values of the quaternary mixture in Figure 5.5 (b) vary with the increasing contact number. For the quaternary mixture, the key tie lines are fully developed after about 50 contacts with three types of tie lines: gas, oil, and crossover. The crossover tie line controls the miscibility because of its least length. Moreover, the TL is obviously decreased in confined space for both binary and quaternary mixtures, representing that the miscibility can be achieved at lower pressure for the confined fluid systems within nanopores.

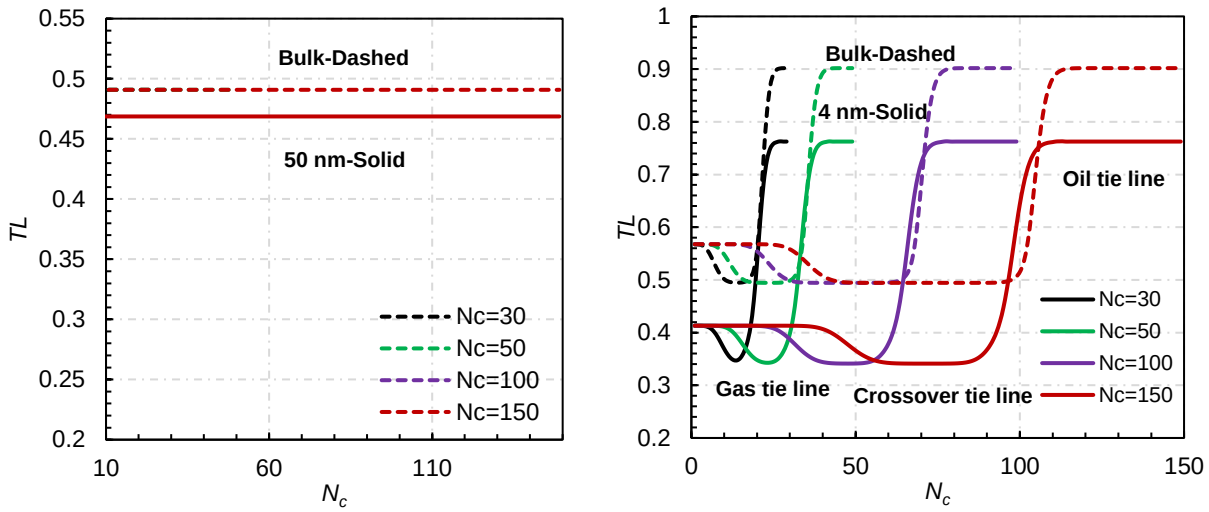

(a) binary mixture CO_2+*n*-C_{10} (b) quaternary mixture CO_2+C_1+*n*-C_4+*n*-C_{10}

Figure 5.5: Tie line development for the binary and quaternary mixtures

Figure 5.6 illustrates the minimum tie line length variation with pressure of the binary mixture at bulk and 50 nm. The MMP values are obtained by computing the TL versus pressure to zero or highly approximating zero.

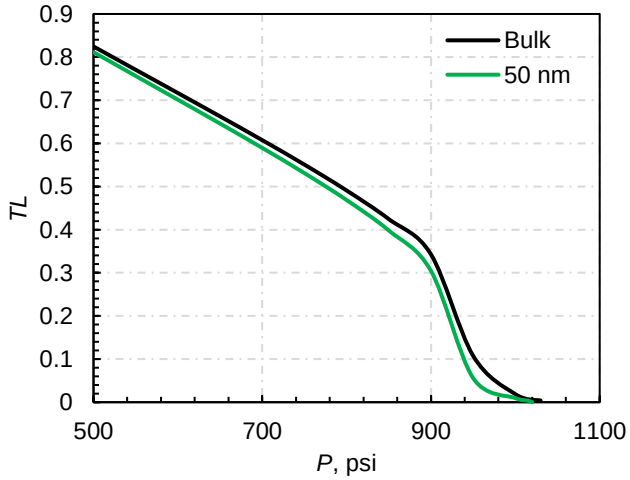

Figure 5.6: TL vs pressure for the binary mixture CO_2+*n*-C_{10}

5.2.2 Accuracy comparison

Table 5.2 listed the comparison of the MMP values of binary mixture CO_2+*n*-C_{10} at bulk and 50 nm obtained by experiments, VIT simulation, and MMC method. As can be seen, the errors for VIT simulation and MMC method in calculating the MMP at bulk space are 38.2% and 8.2%, while the values at 50 nm are 37.5% and 6.3%, respectively. Despite that the VIT experiments are of similar accuracy with the slim tube experiments (Hawthorne et al., 2016), the theoretical VIT simulation is of lower accuracy. On the contrary, MMC method is much more accurate than the VIT simulation in calculating the MMP values of both bulk and confined fluids. Thus, the MMC algorithm incorporating with the modified PR EOS should be applied for the calculation of the confined MMP in unconventional reservoirs.

Table 5.2: MMP values of different methods

CO_2+*n*-C_{10}	Bulk, psi	50 nm, psi	Error (bulk), %	Error (50 nm), %
Experiment	956.8	955.2	-	-
VIT simulation	1322	1313	38.2	37.5
MMC method	1035	1015	8.2	6.3

5.3 Applications on Reservoir Fluids

The MMP values of hydrocarbon and non-hydrocarbon injection in both Bakken and Eagle Ford reservoirs are calculated via the modified MMC algorithm.

5.3.1 Bakken oil

The fluid properties and binary interaction parameters (BIPs) of Bakken oil are from Yu et al. (2015), as illustrated in Table 5.3 and 5.4. Figure 5.7 shows the tie line development for Bakken oil at bulk and 10 nm with 100% CO_2 injection. As can be seen, the critical tie line is almost fully developed after 50 contacts. The contact number is taken as 100 for the determination of the MMP values. Like the synthesized mixtures, the TL is also generally decreased within nanoscale pores for Bakken oil. Figure 5.8 manifests the determination of MMP for Bakken oil at reservoir

temperature (240 °F) within different pore sizes. As can be seen, the TL values have a sharp decrease at pressures near the MMP, which is in accordance with the results of Teklu et al. (2014).

Table 5.3 Bakken oil components and properties (Yu et al., 2015)

Component	z_i	P_c, atm	T_c, K	w	Parachor
CO_2	0.0002	72.8	304.2	0.225	78
N_2	0.0004	33.5	126.2	0.04	41
C_1	0.25	45.4	190.6	0.008	77
C_2-C_4	0.22	42.54	363.3	0.1432	145.2
C_5-C_7	0.2	33.76	511.56	0.2474	250
C_8-C_9	0.13	30.91	579.34	0.2861	306
C_{10+}	0.1994	21.58	788.74	0.6869	686.3

Table 5.4: Binary interaction parameters (Yu et al., 2015)

Component	CO_2	N_2	C_1	C_2-C_4	C_5-C_7	C_8-C_9	C_{10+}
CO_2	0	-0.02	0.103	0.1327	0.1413	0.15	0.15
N_2	-0.02	0	0.031	0.0784	0.1113	0.12	0.12
C_1	0.103	0.031	0	0.0078	0.0242	0.0324	0.0779
C_2-C_4	0.133	0.0784	0.0078	0	0.0046	0.0087	0.0384
C_5-C_7	0.141	0.1113	0.0242	0.0046	0	0.0006	0.0169
C_8-C_9	0.15	0.12	0.0324	0.0087	0.0006	0	0.0111
C_{10+}	0.15	0.12	0.0779	0.0384	0.0169	0.0111	0

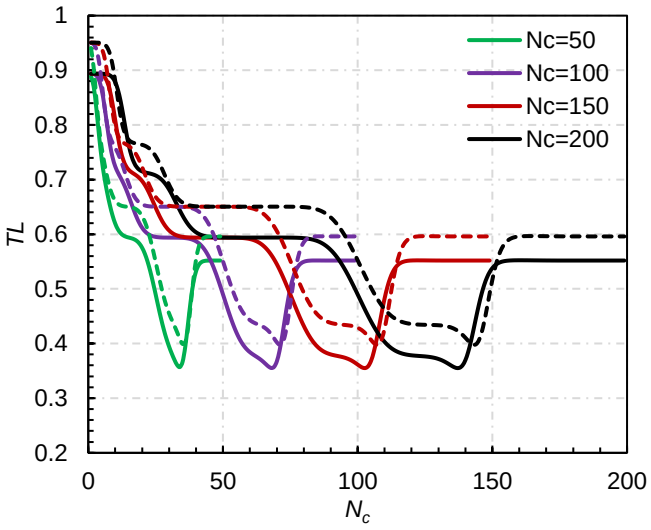

Figure 5.7: Tie line development for the Bakken oil at Bulk and 10 nm

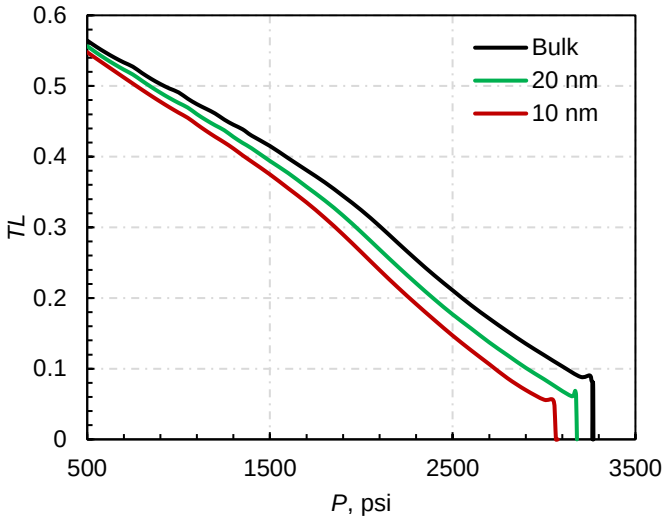

Figure 5.8: Determination of MMPs for Bakken oil at 240 °F

5.3.2 Eagle Ford oil

The fluid properties and binary interaction parameters (BIPs) of Eagle Ford oil are from Yu et al. (2019), as illustrated in Table 5.5 and 5.6.

Table 5.5: Eagle Ford oil components and properties (Yu et al., 2019)

Component	Molar fraction	P_c, atm	T_c, K	V_c	Molecular weight g/mol	w	Parachor
CO_2	0.01183	72.8	304.2	0.094	44.01	0.225	78
N_2	0.00161	33.5	126.2	0.0895	28.01	0.04	41
C_1	0.11541	45.4	190.6	0.099	16.04	0.008	77
C_2-C_5	0.26438	36.5	274.74	0.2293	52.02	0.1723	171.07
C_6-C_{10}	0.38089	25.08	438.68	0.3943	103.01	0.2839	297.42
C_{11+}	0.22588	17.55	740.29	0.887	267.15	0.6716	661.45

Table 5.6: Binary interaction parameters (Yu et al., 2019)

Component	CO_2	N_2	C_1	C_2-C_5	C_6-C_{10}	C_{11+}
CO_2	0	0.02	0.103	0.1299	0.15	0.15
N_2	0.02	0	0.031	0.082	0.12	0.12
C_1	0.103	0.031	0	0.0174	0.0462	0.111
C_2-C_5	0.1299	0.082	0.0174	0	0.0073	0.0444
C_6-C_{10}	0.15	0.12	0.0462	0.0073	0	0.0162
C_{11+}	0.15	0.12	0.111	0.0444	0.0162	0

Figure 5.9 shows the tie line development for the Eagle Ford oil at bulk and 10 nm. Like the results of Bakken oil, the critical tie line for the Eagle Ford oil is also nearly developed after 50 contacts. Contact number of 100 is selected for the further determination of MMP. Figure 5.10 illustrates the determination of the MMPs of Eagle Ford oil at different pore sizes at reservoir temperature of 270 °F. Just like Bakken oil, the TL values of Eagle Ford oil also show greater decrease near the MMP, but not drastically sharp. The MMPs are located at the pressure where the TL value is highly close to zero.

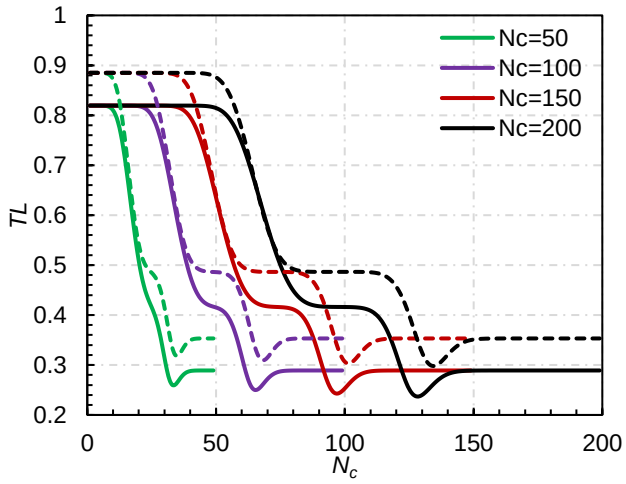

Figure 5.9: Tie line development for the Eagle Ford oil at Bulk and 10 nm

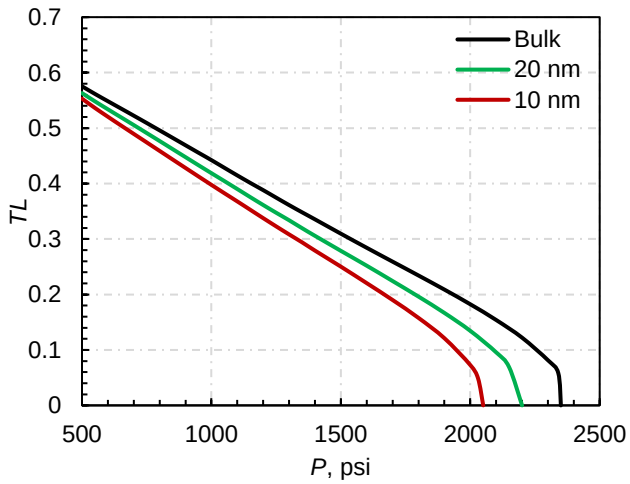

Figure 5.10: Determination of MMPs for Eagle Ford oil at 270 °F

5.3.3 MMP of different injected gases

For the gas huff-n-puff in unconventional reservoirs, different types of gases, such as CO_2, natural gas, or their mixture would be injected. Hence, the MMP values of the Bakken and the Eagle Ford oil samples with different injected gases are calculated and demonstrated in Table 5.7.

Table 5.7: MMP of different injected gases into Bakken and Eagle Ford oil

Injected gas	MMP of Bakken oil (240 °F), psi			MMP of Eagle Ford oil (270 °F), psi		
	Bulk	20 nm	10 nm	Bulk	20 nm	10 nm
100 % CO_2	3266	3177	3063	2345	2175	2040
100% C_1	4425	4150	3850	2428	2323	2133
50% CO_2+ 50% C_1	4385	3975	3825	2345	2175	2036
70% CO_2+ 30% C_1	3925	3725	3655	2335	2165	2034
90% CO_2+ 10% C_1	3500	3250	3175	2325	2160	2032

Olawale (2016) obtained the bulk MMP of Bakken oil with 100% CO_2 injection at 237 °F as 3350 psi using rising bubble apparatus. Hawthorne et al. (2016) measured the MMP of Bakken oil with 100% CH_4 injection at 230 °F (110 °C) as 4512 psi (31.11 MPa) by VIT method. Although the compositions and properties of the crude oil are not listed in these experimental works, both measured values are highly close to the calculation results in Table 5.7, representing the validity of the MMC method.

Moreover, the MMP values of unconventional reservoir oil within nanopores are drastically suppressed. Smaller pore size results in lower MMPs. For 100% CO_2 injection, the MMP suppression rate of Bakken oil and Eagle Ford oil at 10 nm are 6.22% and 13.01%, respectively. Compared with Bakken oil, the MMP values of Eagle Ford oil is much lower, which is probably the reason for the satisfying performance of natural gas huff-n-puff EOR in Eagle Ford formations while that for Bakken shale is unsatisfactory (Hoffman, 2018, 2019). In addition, the mix of CH_4 into CO_2 increases the MMP of Bakken oil. The higher CH_4 fraction induces higher MMP values, which matches well with the results of Hawthorne et al. (2016) where the methane

mole fraction linearly raises CO_2 MMPs. For Eagle Ford oil, the mix of CH_4 into CO_2 can somehow decrease the CO_2 MMP values at specific composition range (less than 50%).

5.4 Summary

This chapter investigated the impact of nanoscale confinement on MMP of confined fluid systems and recognized an accurate theoretical approach in calculating the confined MMP values in unconventional reservoirs. The modified PR EOS applicable for confined fluid characterization is applied to perform the vapor-liquid flash calculation. By comparing the calculated MMP values of confined mixture CO_2+*n*-C_{10} using both VIT simulation and the MMC algorithm to the experimental results, the MMC method is recognized to have higher accuracy in determining the MMP of confined fluid systems. Moreover, nanoscale confinement results in the drastic suppression of MMP and the suppression rate increases with decreasing pore size. For 100% CO_2 injection, the MMP suppression rate of Bakken oil and Eagle Ford oil at 10 nm are 6.22% and 13.01%, respectively. The drastic suppression of MMP is highly favorable for the miscible gas injection EOR in unconventional reservoirs. The mix of CH_4 into CO_2 can either decrease or increase the MMP values of unconventional reservoir fluids depending on the compositions of the reservoir fluid and the injected gases.

Chapter 6: Compositional Simulation of Unconventional Reservoirs

The primary recovery factor of unconventional reservoir remains low because of the extremely low matrix permeability resulted from the dominance of nanoscale pores. Gas huff-n-puff enhanced oil recovery (EOR) has been proved to be a promising approach by both laboratory and field case studies. However, considering that the deviated properties of confined fluids are not well incorporated, erroneous predictions and large uncertainties exist for the compositional simulation of unconventional reservoirs. The objective of this chapter is to propose an improved compositional simulation model tailored for gas huff-n-puff in unconventional reservoirs with well-incorporated nanoscale confinement. In this chapter, more accurate critical property shift correlations proposed in Chapter 3 are applied to reflect the nanoscale confinement. Field case studies based on Eagle Ford shale are performed to investigate the effect of nanoscale confinement on both the primary and the EOR production in unconventional reservoirs.

6.1 Reflection of Nanoscale Confinement

Critical properties shift, as one of the most typical and significant aspects of the confined fluid phase behavior deviation, has been investigated in numerous experimental and simulation works (Zarragoicoechea and Kuz, 2004; Yang et al., 2019a; Qiu et al., 2019). Since the shift of critical properties are the result of nanoscale confinement, it can be used to reflect the nanoscale confinement resulted from strong molecule-wall interaction and geometric constraints (Yu et al., 2019, Yang and Li, 2020).

6.1.1 Critical properties shift correlations

Considering that most of the current correlations to predict the critical properties shift are not accurate enough (Yang et al., 2019), new correlations are established by curve fitting the critical properties shift (ΔT^*, ΔP^*) data from experimental and molecular simulation results with dimensionless pore size r_p/σ_{LJ} as shown in Chapter 3:

$$\Delta T^* = 1.7391 \times (r_p / \sigma_{LJ})^{-1.379} \tag{6.1}$$

$$\Delta P^* = 1.1892 \times (r_p / \sigma_{LJ})^{-0.807} \tag{6.2}$$

where ΔT^*, ΔP^* are the critical temperature shift and the critical pressure shift of the confined fluids, r_p and σ_{LJ} are the pore size and the molecular size, respectively. The newly proposed critical shift correlations are validated capable of predicting both confined critical temperature and critical pressure shift with higher accuracy down to 2 nm (Yang and Li, 2020).

6.1.2 Nanoscale confinement reflection

To reflect the nanoscale confinement with critical property shift, an Eagle Ford oil sample collected from Yu et al. (2019) is adopted to conduct the analysis. Tables 5.5 and 5.6 demonstrate the properties of 6 pseudo components and the binary interaction parameters, respectively. Table 6.1 summaries the shifted critical properties at different pore sizes. The modified PR EOS proposed in Chapter 3 is used to compute the phase diagrams of this oil sample at different pore sizes, as shown in Figure 6.1.

$$P = \frac{RT}{v - \beta b} - \frac{a\beta[1 - 1.7391 \times (r_p / \sigma_{LJ})^{-1.379}]}{v(v + \beta b) + \beta b(v - \beta b)} \tag{6.3a}$$

$$\beta = \frac{1 - \Delta T^*}{1 - \Delta P^*} = \frac{1 - 1.7391 \times (r_p / \sigma_{LJ})^{-1.379}}{1 - 1.1892 \times (r_p / \sigma_{LJ})^{-0.807}} \tag{6.3b}$$

where R is the universal gas constant; v is the molar volume; P and T are pressure and temperature, respectively; a and b are constants describing attractive force and the covolume, respectively. β is the covolume ratio between the confined fluid and the bulk fluid.

Table 6.1: Critical properties of Eagle Ford oil at different pore sizes

Components	50 nm		10 nm		5 nm		3 nm	
	P_{cc}, atm	T_{cc}, K	P_{cc}, atm	T_{cc}, K	P_{cc}, atm	T_{cc}, K	P_{cc}, atm	T_{cc}, K
CO_2	71.07	303.54	66.45	298.10	61.68	288.34	56.01	272.12
N_2	32.72	125.94	30.66	123.79	28.52	119.93	25.99	113.51
C_1	44.32	190.18	41.43	186.77	38.46	180.64	34.92	170.46
C_2-C_5	35.48	273.96	32.77	267.52	29.97	255.97	26.64	236.77
C_6-C_{10}	24.20	436.83	21.86	421.70	19.45	394.51	16.58	349.35
C_{11+}	16.77	735.62	14.70	697.34	12.56	628.58	10.01	514.35

Note: molecular size of each component is calculated by $\sigma_{LJ} = 0.244\sqrt[3]{T_c / P_c}$

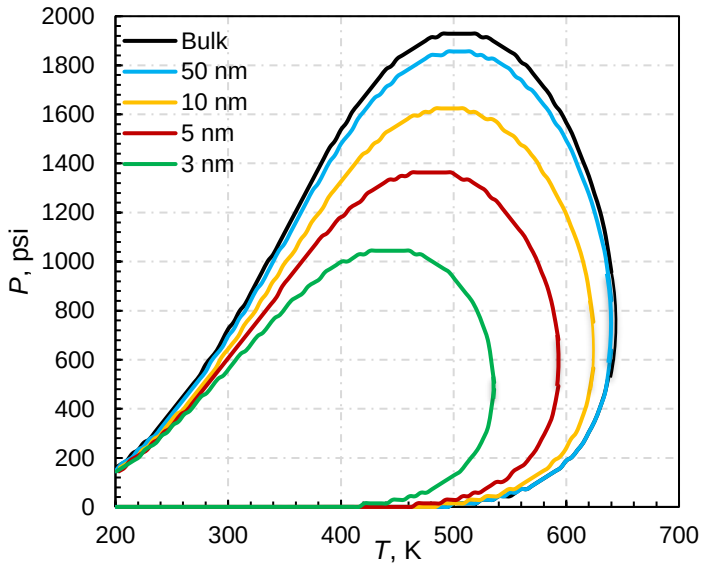

Figure 6.1: Phase diagrams of Eagle Ford sample at various pore sizes

As demonstrated in Figure 6.1, consideration of the critical properties shift results in the overall shrinkage of the two-phase diagram. The shrinkage rate increases with the decreasing pore size, reflecting the increasing effect of geometric constraints and molecule-wall interaction. The favorable phase behavior shift of confined reservoir fluids causes a late evolution of solution gas, providing a wider operation window, a higher liquid saturation and therefore higher oil production.

The quantitative impact of nanoscale confinement on production and the ultimate recovery can be predicted by the compositional simulation approach.

6.2 Compositional Simulation

The GEM simulator has been well-applied for the compositional simulation of unconventional reservoirs with multiple hydraulic fractures and complex fluid behavior (Rubin, 2010; Sanaei et al., 2014). An improved compositional simulation model tailored for gas huff-n-puff in unconventional reservoirs is established in this section. Nanoscale confinement characterized by the modified PR EOS is well incorporated into the compositional simulation model. Consequently, natural gas huff-n-puff process in the Eagle Ford shale is simulated to investigate its influence on the primary production and the ultimate recovery.

6.2.1 Confined fluid properties

The deviated PVT data generated using the modified PR EOS is well incorporated into the compositional simulation model to reflect the nanoscale confinement. The critical properties shift and the bubble-point pressure suppression of the Eagle Ford oil sample with nanopore size are demonstrated in Figure 6.2.

Figure 6.2 (a) demonstrates the shift of critical properties of the Eagle Ford oil sample. The suppression rate decreases with increasing pore size for both critical temperature and critical pressure. The suppression rate of critical pressure is generally higher than that of the critical temperature. Moreover, the effect of nanoscale confinement on critical temperature becomes negligible at pore size above 50 nm, while for critical pressure, the threshold value is 100 nm. Figure 6.2 (b) illustrates the suppression of bubble-point pressure with pore size. Like the critical

property shift, the suppression rate also decreases with increasing pore size. At 100 nm and above, the effect of nanoscale confinement can be neglected, where the properties of bulk fluids can be applied for compositional simulation.

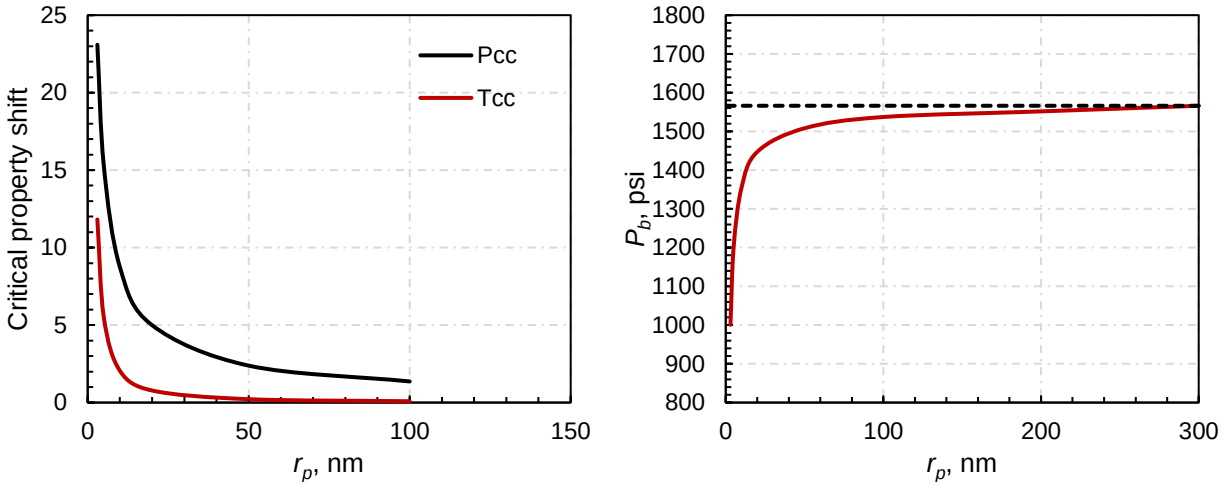

(a) Critical properties shift (b) Bubble-point pressure

Figure 6.2: Property deviation of Eagle Ford oil sample at various pore sizes

6.2.2 Field case model

With the nanoscale confinement well incorporated, the field case model can be established to investigate the impact of both nanoscale confinement and gas huff-n-puff on the production and the ultimate recovery of unconventional reservoirs. The model is established based on the field case wells in Eagle Ford shale (Wang and Yu, 2019, Yu et al., 2019). It is a homogeneous model built in the GEM simulator with dual permeability. The dimensions of this model are 5450×1290×100 ft in *x*, *y*, and *z* direction, respectively. The grid sizes are 50×30×20 in *x*, *y*, and *z* direction, respectively. Single well with a length of 4550 ft and multi-stage fractures is located in the middle of the reservoir, as demonstrated in Figure 6.3.

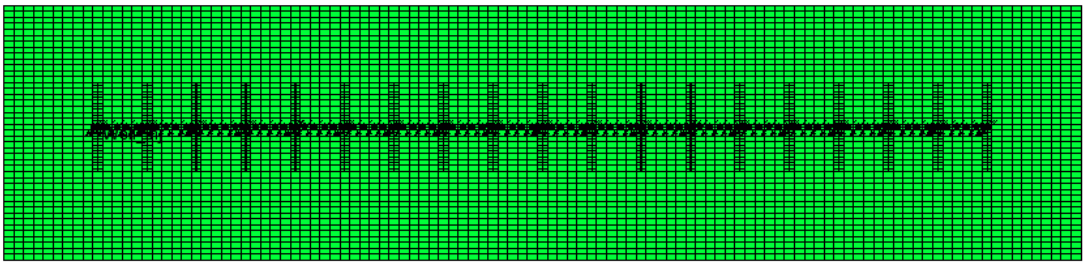

Figure 6.3: Field case model of Eagle Ford shale

Reservoir properties

The reservoir properties of the field case model are based on the actual Eagle Ford shale formations (Wang and Yu, 2019; Yu et al., 2019). The reservoir properties and the parameters of the fractures are summarized and listed in Table 6.2.

Table 6.2: Reservoir properties and fracture parameters of the field case model

Properties	Value	Unit
Depth at top of reservoir	10000	ft
Reservoir thickness	100	ft
Initial reservoir pressure	8000	psi
Reservoir temperature	270	°F
Initial water saturation	0.25	fraction
Rock compressibility	1×10^{-6}	-
Matrix porosity	0.12	fraction
Matrix permeability	5×10^{-4}	mD
Natural fracture porosity	0.002	fraction
Natural fracture permeability	0.003	mD
Natural fracture x spacing	50	ft
Natural fracture y spacing	50	ft
Natural fracture z spacing	0	ft
Horizontal well length	4550	ft
Hydraulic fracture number	19	stage
Hydraulic fracture half length	210	ft
Hydraulic fracture spacing	250	ft
Hydraulic fracture conductivity	200	mD.ft

Reservoir fluid

The reservoir fluid in this work is represented by an Eagle Ford oil sample with six pseudo-components that is taken from Yu et al. (2019). The fluid composition and the binary interaction

parameters between different components are listed in Tables 5.5 and 5.6. These data are also the basis for calculating the confined fluid properties of the oil sample by using the modified PR EOS model (Yang and Li, 2020).

Relative permeability

As an important input parameter for the compositional simulation of unconventional reservoirs, relative permeability has a significant impact on the simulation results. Considering the drastic difficulty and cost of obtaining the accurate relative permeability curves in unconventional reservoirs. The relative permeability curves of Yu et al. (2019) are slightly modified and fit to the Corey-Brooks equations to facilitate its input into the GEM model for the Eagle Ford well, as demonstrated in Table 6.3 and Figure 6.4.

Table 6.3: Corey-Brooks constants for relative permeability curves

Parameter	Value
Connate water saturation	0.25
Critical water saturation	0.25
Residual oil saturation	0.1
Residual gas saturation	0.04
Critical gas saturation	0.07
Endpoint water relative permeability k_{rw}	0.53
Endpoint oil relative permeability k_{ro}	1
Endpoint gas relative permeability k_{rog}	1
Endpoint liquid relative permeability k_{rg}	1
Exponent for calculating k_{rw}	1.2
Exponent for calculating k_{row}	2.8
Exponent for calculating k_{rog}	5.0
Exponent for calculating k_{rg}	3.0

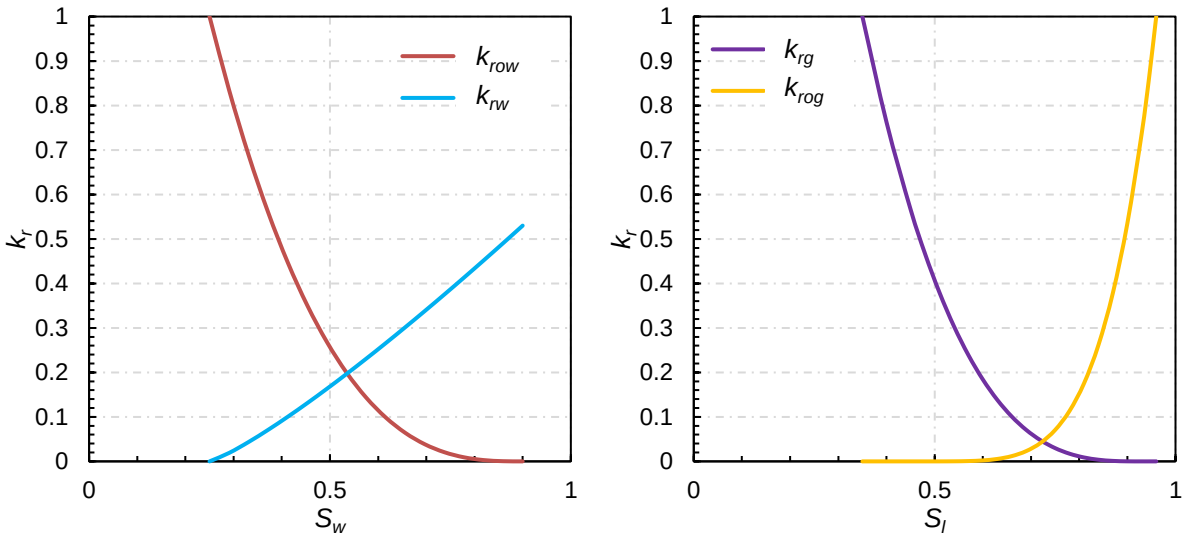

(a) Water-oil relative permeability (b) Liquid-gas relative permeability

Figure 6.4: Relative permeability curves for the reservoir model

Gas huff-n-puff

Methane is chosen as the injected gas to perform the field case simulation. As for the huff-n-puff, the operation parameters are selected according to the pilot tests and some other simulation works in Eagle Ford formations, as shown in Table 6.4. In this work, the well is primarily produced for three years before gas injection. For each huff-n-puff cycle, 3-month gas injection is followed by a 1-month shut in as the soaking time, and then the well is put back into production for 8-month before the next cycle starts. In total, 5 cycles of gas huff-n-puff are simulated, followed by another 5 years of production. Overall, the simulation time is 13 years. Moreover, the constant gas injection rate is 1500 MSCF and the maximum injection pressure is 8000 psi. The minimum bottom hole pressure for the production well is set at 2000 psi and the maximum production rate is 1200 bbl/day.

After the field case model is well-established with incorporation of the nanoscale confinement, the compositional simulation of gas huff-n-puff is performed to investigate the influence on the production and the ultimate recovery.

Table 6.4: Parameter settings for gas huff-n-puff

References	Injected gas	Primary production	Injection time	Soaking time	Production time	Injection rate
Orozco et al., 2018	Natural gas	3 years	100 days	-	100 days	1500 MSCF
Yu et al., 2019	CO_2	583 days	90 days	90 days	720 days	5000 MSCF
Wang and Yu, 2019	Natural gas	5 years	3 months	1 month	6 months	1300 MSCF
Wang et al., 2019	Natural gas	3 years	1 month	0.5 month	2.5 months	5000 MSCF

6.3 Results and Discussion

The compositional simulation of an Eagle Ford well is conducted with consideration of the nanoscale confinement. Figure 6.5 demonstrated the effect of nanoscale confinement under different pore sizes. As can be seen, nanoscale confinement results in the increased cumulative oil production due to the suppressed bubble-point pressure, which delays the evolution of solution gas, providing a wider oil production window.

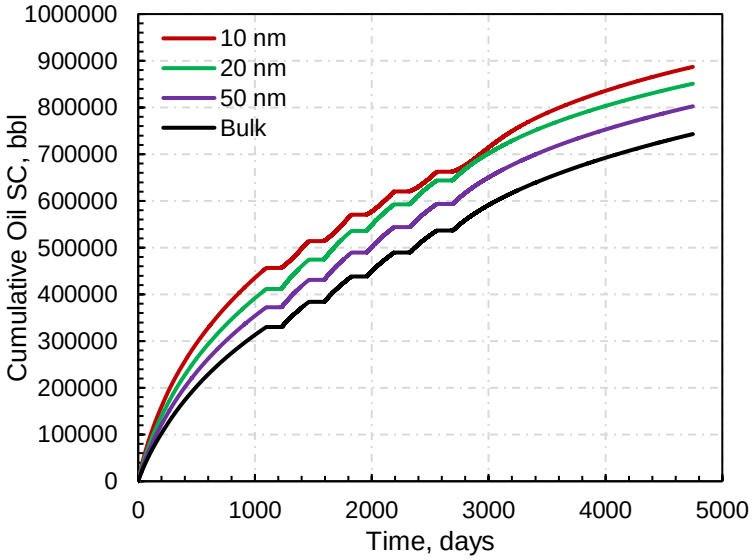

Figure 6.5: Effect of nanoscale confinement on gas huff-n-puff production

To investigate the performance of gas huff-n-puff in Eagle Ford shale under the impact of nanoscale confinement, a general case with pore size of 20 nm is simulated and illustrated in Figure

6.6. The compositional simulation of Bakken shale with CO_2 injection is also demonstrated for comparison (Yang and Li, 2020).

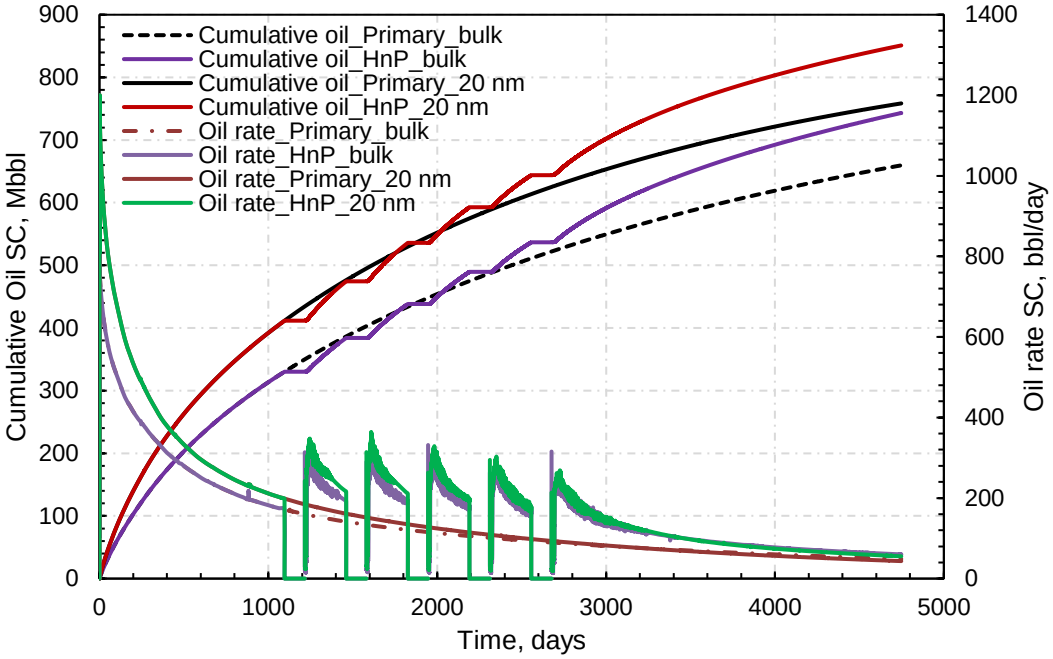

Figure 6.6: Effect of gas huff-n-puff and nanoscale confinement on Eagle Ford oil production

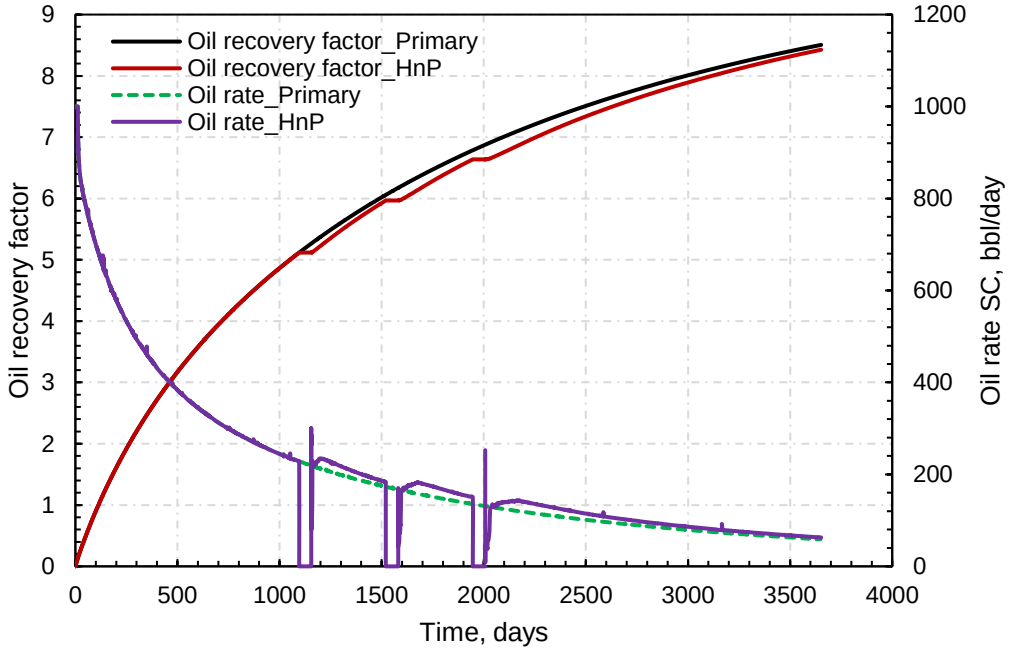

Figure 6.7: Effect of gas huff-n-puff on Bakken oil production (Yang and Li, 2020)

The simulation results in Figure 6.6 demonstrate that the CH_4 huff-n-puff is an effective EOR method for Eagle Ford shale and nanoscale confinement has significant impact on both the primary and the EOR production of unconventional reservoirs. Due to the extremely low matrix permeability, the primary oil rate decreases drastically with time. As shown in Figure 6.6, the oil flow rate drops by 80 % before gas injection, validating the necessity of the enhanced oil recovery. After gas injection, the oil rate increases sharply. Despite the production loss during injection and soaking time, the cumulative oil production of gas huff-n-puff still shows a satisfactory increase compared with the primary production. The recovery factor at the end of the 13 years production is increased by 12.20% after gas huff-n-puff. On the contrary, the simulation of CO_2 huff-n-puff in Bakken shale demonstrated in Figure 6.7 achieves unsatisfactory enhanced oil recovery performance because the limited incremental oil cannot even offset the production lost during the injection and soaking time (Yang and Li, 2020). Hence, it is well proved that the eligibility of gas huff-n-puff EOR is highly dependent on the composition of reservoir fluids, injected gas, and the properties of reservoir formations.

6.4 Summary

This chapter establishes an improved compositional simulation model tailored for the gas huff-n-puff in unconventional reservoirs with well-incorporated nanoscale confinement. Because of the extremely low matrix permeability, the primary oil rate decreases by 80% before the gas huff-n-puff, validating the necessity of the EOR approach. Compositional simulation results demonstrated that the nanoscale confinement has significant impact on both the primary production and the ultimate recovery of unconventional reservoirs. Specifically, nanoscale confinement results in the increased cumulative oil production due to the suppressed bubble-point

pressure. The oil recovery factor of Eagle Ford well is increased by 12.20% at the end of the 13 years production after CH_4 huff-n-puff. The gas huff-n-puff EOR performance is highly dependent on the composition of reservoir fluids and properties of reservoir formations.

Chapter 7: Conclusions

This dissertation developed reliable theoretical models to characterize the confined fluid phase behavior within nanopores and investigated its influence on the unconventional hydrocarbon recovery. The following conclusions can be made:

1. A modified PR EOS with incorporation of both molecule-wall interaction and geometric constraints has been proposed to characterize the confined fluid phase behavior at various nanopore sizes. Molecule-wall interaction can demonstrate as repulsion- or attraction-dominant under different pore sizes, having a similar variation trend with the typical Lennard-Jones potential. With consideration of the geometric constraints, confined covolume is generally greater than the bulk covolume and the variation with dimensionless pore size is not monotonic. Confinement effect imposes an overall shrinkage to both the *P-T* diagram and the two-phase region in a ternary diagram of CO_2/hydrocarbon systems, benefiting the miscible enhanced oil recovery (EOR) in unconventional reservoirs by increasing the possibility of achieving the first contact miscibility.

2. A modified Kelvin equation with consideration of the real gas effect, the pore size effect on surface tension, the multilayer adsorption, and the molecule-wall interaction potential has been proposed to investigate the capillary condensation phenomenon of both single- and multicomponent fluids in nanopores. The proposed model is applicable to calculate the suppressed capillary condensation pressure of confined fluids in nanopores with the overall relative deviations of 7.65% and 6.52% for single- and multicomponent fluids, respectively. The molecule-wall interaction potential has the most significant contribution to the modification, while the pore size effect on surface tension has the least contribution among all the incorporated factors.

3. Nanoscale confinement results in the drastic suppression of the minimum miscibility pressure (MMP) of confined fluids and the suppression rate increases with decreasing pore size.

For 100% CO_2 injection, the MMP suppression rate of Bakken oil and Eagle Ford oil at 10 nm are 6.22% and 13.01%, respectively. The drastic suppression of MMP is highly favorable for the miscible gas injection EOR in unconventional reservoirs. The mix of CH_4 into CO_2 can either decrease or increase the MMP values of unconventional reservoir fluids depending on the compositions of the reservoir fluid and the injected gases. Comparing to the vanishing interfacial tension (VIT) simulation, the multiple mixing cell (MMC) approach has been recognized to be an accurate theoretical method to calculate the confined MMP values in unconventional reservoirs.

4. An improved compositional simulation model tailored for gas huff-n-puff in unconventional reservoirs has been established with well incorporated nanoscale confinement. Results demonstrated that nanoscale confinement has obvious influence on the production and the ultimate recovery of gas huff-n-puff in unconventional reservoirs. The oil recovery factor of Eagle Ford well is increased by 12.20% at the end of the 13 years production after CH_4 injection. The gas huff-n-puff EOR performance is highly dependent on the composition of reservoir fluids and properties of reservoir formations.

The results of this dissertation improved our understanding of the confined fluid phase behavior, which further provided reliable and practical instructions for the unconventional hydrocarbon recovery. In addition, it also shed light on the characterization of confined fluid systems which can potentially be applied in carbon storage, membrane separation and some other nanoscale disciplines.

References

Adekunle, O., & Hoffman, B. T. (2016). Experimental and analytical methods to determine minimum miscibility pressure (MMP) for Bakken formation crude oil. Journal of Petroleum Science and Engineering, 146, 170-182.

Adolphs, J. (2016). Thermodynamics and modeling of sorption isotherms. Chemie Ingenieur Technik, 88(3), 274-281.

Ahmadi, K., & Johns, R. T. (2011). Multiple-mixing-cell method for MMP calculations. SPE Journal, 16(04), 733-742.

Alcoutlabi, M., & McKenna, G. B. (2005). Effects of confinement on material behavior at the nanometre size scale. Journal of Physics: Condensed Matter, 17(15), R461.

Alfi, M., Banerjee, D., & Nasrabadi, H. (2016). Effect of confinement on the dynamic contact angle of hydrocarbons. Energy & Fuels, 30(11), 8962-8967.

Alfi, M., Nasrabadi, H., & Banerjee, D. (2016). Experimental investigation of confinement effect on phase behavior of hexane, heptane and octane using lab-on-a-chip technology. Fluid Phase Equilibria, 423, 25-33.

Alharthy, N. S., Nguyen, T., Teklu, T., Kazemi, H., & Graves, R. (2013). Multiphase compositional modeling in small-scale pores of unconventional shale reservoirs. In SPE Annual Technical Conference and Exhibition. Society of Petroleum Engineers.

Alharthy, N., Teklu, T. W., Kazemi, H., Graves, R. M., Hawthorne, S. B., Braunberger, J., & Kurtoglu, B. (2018). Enhanced oil recovery in liquid-rich shale reservoirs: laboratory to field. SPE Reservoir Evaluation & Engineering, 21(01), 137-159.

Allen, M. P. (2004). Introduction to molecular dynamics simulation. Computational soft matter: from synthetic polymers to proteins, 23(1), 1-28.

Ambrose, R. J., Hartman, R. C., Diaz-Campos, M., Akkutlu, I. Y., & Sondergeld, C. H. (2012). Shale gas-in-place calculations part I: new pore-scale considerations. SPE Journal, 17(01), 219-229.

Arogundade, O., & Sohrabi, M. (2012). A review of recent developments and challenges in shale gas recovery. In SPE Saudi Arabia Section Technical Symposium and Exhibition. Society of Petroleum Engineers.

Bao, B., Feng, J., Qiu, J., & Zhao, S. (2020). Direct measurement of minimum miscibility pressure of decane and CO_2 in nanoconfined channels. ACS Omega.

Bao, B., Riordon, J., Mostowfi, F., & Sinton, D. (2017). Microfluidic and nanofluidic phase behaviour characterization for industrial CO_2, oil and gas. Lab on a Chip, 17(16), 2740-2759.

Barsotti, E., Tan, S. P., Saraji, S., Piri, M., & Chen, J. H. (2016). A review on capillary condensation in nanoporous media: Implications for hydrocarbon recovery from tight reservoirs. Fuel, 184, 344-361.

Barsotti, E., Tan, S. P., Piri, M., & Chen, J. H. (2018). Phenomenological study of confined criticality: Insights from the capillary condensation of propane, n-butane, and n-pentane in nanopores. Langmuir, 34(15), 4473-4483.

Barsotti, E., Saraji, S., Tan, S. P., & Piri, M. (2018). Capillary condensation of binary and ternary mixtures of n-Pentane–Isopentane–CO_2 in nanopores: an experimental study on the effects of composition and equilibrium. Langmuir, 34(5), 1967-1980.

Bernardo, P., Drioli, E., & Golemme, G. (2009). Membrane gas separation: a review/state of the art. Industrial & engineering chemistry research, 48(10), 4638-4663.

Boelens, A. M., & Tchelepi, H. A. (2020). Minkowski functionals for phase behavior under confinement. arXiv preprint arXiv:2004.01344.

Brás, A. R., Fonseca, I. M., Dionísio, M., Schönhals, A., Affouard, F., & Correia, N. T. (2014). Influence of nanoscale confinement on the molecular mobility of ibuprofen. The Journal of Physical Chemistry C, 118(25), 13857-13868.

Broekhoff, J. C. P., & De Boer, J. H. (1967). Studies on pore systems in catalysts: IX. Calculation of pore distributions from the adsorption branch of nitrogen sorption isotherms in the case of open cylindrical pores A. Fundamental equations. Journal of Catalysis, 9(1), 8-14.

Brunauer, S., Emmett, P. H., & Teller, E. (1938). Adsorption of gases in multimolecular layers. Journal of the American chemical society, 60(2), 309-319.

Burgess, C. G., Everett, D. H., & Nuttall, S. (1990). Adsorption of carbon dioxide and xenon by porous glass over a wide range of temperature and pressure-applicability of the Langmuir case VI equation. Langmuir, 6(12), 1734-1738.

Cao, J., Liang, Y., Masuda, Y., Koga, H., Tanaka, H., Tamura, K., ... & Matsuoka, T. (2019). Molecular simulation of CH_4 adsorption behavior in slit nanopores: Verification of simulation methods and models. AIChE Journal, 65(11), e16733.

Chai, D., Yang, G., Fan, Z., & Li, X. (2019). Gas transport in shale matrix coupling multilayer adsorption and pore confinement effect. Chemical Engineering Journal, 370, 1534-1549.

Chen, J. H., Zhang, J., Jin, G., Quinn, T., Frost, E., & Chen, J. (2012). Capillary condensation and NMR relaxation time in unconventional shale hydrocarbon resources. In SPWLA 53rd Annual Logging Symposium. Society of Petrophysicists and Well-Log Analysts.

Chen, J. H., Mehmani, A., Li, B., Georgi, D., & Jin, G. (2013). Estimation of total hydrocarbon in the presence of capillary condensation for unconventional shale reservoirs. In SPE Middle East oil and gas show and conference. Society of Petroleum Engineers.

Cho, H., Bartl, M. H., & Deo, M. (2017). Bubble point measurements of hydrocarbon mixtures in mesoporous media. Energy & Fuels, 31(4), 3436-3444.

Christiansen, R. L., & Haines, H. K. (1987). Rapid measurement of minimum miscibility pressure with the rising-bubble apparatus. SPE Reservoir Engineering, 2(04), 523-527.

Cipolla, C. L., Lolon, E. P., Erdle, J. C., & Rubin, B. (2010). Reservoir modeling in shale-gas reservoirs. SPE reservoir evaluation & engineering, 13(04), 638-653.

Clarkson, C. R., Solano, N., Bustin, R. M., Bustin, A. M. M., Chalmers, G. R. L., He, L., ... & Blach, T. P. (2013). Pore structure characterization of North American shale gas reservoirs using USANS/SANS, gas adsorption, and mercury intrusion. Fuel, 103, 606-616.

Coasne, B., Hung, F. R., Pellenq, R. J. M., Siperstein, F. R., & Gubbins, K. E. (2006). Adsorption of simple gases in MCM-41 materials: the role of surface roughness. Langmuir, 22(1), 194-202.

Cohen, A. J., Mori-Sánchez, P., & Yang, W. (2012). Challenges for density functional theory. Chemical reviews, 112(1), 289-320.

Cui, X., Yang, E., Song, K., Huang, J., Killough, J., Dong, C., ... & Wang, K. (2018). Phase equilibrium of hydrocarbons confined in nanopores from a modified Peng-Robinson equation of state. In SPE Annual Technical Conference and Exhibition. Society of Petroleum Engineers.

Danesh, A. S., Dandekar, A. Y., Todd, A. C., & Sarkar, R. (1991). A modified scaling law and parachor method approach for improved prediction of interfacial tension of gas-condensate systems. In SPE annual technical conference and exhibition. Society of Petroleum Engineers.

Derouane, E. G. (2007). On the physical state of molecules in microporous solids. Microporous and mesoporous materials, 104(1-3), 46-51.

Derycke, I., Vigneron, J. P., Lambin, P., Lucas, A. A., & Derouane, E. G. (1991). Physisorption in confined geometry. The Journal of chemical physics, 94(6), 4620-4627.

Didar, B. R., & Akkutlu, I. Y. (2013). Pore-size dependence of fluid phase behavior and properties in organic-rich shale reservoirs. In SPE international symposium on oilfield chemistry. Society of Petroleum Engineers.

Dillmann, O., Janke, W., Müller, M., & Binder, K. (2001). A Monte Carlo test of the Fisher–Nakanishi–Scaling theory for the capillary condensation critical point. The Journal of Chemical Physics, 114(13), 5853-5862.

Dong, X., Liu, H., Hou, J., Wu, K., & Chen, Z. (2016). Phase equilibria of confined fluids in nanopores of tight and shale rocks considering the effect of capillary pressure and adsorption film. Industrial & Engineering Chemistry Research, 55(3), 798-811.

Eberle, A. P., King, H. E., Ravikovitch, P. I., Walters, C. C., Rother, G., & Wesolowski, D. J. (2016). Direct measure of the dense methane phase in gas shale organic porosity by neutron scattering. Energy & Fuels, 30(11), 9022-9027.

Economou, I. G. (2008). Molecular simulation of phase equilibria for industrial applications. ChemInform, 39(49).

Findenegg, G. H., Groβ, S., & Michalski, T. (1994). Pore condensation in controlled-pore glass. An experimental test of the Saam-Cole theory. In Studies in Surface Science and Catalysis (Vol. 87, pp. 71-80). Elsevier.

Findenegg, G. H., Jähnert, S., Akcakayiran, D., & Schreiber, A. (2008). Freezing and melting of water confined in silica nanopores. Chem Phys Chem, 9(18), 2651-2659.

Firincioglu, T. (2013). Bubble point suppression in unconventional liquids rich reservoirs and its impact on oil production (Doctoral dissertation, Colorado School of Mines. Arthur Lakes Library).

Fisher, M. E., & Nakanishi, H. (1981). Scaling theory for the criticality of fluids between plates. The Journal of Chemical Physics, 75(12), 5857-5863.

Fréchette, L. G., Jacobson, S. A., Breuer, K. S., Ehrich, F. F., Ghodssi, R., Khanna, R., ... & Epstein, A. H. (2005). High-speed microfabricated silicon turbomachinery and fluid film bearings. Journal of Microelectromechanical Systems, 14(1), 141-152.

Gamadi, T. D., Sheng, J. J., Soliman, M. Y., Menouar, H., Watson, M. C., & Emadibaladehi, H. (2014). An experimental study of cyclic CO_2 injection to improve shale oil recovery. In SPE improved oil recovery symposium. Society of Petroleum Engineers.

Gavette, J. V., Zhang, K. D., Ajami, D., & Rebek, J. (2014). Folded alkyl chains in water-soluble capsules and cavitands. Organic & Biomolecular Chemistry, 12(34), 6561-6563.

Gelb, L. D., Gubbins, K. E., Radhakrishnan, R., & Sliwinska-Bartkowiak, M. (1999). Phase separation in confined systems. Reports on Progress in Physics, 62(12), 1573.

Giovambattista, N., Rossky, P. J., & Debenedetti, P. G. (2006). Effect of pressure on the phase behavior and structure of water confined between nanoscale hydrophobic and hydrophilic plates. Physical Review E, 73(4), 041604.

Glachant, A., Jaubert, M., Bienfait, M., & Boato, G. (1982). Monolayer adsorption of Kr and Xe on metal surfaces: Structures and uniaxial phase transitions on Cu (110). Surface Science, 115(1), 219-235.

Goel, H., Ling, S., Ellis, B. N., Taconi, A., Slater, B., & Rai, N. (2018). Predicting vapor liquid equilibria using density functional theory: A case study of argon. The Journal of chemical physics, 148(22), 224501.

Goertz, M. P., Houston, J. E., & Zhu, X. Y. (2007). Hydrophilicity and the viscosity of interfacial water. Langmuir, 23(10), 5491-5497.

Gogotsi, Y., Libera, J. A., Güvenç-Yazicioglu, A., & Megaridis, C. M. (2001). In situ multiphase fluid experiments in hydrothermal carbon nanotubes. Applied physics letters, 79(7), 1021-1023.

González, M. A. (2011). Force fields and molecular dynamics simulations. École thématique de la Société Française de la Neutronique, 12, 169-200.

Gregg, S. J., Sing, K. S. W., & Salzberg, H. W. (1967). Adsorption surface area and porosity. Journal of the electrochemical society, 114(11), 279C.

Grosman, A., & Ortega, C. (2005). Nature of capillary condensation and evaporation processes in ordered porous materials. Langmuir, 21(23), 10515-10521.

Guo, C., Xu, J., Wu, K., Wei, M., & Liu, S. (2015). Study on gas flow through nano pores of shale gas reservoirs. Fuel, 143, 107-117.

Haider, B. A., & Aziz, K. (2017). Impact of capillary pressure and critical property shift due to confinement on hydrocarbon production in shale reservoirs. In SPE Reservoir Simulation Conference. Society of Petroleum Engineers.

Hamada, Y., Koga, K., & Tanaka, H. (2007). Phase equilibria and interfacial tension of fluids confined in narrow pores. The Journal of chemical physics, 127(8), 084908.

Han, S., Choi, M. Y., Kumar, P., & Stanley, H. E. (2010). Phase transitions in confined water nanofilms. Nature Physics, 6(9), 685-689.

Hawthorne, S. B., Gorecki, C. D., Sorensen, J. A., Steadman, E. N., Harju, J. A., & Melzer, S. (2013). Hydrocarbon mobilization mechanisms from upper, middle, and lower Bakken reservoir rocks exposed to CO_2. In SPE Unconventional Resources Conference Canada. Society of Petroleum Engineers.

Hawthorne, S. B., Miller, D. J., Jin, L., & Gorecki, C. D. (2016). Rapid and simple capillary-rise/vanishing interfacial tension method to determine crude oil minimum miscibility pressure: pure and mixed CO_2, methane, and ethane. Energy & Fuels, 30(8), 6365-6372.

Hoang, H., & Galliero, G. (2012). Local viscosity of a fluid confined in a narrow pore. Physical Review E, 86(2), 021202.

Hoffman, B. T. (2018). Huff-N-Puff gas injection pilot projects in the eagle ford. In SPE Canada Unconventional Resources Conference. Society of Petroleum Engineers.

Horikawa, T., Do, D. D., & Nicholson, D. (2011). Capillary condensation of adsorbates in porous materials. Advances in colloid and interface science, 169(1), 40-58.

Hoffman, B. T. (2018). Huff-N-Puff gas injection pilot projects in the eagle ford. In SPE Canada Unconventional Resources Conference. Society of Petroleum Engineers.

Ingebrigtsen, T. S., & Dyre, J. C. (2014). The impact range for smooth wall–liquid interactions in nanoconfined liquids. Soft Matter, 10(24), 4324-4331.

Israelachvili, J. N. (2011). Intermolecular and surface forces. Academic press.

Jackson, C. L., & McKenna, G. B. (1990). The melting behavior of organic materials confined in porous solids. The Journal of Chemical Physics, 93(12), 9002-9011.

Jackson, C. L., & McKenna, G. B. (1991). The glass transition of organic liquids confined to small pores. Journal of Non-Crystalline Solids, 131, 221-224.

Jackson, C. L., & McKenna, G. B. (1996). Vitrification and crystallization of organic liquids confined to nanoscale pores. Chemistry of Materials, 8(8), 2128-2137.

Jana, S., Singh, J. K., & Kwak, S. K. (2009). Vapor-liquid critical and interfacial properties of square-well fluids in slit pores. The Journal of chemical physics, 130(21), 214707.

Jatukaran, A., Zhong, J., Persad, A. H., Xu, Y., Mostowfi, F., & Sinton, D. (2018). Direct visualization of evaporation in a two-dimensional nanoporous model for unconventional natural gas. ACS Applied Nano Materials, 1(3), 1332-1338.

Javadpour, F. (2009). Nanopores and apparent permeability of gas flow in mudrocks (shales and

siltstone). Journal of Canadian Petroleum Technology, 48(08), 16-21.

Jiang, J., Sandler, S. I., & Smit, B. (2004). Capillary phase transitions of n-alkanes in a carbon nanotube. Nano Letters, 4(2), 241-244.

Jimenez-Gallegos, R., Galicia-Luna, L. A., & Elizalde-Solis, O. (2006). Experimental vapor− liquid equilibria for the carbon dioxide+ octane and carbon dioxide+ decane systems. Journal of Chemical & Engineering Data, 51(5), 1624-1628.

Jin, Z., & Firoozabadi, A. (2016). Thermodynamic modeling of phase behavior in shale media. SPE Journal, 21(01), 190-207.

Jin, B., & Nasrabadi, H. (2018). Phase behavior in shale organic/inorganic nanopores from molecular simulation. SPE Reservoir Evaluation & Engineering, 21(03), 626-637.

Jin, Z. (2018). Bubble/dew point and hysteresis of hydrocarbons in nanopores from molecular perspective. Fluid Phase Equilibria, 458, 177-185.

Jin, B., & Nasrabadi, H. (2016). Phase behavior of multicomponent hydrocarbon systems in nano-pores using gauge-GCMC molecular simulation. Fluid Phase Equilibria, 425, 324-334.

Koga, K., Gao, G. T., Tanaka, H., & Zeng, X. C. (2001). Formation of ordered ice nanotubes inside carbon nanotubes. Nature, 412(6849), 802-805.

Kontogeorgis, G. M., & Gani, R. (Eds.). (2004). Computer aided property estimation for process and product design: computers aided chemical engineering. Elsevier.

Kremer, F., Huwe, A., Schönhals, A., & Różański, S. A. (2003). Molecular dynamics in confining space. In Broadband Dielectric Spectroscopy (pp. 171-224). Springer, Berlin, Heidelberg.

Kruk, M., & Jaroniec, M. (2000). Accurate method for calculating mesopore size distributions from argon adsorption data at 87 K developed using model MCM-41 materials. Chemistry of Materials, 12(1), 222-230.

Kuila, U., & Prasad, M. (2013). Specific surface area and pore-size distribution in clays and shales. Geophysical Prospecting, 61(Rock Physics for Reservoir Exploration, Characterisation and Monitoring), 341-362.

Kurtoglu, B., & Kazemi, H. (2012). Evaluation of Bakken performance using coreflooding, well testing, and reservoir simulation. In SPE Annual Technical Conference and Exhibition. Society of Petroleum Engineers.

Kurtoglu, B., Ramirez, B., & Kazemi, H. (2013). Modeling production performance of an abnormally high pressure unconventional shale reservoir. In Unconventional Resources Technology Conference (pp. 69-78). Society of Exploration Geophysicists, American Association of Petroleum Geologists, Society of Petroleum Engineers.

Laitinen, R., Löbmann, K., Strachan, C. J., Grohganz, H., & Rades, T. (2013). Emerging trends in the stabilization of amorphous drugs. International journal of pharmaceutics, 453(1), 65-79. Lennard-Jones, J. E. (1931). Cohesion. Proceedings of the Physical Society (1926-1948), 43(5), 461.

Leu, A. D., & Robinson, D. B. (1987). Equilibrium phase properties of the n-butane-carbon dioxide and isobutane-carbon dioxide binary systems. Journal of Chemical and Engineering Data, 32(4), 444-447.

Li, B., Mehmani, A., Chen, J., Georgi, D. T., & Jin, G. (2013). The condition of capillary condensation and its effects on adsorption isotherms of unconventional gas condensate reservoirs. In SPE Annual Technical Conference and Exhibition. Society of Petroleum Engineers.

Li, X., Yang, D., Zhang, X., Zhang, G., & Gao, J. (2016). Binary interaction parameters of CO_2− heavy-n-alkanes systems by using Peng–Robinson equation of state with modified alpha function. Fluid Phase Equilibria, 417, 77-86.

Li, X., Han, H., Yang, D., Liu, X., & Qin, J. (2017). Phase behavior of C_3H_8–CO_2–heavy oil systems in the presence of aqueous phase under reservoir conditions. Fuel, 209, 358-370.

Li, Z., & Firoozabadi, A. (2009). Interfacial tension of nonassociating pure substances and binary mixtures by density functional theory combined with Peng–Robinson equation of state. The Journal of chemical physics, 130(15), 154108.

Li, Z., Jin, Z., & Firoozabadi, A. (2014). Phase behavior and adsorption of pure substances and mixtures and characterization in nanopore structures by density functional theory. SPE Journal, 19(06), 1-096.

Liu, Y., Jin, Z., & Andy Li, H. (2017). Comparison of PR-EOS with capillary pressure model with engineering density functional theory on describing the phase behavior of confined hydrocarbons. In SPE Annual Technical Conference and Exhibition. Society of Petroleum Engineers.

Liu, Y., Li, H. A., & Okuno, R. (2018). Phase behavior of N_2/n-C_4H_{10} in a partially confined space derived from shale sample. Journal of Petroleum Science and Engineering, 160, 442-451.

Loucks, R. G., Reed, R. M., Ruppel, S. C., & Jarvie, D. M. (2009). Morphology, genesis, and distribution of nanometer-scale pores in siliceous mudstones of the Mississippian Barnett Shale. Journal of sedimentary research, 79(12), 848-861.

Lowry, E., & Piri, M. (2018). Effects of chemical and physical heterogeneity on confined phase behavior in nanopores. Microporous and Mesoporous Materials, 263, 53-61.

Maniwa, Y., Kataura, H., Abe, M., Suzuki, S., Achiba, Y., Kira, H., & Matsuda, K. (2002). Phase transition in confined water inside carbon nanotubes. Journal of the Physical Society of Japan, 71(12), 2863-2866.

Luo, S., Lutkenhaus, J. L., & Nasrabadi, H. (2016). Confinement-induced supercriticality and phase equilibria of hydrocarbons in nanopores. Langmuir, 32(44), 11506-11513.

Luo, S., Nasrabadi, H., & Lutkenhaus, J. L. (2016). Effect of confinement on the bubble points of hydrocarbons in nanoporous media. AIChE Journal, 62(5), 1772-1780.

Luo, S., Lutkenhaus, J. L., & Nasrabadi, H. (2018). Use of differential scanning calorimetry to study phase behavior of hydrocarbon mixtures in nano-scale porous media. Journal of Petroleum Science and Engineering, 163, 731-738.

Marx, R. (1985). Calorimetric studies of phase transitions in two-dimensional physisorbed films. Physics Reports, 125(1), 1-67.

Mashl, R. J., Joseph, S., Aluru, N. R., & Jakobsson, E. (2003). Anomalously immobilized water: a new water phase induced by confinement in nanotubes. Nano letters, 3(5), 589-592.

Millot, F., Larher, Y., & Tessier, C. (1982). Critical temperatures of two-dimensional condensation in monolayers of Ar, Kr, or Xe adsorbed on lamellar halides. The Journal of Chemical Physics, 76(6), 3327-3335.

Miyahara, M., Kanda, H., Yoshioka, T., & Okazaki, M. (2000). Modeling capillary condensation in cylindrical nanopores: a molecular dynamics study. Langmuir, 16(9), 4293-4299.

Morishige, K., Fujii, H., Uga, M., & Kinukawa, D. (1997). Capillary critical point of argon, nitrogen, oxygen, ethylene, and carbon dioxide in MCM-41. Langmuir, 13(13), 3494-3498.

Morishige, K., & Shikimi, M. (1998). Adsorption hysteresis and pore critical temperature in a single cylindrical pore. The Journal of chemical physics, 108(18), 7821-7824.

Morishige, K., & Nakamura, Y. (2004). Nature of adsorption and desorption branches in cylindrical pores. Langmuir, 20(11), 4503-4506.

Morishige, K., & Ito, M. (2002). Capillary condensation of nitrogen in MCM-41 and SBA-15. The Journal of Chemical Physics, 117(17), 8036-8041.

Morishige, K. (2016). Nature of adsorption hysteresis in cylindrical pores: effect of pore corrugation. The Journal of Physical Chemistry C, 120(39), 22508-22514.

Monson, P. A. (2012). Understanding adsorption/desorption hysteresis for fluids in mesoporous materials using simple molecular models and classical density functional theory. Microporous and Mesoporous Materials, 160, 47-66.

Mostowfi, F., Molla, S., & Tabeling, P. (2012). Determining phase diagrams of gas–liquid systems using a microfluidic PVT. Lab on a Chip, 12(21), 4381-4387.

Nagarajan, N., Gasem, K. A., & Robinson Jr, R. L. (1990). Equilibrium phase compositions, phase densities, and interfacial tensions for carbon dioxide+ hydrocarbon systems. 6. Carbon dioxide+ n-butane+ n-decane. Journal of Chemical and Engineering Data, 35(3), 228-231.

Nardon, Y., & Larher, Y. (1974). Critical temperatures of two-dimensional condensation of methane and rare gases on the cleavage face of layer-like halides. Surface Science, 42(1), 299-305.

Nikitin, E. D., & Popov, A. P. (2015). Vapour–liquid critical properties of components of biodiesel. 1. Methyl esters of n-alkanoic acids. Fuel, 153, 634-639.

Nojabaei, B., Johns, R. T., & Chu, L. (2013). Effect of capillary pressure on phase behavior in tight rocks and shales. SPE Reservoir Evaluation & Engineering, 16(03), 281-289.

Orozco, D., Fragoso, A., Selvan, K., Noble, G., & Aguilera, R. (2020). Eagle Ford huff ‘n’ puff gas-injection pilot: comparison of reservoir-simulation, material balance, and real performance of the pilot well. SPE Reservoir Evaluation & Engineering, 23(01), 247-260.

Orr Jr, F. M., & Jessen, K. (2007). An analysis of the vanishing interfacial tension technique for determination of minimum miscibility pressure. Fluid phase equilibria, 255(2), 99-109.

Ortiz-Young, D., Chiu, H. C., Kim, S., Voïtchovsky, K., & Riedo, E. (2013). The interplay between apparent viscosity and wettability in nanoconfined water. Nature communications, 4(1), 1-6.

Parsa, E., Yin, X., & Ozkan, E. (2015). Direct observation of the impact of nanopore confinement on petroleum gas condensation. In SPE Annual Technical Conference and Exhibition. Society of Petroleum Engineers.

Patrykiejew, A., Zientarski, T., & Binder, K. (1996). On melting of two-dimensional monolayer films. Acta Physica Polonica-Series A General Physics, 89(5), 735-742.

Peng, B., & Yu, Y. X. (2008). A density functional theory with a mean-field weight function: applications to surface tension, adsorption, and phase transition of a Lennard-Jones fluid in a slit-like pore. The Journal of Physical Chemistry B, 112(48), 15407-15416.

Pepper, A., Perry, S., & Heister, L. (2019). Saturation isn't what it used to be: Towards more realistic petroleum fluid saturations and produced fluid compositions in organic-rich unconventional reservoirs. Unconventional Resources Technology Conference (URTEC).

Pitakbunkate, T., Balbuena, P., Moridis, G. J., & Blasingame, T. A. (2014). Effect of confinement on PVT properties of hydrocarbons in shale reservoirs. In SPE Annual Technical Conference and Exhibition. Society of Petroleum Engineers.

Qian, K. K., & Bogner, R. H. (2012). Application of mesoporous silicon dioxide and silicate in oral amorphous drug delivery systems. Journal of pharmaceutical sciences, 101(2), 444-463.

Qiao, S. Z., Bhatia, S. K., & Zhao, X. S. (2003). Prediction of multilayer adsorption and capillary condensation phenomena in cylindrical mesopores. Microporous and mesoporous materials, 65(2-3), 287-298.

Qiu, X., Tan, S. P., Dejam, M., & Adidharma, H. (2018). Novel isochoric measurement of the onset of vapor–liquid phase transition using differential scanning calorimetry. Physical Chemistry Chemical Physics, 20(41), 26241-26248.

Qiu, X., Tan, S. P., Dejam, M., & Adidharma, H. (2019). Experimental study on the criticality of a methane/ethane mixture confined in nanoporous media. Langmuir, 35(36), 11635-11642.

Qiu, X., Tan, S. P., Dejam, M., & Adidharma, H. (2019). Simple and accurate isochoric differential scanning calorimetry measurements: phase transitions for pure fluids and mixtures in nanopores. Physical Chemistry Chemical Physics, 21(1), 224-231.

Qiu, X., Tan, S. P., Dejam, M., & Adidharma, H. (2020). Isochoric measurement of the evaporation point of pure fluids in bulk and nanoporous media using differential scanning calorimetry. Physical Chemistry Chemical Physics, 22(13), 7048-7057.

Qiu, X., Tan, S. P., Dejam, M., & Adidharma, H. (2021). Binary fluid mixtures confined in nanoporous media: Experimental evidence of no phase coexistence. Chemical Engineering Journal, 405, 127021.

Quateman, J. H., & Bretz, M. (1984). Nuclear-magnetic-resonance study of methane adsorbed on graphite. Physical Review B, 29(3), 1159.

Rao, D. N. (1997). A new technique of vanishing interfacial tension for miscibility determination. Fluid phase equilibria, 139(1-2), 311-324.

Ravikovitch, P. I., & Neimark, A. V. (2001). Characterization of micro-and mesoporosity in SBA-15 materials from adsorption data by the NLDFT method. The Journal of Physical Chemistry B, 105(29), 6817-6823.

Regnier, J., Thomy, A., & Duval, X. (1979). Comparative study of the first adsorbed layer of xenon and krypton on boron nitride and graphite. Journal of Colloid and Interface Science, 70(1), 105-111.

Richert, R. (2011). Dynamics of nanoconfined supercooled liquids. Annual review of physical chemistry, 62, 65-84.

Rossi, M. P., Ye, H., Gogotsi, Y., Babu, S., Ndungu, P., & Bradley, J. C. (2004). Environmental scanning electron microscopy study of water in carbon nanopipes. Nano Letters, 4(5), 989-993.

Rubin, B. (2010). Accurate simulation of non-Darcy flow in stimulated fractured shale reservoirs. In SPE Western regional meeting. Society of Petroleum Engineers.

Russo, P. A., Carrott, M. R., & Carrott, P. J. M. (2012). Trends in the condensation/evaporation and adsorption enthalpies of volatile organic compounds on mesoporous silica materials. Microporous and Mesoporous Materials, 151, 223-230.

Russell, B. A.; Migone, A. D. Low Temperature Adsorption Study of CO_2 in ZIF-8. Microporous Mesoporous Mater. 2017, 246, 178-185.

Salahshoor, S., Fahes, M., & Teodoriu, C. (2018). A review on the effect of confinement on phase behavior in tight formations. Journal of Natural Gas Science and Engineering, 51, 89-103.

Salahshoor, S., & Fahes, M. (2020). Experimental determination of the dew point pressure for bulk and confined gas mixtures using an isochoric apparatus. Fluid Phase Equilibria, 508, 112439.

Sanaei, A., Jamili, A., & Callard, J. (2014). Effect of pore size distribution and connectivity on phase behavior and gas condensate production from unconventional resources. In SPE Unconventional Resources Conference. Society of Petroleum Engineers.

Sandoval, D., Yan, W., Michelsen, M. L., & Stenby, E. H. (2015). Phase envelope calculations for reservoir fluids in the presence of capillary pressure. In SPE Annual Technical Conference and Exhibition. Society of Petroleum Engineers.

Sandoval, D. R., Yan, W., Michelsen, M. L., & Stenby, E. H. (2018). Influence of adsorption and capillary pressure on phase equilibria inside shale reservoirs. Energy & fuels, 32(3), 2819-2833.

Schmicker, D., Toennies, J. P., Vollmer, R., & Weiss, H. (1991). Monolayer structures of carbon monoxide adsorbed on sodium chloride: A helium atom diffraction study. The Journal of chemical physics, 95(12), 9412-9415.

Sedghi, M., & Piri, M. (2018). Capillary condensation and capillary pressure of methane in carbon nanopores: Molecular Dynamics simulations of nanoconfinement effects. Fluid Phase Equilibria, 459, 196-207.

Shabib-Asl, A., Plaksina, T., & Moradi, B. (2020). Evaluation of nanopore confinement during CO_2 huff and puff process in liquid-rich shale formations. Computational Geosciences, 1-16.

Shapiro, A. A., & Stenby, E. H. (1997). Kelvin equation for a non-ideal multicomponent mixture. Fluid phase equilibria, 134(1-2), 87-101.

Shapiro, A. A., & Stenby, E. H. (1998). Potential theory of multicomponent adsorption. Journal of Colloid and Interface Science, 201(2), 146-157.

Sheng, J. J., Mody, F., Griffith, P. J., & Barnes, W. N. (2016). Potential to increase condensate oil production by huff-n-puff gas injection in a shale condensate reservoir. Journal of Natural Gas Science and Engineering, 28, 46-51.

Shkolnikov, E. I., Sidorova, E. V., Malakhov, A. O., Volkov, V. V., Julbe, A., & Ayral, A. (2011). Estimation of pore size distribution in MCM-41-type silica using a simple desorption technique. Adsorption, 17(6), 911-918.

Sigal, R. F. (2015). Pore-size distributions for organic-shale-reservoir rocks from nuclear-magnetic-resonance spectra combined with adsorption measurements. SPE Journal, 20(04), 824-830.

Sing, K. S., & Williams, R. T. (2004). The use of molecular probes for the characterization of nanoporous adsorbents. Particle & Particle Systems Characterization: Measurement and Description of Particle Properties and Behavior in Powders and Other Disperse Systems, 21(2), 71-79.

Singh, J. K., & Kwak, S. K. (2007). Surface tension and vapor-liquid phase coexistence of confined square-well fluid. The Journal of Chemical Physics, 126(2), 024702.

Singh, S. K., Sinha, A., Deo, G., & Singh, J. K. (2009). Vapor− liquid phase coexistence, critical properties, and surface tension of confined alkanes. The Journal of Physical Chemistry C, 113(17), 7170-7180.

Singh, S. K., & Singh, J. K. (2011). Effect of pore morphology on vapor–liquid phase transition and crossover behavior of critical properties from 3D to 2D. Fluid Phase Equilibria, 300(1-2), 182-187.

Sirghi, L., Szoszkiewicz, R., & Riedo, E. (2006). Volume of a nanoscale water bridge. Langmuir, 22(3), 1093-1098.

Song, Y., Song, Z., Feng, D., Qin, J., Chen, Y., Shi, Y., ... & Song, K. (2020). Phase behavior of hydrocarbon mixture in shale nanopores considering the effect of adsorption and its induced critical shifts. Industrial & Engineering Chemistry Research, 59(17), 8374-8382.

Song, L.; Sun, Z.; Duan, L.; Gui, J.; McDougall, G. S. Adsorption and diffusion properties of hydrocarbons in zeolites. Microporous Mesoporous Mater. 2007, 104(1-3), 115-128.

Sonwane, C. G., & Bhatia, S. K. (1998). Adsorption in mesopores: A molecular-continuum model with application to MCM-41. Chemical engineering science, 53(17), 3143-3156.

Sonwane, C. G., Jones, C. W., & Ludovice, P. J. (2005). A model for the structure of MCM-41 incorporating surface roughness. The Journal of Physical Chemistry B, 109(49), 23395-23404.

Stalkup, F. I. (1983). Miscible displacement. New York: AIME

Standing, M. B., & Katz, D. L. (1942). Density of natural gases. Transactions of the AIME, 146(01), 140-149.

Stimpson, B. C. (2017). Impacts of confined space on production from tight reservoirs (Doctoral dissertation).

Takaiwa, D., Hatano, I., Koga, K., & Tanaka, H. (2008). Phase diagram of water in carbon nanotubes. Proceedings of the National Academy of Sciences, 105(1), 39-43.

Takei, T., Chikazawa, M., & Kanazawa, T. (1997). Validity of the Kelvin equation in estimation of small pore size by nitrogen adsorption. Colloid and Polymer Science, 275(12), 1156-1161.

Tan, S. P., & Piri, M. (2015). Equation-of-state modeling of confined-fluid phase equilibria in nanopores. Fluid Phase Equilibria, 393, 48-63.

Tan, S. P., & Piri, M. (2017). Heat of capillary condensation in nanopores: new insights from the equation of state. Physical Chemistry Chemical Physics, 19(7), 5540-5549.

Tan, S. P., Qiu, X., Dejam, M., & Adidharma, H. (2019). Critical point of fluid confined in nanopores: experimental detection and measurement. The Journal of Physical Chemistry C, 123(15), 9824-9830.

Teklu, T. W., Alharthy, N., Kazemi, H., Yin, X., Graves, R. M., & AlSumaiti, A. M. (2014). Phase behavior and minimum miscibility pressure in nanopores. SPE Reservoir Evaluation & Engineering, 17(03), 396-403.

Thommes, M., Köhn, R., & Fröba, M. (2002). Sorption and pore condensation behavior of pure fluids in mesoporous MCM-48 silica, MCM-41 silica, SBA-15 silica and controlled-pore glass at temperatures above and below the bulk triple point. Applied surface science, 196(1-4), 239-249.

Thommes, M. (2004). Physical adsorption characterization of ordered and amorphous mesoporous materials. In Nanoporous Materials: Science and Engineering (pp. 317-364).

Thomson, W. (1872). 4. On the equilibrium of vapor at a curved surface of liquid. Proceedings of the Royal Society of Edinburgh, 7, 63-68.

Todd, H. B., & Evans, J. G. (2016). Improved oil recovery IOR pilot projects in the Bakken formation. In SPE low perm symposium. Society of Petroleum Engineers.

Thompson, J. M., Okouma Mangha, V., & Anderson, D. M. (2011). Improved shale gas production forecasting using a simplified analytical method-a marcellus case study. In North American Unconventional Gas Conference and Exhibition. Society of Petroleum Engineers.

Thomy, A., & Duval, X. (1970). Adsorption de molécules simples sur graphite. Journal de Chimie Physique, 67, 1101-1110.

Thomy, A., Duval, X., & Regnier, J. (1981). Two-dimensional phase transitions as displayed by adsorption isotherms on graphite and lamellar solids. Surface Science Reports, 1(1), 1-38.

Todd, H. B., & Evans, J. G. (2016). Improved oil recovery IOR pilot projects in the Bakken formation. In SPE Low Perm Symposium. Society of Petroleum Engineers.

Travalloni, L., Castier, M., & Tavares, F. W. (2014). Phase equilibrium of fluids confined in porous media from an extended Peng–Robinson equation of state. Fluid Phase Equilibria, 362, 335-341.

Uchytil, P., Petrickovic, R., Thomas, S., & Seidel-Morgenstern, A. (2003). Influence of capillary condensation effects on mass transport through porous membranes. Separation and purification technology, 33(3), 273-281.

Vishnyakov, A., Piotrovskaya, E. M., Brodskaya, E. N., Votyakov, E. V., & Tovbin, Y. K. (2001). Critical properties of Lennard-Jones fluids in narrow slit-shaped pores. Langmuir, 17(14), 4451-4458.

Wang, H., Qu, Z., Yin, Y., Bai, J., & Yu, B. (2019). Review of molecular simulation method for gas adsorption/desorption and diffusion in shale matrix. Journal of Thermal Science, 28(1), 1-16.

Wang, J. (2010). Molecular dynamics studies of simple model fluids and water confined in carbon nanotube.

Wang, L., & Yu, W. (2019). Gas huff and puff process in Eagle Ford shale: Recovery mechanism study and optimization. In SPE Oklahoma City Oil and Gas Symposium. Society of Petroleum Engineers.

Wang, M., Wang, L., Zhou, W., & Yu, W. (2019). Lean gas huff and puff process for Eagle Ford Shale: Methane adsorption and gas trapping effects on EOR. Fuel, 248, 143-151.

Wang, S., Feng, Q., Javadpour, F., Xia, T., & Li, Z. (2015). Oil adsorption in shale nanopores and its effect on recoverable oil-in-place. International Journal of Coal Geology, 147, 9-24.

Whitson, C. H., & Brulé, M. R. (2000). Phase behavior (Vol. 20, p. 233). Richardson, TX: Henry L. Doherty Memorial Fund of AIME, Society of Petroleum Engineers.

Wongkoblap, A., Do, D. D., Birkett, G., & Nicholson, D. (2011). A critical assessment of capillary condensation and evaporation equations: A computer simulation study. Journal of colloid and interface science, 356(2), 672-680.

Wu, J. (2006). Density functional theory for chemical engineering: From capillarity to soft materials. AIChE journal, 52(3), 1169-1193.

Wu, K., Chen, Z., Li, X., & Dong, X. (2016). Methane storage in nanoporous material at supercritical temperature over a wide range of pressures. Scientific reports, 6, 33461.

Yang, G., Fan, Z., & Li, X. (2018). Determination of confined fluid phase behavior using modified Peng-Robinson equation of state. In Unconventional Resources Technology Conference. Society of Exploration Geophysicists, American Association of Petroleum Geologists, Society of Petroleum Engineers.

Yang, G., Fan, Z., & Li, X. (2019a). Determination of confined fluid phase behavior using extended Peng-Robinson equation of state. Chemical Engineering Journal, 378, 122032.

Yang, G., Chai, D., Fan, Z., & Li, X. (2019b). Analytical investigation of the confinement effect on capillary condensation pressure of fluids in nanopores. In SPE Western Regional Meeting. Society of Petroleum Engineers.

Yang, G., Chai, D., Fan, Z., & Li, X. (2019c). Capillary condensation of single- and multicomponent fluids in nanopores. Industrial & Engineering Chemistry Research, 58(41), 19302-19315.

Yang, G., & Li, X. (2020a). Modified Peng-Robinson equation of state for CO_2/hydrocarbon systems within nanopores. Journal of Natural Gas Science and Engineering, 84, 103700.

Yang, G., & Li, X. (2020b). Improved equation of state model for gas huff-n-puff EOR processes in unconventional reservoirs. In Unconventional Resources Technology Conference. Unconventional Resources Technology Conference (URTeC).

Yang, Q., Jin, B., Banerjee, D., & Nasrabadi, H. (2019). Direct visualization and molecular simulation of dewpoint pressure of a confined fluid in sub-10 nm slit pores. Fuel, 235, 1216-1223.

Yazicioglu, A. G., Megaridis, C. M., Nicholls, A., & Gogotsi, Y. (2005). Electron microscope visualization of multiphase fluids contained in closed carbon nanotubes. Journal of visualization, 8(2), 137-144.

Yellig, W. F., & Metcalfe, R. S. (1980). Determination and prediction of CO_2 minimum miscibility pressures (includes associated paper 8876). Journal of Petroleum Technology, 32(01), 160-168.

Yu, W., & Sepehrnoori, K. (2014). Simulation of gas desorption and geomechanics effects for unconventional gas reservoirs. Fuel, 116, 455-464.

Yu, W., Lashgari, H. R., Wu, K., & Sepehrnoori, K. (2015). CO_2 injection for enhanced oil recovery in Bakken tight oil reservoirs. Fuel, 159, 354-363.

Yu, W., Zhang, Y., Varavei, A., Sepehrnoori, K., Zhang, T., Wu, K., & Miao, J. (2019). Compositional simulation of CO_2 huff'n'puff in Eagle Ford tight oil reservoirs with CO_2 molecular diffusion, nanopore confinement, and complex natural fractures. SPE Reservoir Evaluation & Engineering, 22(02), 492-508.

Zarragoicoechea, G. J., & Kuz, V. A. (2004). Critical shift of a confined fluid in a nanopore. Fluid phase equilibria, 220(1), 7-9.

Zhang, J., Xu, F., Hong, Y., Xiong, Q., & Pan, J. (2015). A comprehensive review on the molecular dynamics simulation of the novel thermal properties of graphene. Rsc Advances, 5(109), 89415-89426.

Zhang, K., Jia, N., Zeng, F., & Luo, P. (2017). A new diminishing interface method for determining the minimum miscibility pressures of light oil–CO_2 systems in bulk phase and nanopores. Energy & Fuels, 31(11), 12021-12034.

Zhang, K., Nojabaei, B., Ahmadi, K., & Johns, R. T. (2020). Effect of gas/oil capillary pressure on minimum miscibility pressure for tight reservoirs. SPE Journal, 25(02), 820-831.

Zhang, P., Lu, S., & Li, J. (2019). Characterization of pore size distributions of shale oil reservoirs: A case study from Dongying sag, Bohai Bay basin, China. Marine and Petroleum Geology, 100, 297-308.

Zhang, S., & Ionkina, N. (2018). The Impact of capillary condensation on the hydrocarbon storage and mobility. In AAPG ACE.

Zhong, J. (2019). Nanofluidics: a window into transport and phase change in nanoporous systems (Doctoral dissertation).

Zhu, X. L., Wang, P. Y., Peng, C., Yang, J., Yan, X. B. Activated carbon produced from paulownia sawdust for high-performance CO_2 sorbents. Chin. Chem. Lett. 2014, 25(6), 929-932.

Zuo, J. Y., Guo, X., Liu, Y., Pan, S., Canas, J., & Mullins, O. C. (2018). Impact of capillary pressure and nanopore confinement on phase behaviors of shale gas and oil. Energy & fuels, 32(4), 4705-4714.

Appendix: Calculations with the Modified PR EOS

The modified PR EOS carries a highly similar expression as the original PR EOS, which makes the related calculations much more convenient. Only the attractive parameter *a* and covolume *b* need to be replaced by the confined values. The modified PR EOS in terms of the compressibility factor (Z) and the equations to calculate the fugacity are highly similar to the equations of the original PR EOS.

Compressibility Factor *Z*

The modified PR EOS in terms of the compressibility factor (*Z*) is:

$$Z^3+(B_c-1)Z^2-(3B_c^2+2B_c-A_c)Z+(B_c^3+B_c^2-A_cB_c)=0 \tag{1}$$

$$A_c = A\beta[1-1.7391\times(r_p/\sigma_{LJ})^{-1.379}] \tag{2a}$$

$$B_c = B\frac{1-1.7391\times(r_p/\sigma_{LJ})^{-1.379}}{1-1.1892\times(r_p/\sigma_{LJ})^{-0.807}} \tag{2b}$$

where A and B are the values of bulk fluids with the original PR EOS, r_p and σ_{LJ} are the pore size and molecule size, respectively, β is the confined covolume ratio which can be calculated with Equation (3.18b).

Fugacity Calculation

The equations to calculate the fugacity of vapor and liquid phase using the modified PR EOS are:

$$\ln\frac{f_{L/V}}{p}=\ln\phi_{L/V}=Z_{L/V}-1-\ln(Z_{L/V}-B_c)-\frac{A_c}{2\sqrt{2}B_c}\ln[\frac{Z_{L/V}+(1+\sqrt{2})B_c}{Z_{L/V}+(1-\sqrt{2})B_c}] \tag{3}$$

where f_L and f_V are the fugacity of liquid and vapor phase, respectively; Z_L and Z_V are the compressibility factor of liquid and vapor phase, respectively. A_c and B_c can be calculated by Equations 2(a) and 2(b) in the above section.

Saturation Pressure Determination

The method to determine the saturation pressure of a mixture, where the stability test algorithm is applied, is shown in Figure 1 (Yang et al., 2019a). The flow chart can be described as follows (Whitson and Brulé, 2000):

(1) The feed composition, temperature, pore size and the properties of each component of the mixture are firstly inputted.

(2) With the initial guess of a small value of the pressure, stability test of the mixture is performed to judge whether it will split into two phases or not.

(3) Calculate the mixture fugacity, f_{zi}; with multiple *Z*-factor roots, choose the root with the lowest normalized Gibbs energy.

(4) Use the Wilson equation to estimate the initial *K* values.

$$K_i^1 = \frac{\exp[5.37(1+\omega_i)(1-T_{ri}^{-1})]}{P_{ri}} \tag{4}$$

where ω_i, T_{ri}, and P_{ri} are the acentric factor, reduced temperature and reduced pressure of the *i*th component.

(5) The second-phase mole numbers, Y_i, is calculated by using the mixture composition z_i and the *K* value from the previous step, where "*V*" and "*L*" stand for vapor and liquid, respectively.

(6) The mole fraction y_i is obtained by normalizing the second-phase mole numbers.

(7) The component fugacities $(f_{yi})_V$ and $(f_{yi})_L$ from the modified EOS are subsequently calculated using Equation 3.

(8) The equal fugacity-ratio correction is subsequently determined, where S is the summation of mole numbers ($\sum Y_i$).

(9) The convergence is checked to make sure it is within the tolerance. If not, the K value needs to be updated and then repeated from step #4.

(10) If the convergence is within the tolerance, the value of S can be obtained and therefore whether the mixture is stable or unstable can be decided, namely, $S_v>1$ and $S_L>1$, or $S_v>1$ and $S_L<1$, or $S_V \leq 1$ and $S_L > 1$ represents unstable condition, and $S_V \leq 1$ and $S_L \leq 1$ indicates stable condition.

(11) If it is unstable, update the pressure until the saturation pressure is reached, which will result in a stable condition. The superscripts (n) and (n+1) represent the iteration level.

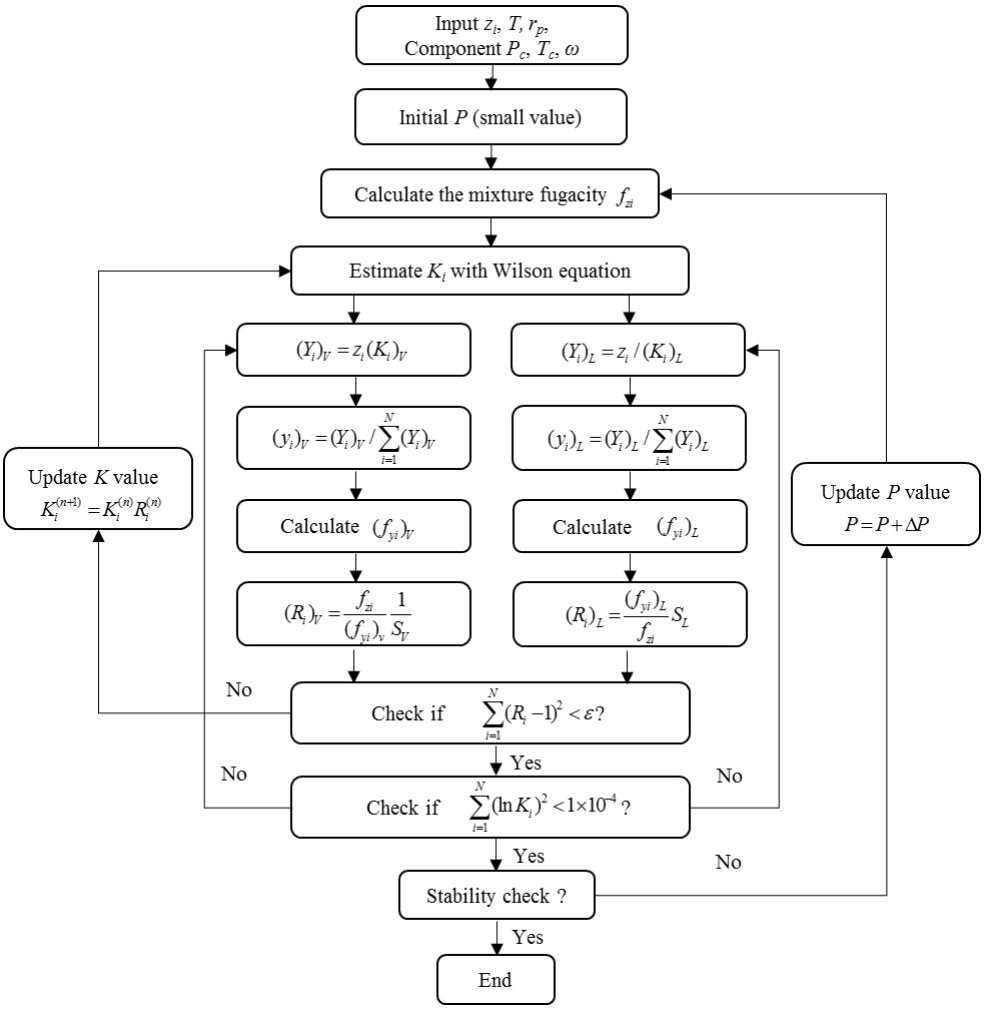

Figure 1 Flow chart to determine the saturation pressure of a mixture